FLOW CHARACTERIZATION AND MODELING OF CARTILAGE DEVELOPMENT IN A SPINNER-FLASK BIOREACTOR

A Dissertation
Presented to
The Academic Faculty

By

Philippe Sucosky

In Partial Fulfillment
Of the Requirements for the Degree of
Doctor of Philosophy in Mechanical Engineering

Georgia Institute of Technology
May 2005

FLOW CHARACTERIZATION AND MODELING OF CARTILAGE DEVELOPMENT IN A SPINNER-FLASK BIOREACTOR

Approved by:

Dr. G. Paul Neitzel, Chair
School of Mechanical Engineering
Georgia Institute of Technology

Dr. Marc K. Smith
School of Mechanical Engineering
Georgia Institute of Technology

Dr. Robert E. Guldberg
School of Mechanical Engineering
Georgia Institute of Technology

Dr. Pui-Kuen Yeung
School of Aerospace Engineering
Georgia Institute of Technology

Dr. Gordana Vunjak-Novakovic
School of Chemical Engineering
Massachusetts Institute of Technology

Date Approved: March 9, 2005

Work Spirit, Inspiration, Values, and Love
are what they offered and handed to me.

Pride of having me as a son and grandson
Is what I wish to give them today through these few pages.

To my beloved Parents and Grandparents.

***

Sens du Travail, Inspiration, Valeurs, et Amour
Sont ce qu’ils m’ont offert et transmis.

La fierté de m’avoir comme fils et petit-fils
Est ce que je souhaiterais leur donner aujourd’hui au travers de ces quelques pages.

A mes Parents et Grand-Parents bien-aimés.

ACKNOWLEDGMENTS

I would like to take advantage of this page to express my deepest thanks to the persons who have made this work possible. I would especially like to thank:

Dr. G. Paul Neitzel, for advising this research, sharing his knowledge, and opening the doors of the Scientific Community to me;

Drs. Robert E. Guldberg, Marc K. Smith, Gordana Vunjak-Novakovic and Pui-Kuen Yeung, for serving on my reading committee;

Drs. Lisa Freed and Bojana Obradovic for their respective works on tissue culture and histological analysis;

The Georgia Tech/Emory Center for the Engineering of Living Tissues (GTEC), for funding this research;

The National Science Foundation, for supporting the tissue-engineering community;

Peter Nagy, Maria Carnasciali and Damien Moreau, my fellow labmates, for their support, advice, and good humor;

Sander Ubbink, Jason Brown and Bahar Bilgen, the graduate students who crossed my path and shared their expertise with me;

Dr. Robert Nerem, Donna Brown, Donna Gamble and Sally Gerrish, for their efforts to serve GTEC;

Judith Diamond, for her administrative skills and her assistance;

And all the other persons who I could not cite on this page but whose contribution to this research will not be forgotten.

TABLE OF CONTENTS

APPENDICES

LIST OF TABLES

LIST OF FIGURES

LIST OF SYMBOLS or ABBREVIATIONS

Symbol	Description	Units
α	permeability of a homogeneous porous medium	m^2
$\left[\alpha_{ij}\right]$	permeability tensor	m^2
δ_{ij}	Kronecker delta operator	dimensionless
Δh	thickness of the porous medium	m
Δl	side length of the PIV interrogation window	pixels
Δx	PIV grid spacing	pixels
ε	energy dissipation rate per unit mass	$m^2.s^{-3}$
θ_e	angle of an equiangular cell	°
θ_e	angle of an equiangular cell	°
$\theta_{\min}$	smallest cell angle	°
$\theta_{\max}$	largest cell angle	°
η	Kolmogorov scale	m
μ	fluid dynamic viscosity	$kg.m^{-1}.s^{-1}$
μ_t	turbulent dynamic viscosity	$kg.m^{-1}.s^{-1}$
ν	fluid kinematic viscosity	$m^2.s^{-1}$
ν_t	turbulent kinematic viscosity	$m^2.s^{-1}$
ρ	fluid density	$g.cm^{-3}$
ρ_f	mass density of the fluid	$g.cm^{-3}$
ρ_{ij}	turbulence correlation coefficient relative to the velocity fluctuations u_i and u_j	dimensionless
ρ_p	mass density of the particle	$g.cm^{-3}$
ω	impeller angular velocity	$rad.s^{-1}$
σ_ε	turbulent Prandtl number for ε	dimensionless
σ_k	turbulent Prandtl number for k	dimensionless
$\overline{\tau}$	mean-shear stress magnitude	$N.m^{-2}$
$\overline{\tau}_{global}$	average wall-shear stress magnitude on the lateral construct surface	$N.m^{-2}$
$\overline{\tau}_{local}$	average wall-shear stress magnitude at a point on the construct perimeter contained in the histological cross section	$N.m^{-2}$
τ_{ij}	*ij*-component of the Reynolds stress tensor	$N.m^{-2}$
$\tilde{\tau}_{ij}$	*ij*-component of the instantaneous shear stress tensor	$N.m^{-2}$

Symbol	Description	Units
$\overline{\tau}_{ij}$	*ij*-component of the mean-shear stress tensor	N.m^{-2}
ψ	basis function of the thin-plate spline f	dimensionless
$\left[\psi_{bg}\right]$	collocation matrix of size $b \times g$	dimensionless
Φ_1	holder diameter above the scaffold	m
Φ_2	holder diameter below the scaffold	m
Φ_3	pipe diameter	m
χ	maximum equiangle skew	dimensionless
ω	angular velocity of the stir bar	s^{-1}
ω_i	x_i -component of the vorticity-fluctuation vector	s^{-1}
a	set of coefficients for the thin-plate spline f	dimensionless
a_p	radius of a particle	m
A_0	constant used in the realizable $k-\varepsilon$ model	dimensionless
A_S	constant used in the realizable $k-\varepsilon$ model	dimensionless
$\mathbf{c}$	set of prescribed site coordinates for the thin-plate spline f	dimensionless
C	continuity value	s^{-1}
$\lVert C \rVert$	normalized continuity value	dimensionless
C_1	constant depending on k used in the realizable $k-\varepsilon$ model	dimensionless
$C_{1\varepsilon}$	constant used in the realizable $k-\varepsilon$ model	dimensionless
C_2	constant depending on ε used in the realizable $k-\varepsilon$ model	dimensionless
$C_{2\varepsilon}$	constant used in the realizable $k-\varepsilon$ model	dimensionless
C_μ	constant used in the realizable $k-\varepsilon$ model	dimensionless
d	construct diameter	m
E	energy function	dimensionless
f	thin-plate spline function	dimensionless
$f_{\tilde{U}_i}$	thin-plate spline function for $\tilde{U}_i$	m.s^{-1}
g_r	gravity constant	m.s^{-2}
H_1	vertical distance between the free surface and the top surface of the construct	m
H_2	vertical distance between the pipe exit and the lower surface of the construct	m
k	turbulent kinetic energy per unit mass	m^2.kg^{-1}.s^{-2}
L	impeller length	m
L_3	pipe length	m
$_m$	quantity relative to the model bioreactor	dimensionless
n	current PIV realization	dimensionless
n_c	number of unknown coefficients used in spline construction	dimensionless

Symbol	Description	Units
n_r	number of PIV realizations	dimensionless
overlap	percentage overlap between two adjacent PIV interrogation windows	dimensionless
$_p$	quantity relative to the prototype bioreactor	dimensionless
px_i	number of non-white pixels in the 5×5-pixel window i	pixels
P	pressure	N.m^{-2}
P_G	GAG fraction	% wet weight of tissue
$P_{G\,loc}$	total GAG fraction in a slice	% wet weight of tissue
$P_{G\,tot}$	local GAG fraction measured in the tissue falling in an angular sector outside the porous scaffold	% wet weight of tissue
Q	volumetric flow rate of fluid across a porous medium	m^3.s^{-1}
$\bar{R}$	local red intensity	dimensionless
$\bar{R}_i$	local red intensity measured in the 5×5-pixel window i	dimensionless
R^2	correlation coefficient	dimensionless
Re	Reynolds number	dimensionless
S	function of the mean strain rate used in the realizable $k-\varepsilon$ model	s^{-1}
U^*	function of the mean strain and rotation rate used in the realizable $k-\varepsilon$ model	s^{-1}
u_i	x_i-component of the fluctuating velocity	m.s^{-1}
U_i	x_i-component of the average fluid velocity across a porous medium	m.s^{-1}
$\tilde{U}_i$	x_i-component of the instantaneous velocity	m.s^{-1}
$\bar{U}_i$	x_i-component of the mean velocity	m.s^{-1}
$[\tilde{U}_{i\,rs}]$	matrix of size $r\times s$ containing the x_i-components of the instantaneous velocity obtained by adapted cross-correlation	m.s^{-1}
$\mathbf{u_{ij}}$	fluctuating-velocity vector in the plane $\left(\mathbf{e_i},\mathbf{e_j}\right)$	m.s^{-1}
$\mathbf{U}$	average fluid velocity vector across a porous medium	m.s^{-1}
$\mathbf{\tilde{U}_{ij}}$	instantaneous-velocity vector in the plane $\left(\mathbf{e_i},\mathbf{e_j}\right)$	m.s^{-1}
$\mathbf{\bar{U}_{ij}}$	mean-velocity vector in the plane $\left(\mathbf{e_i},\mathbf{e_j}\right)$	m.s^{-1}
U_{St}	particle sedimentation velocity	m.s^{-1}
V	volume of fluid in the vessel	m^3
w_x	uncertainty on the quantity x	dimensionless
$[x_{i\,rs}]$	matrix of size $r\times s$ containing the x_i-coordinates of the PIV grid	m

Symbol	Description	Units
$[x'_{i\,rs}]$	matrix of size $r \times s$ containing the x_i -coordinates of the PIV grid points after adapted cross-correlation	m
Z	set of prescribed values for the thin-plate spline function f	dimensionless
$Z_{\tilde{U}_i}$	set of prescribed values for the thin-plate spline function $f_{\tilde{U}_i}$	m.s^{-1}
$\lvert\ \rvert$	absolute value	dimensionless
$\lVert\ \rVert$	norm of a vector	dimensionless
∇	gradient operator	m^{-1}
$\frac{\partial}{\partial}$	partial derivative	dimensionless
$\overline{}$	mean value obtained by ensemble-averaging	dimensionless
$(\mathbf{e_1}, \mathbf{e_2}, \mathbf{e_3})$	Cartesian coordinate system	dimensionless
(x_1, x_2, x_3)	point coordinates in the Cartesian system $(\mathbf{e_1}, \mathbf{e_2}, \mathbf{e_3})$	m

SUMMARY

Bioreactors are devices used for the growth of tissues in a laboratory environment. They exist in many different forms, each designed to enable the production of high-quality tissues. The dynamic environment within bioreactors is known to significantly affect the growth and development of the tissue. Chondrocytes, the building blocks of articular cartilage, for example, are stimulated by mechanical stresses such as shear, as compared with those in tissues grown under static incubation conditions. On the other hand, high shear can damage cells. Consequently the shear-stress level has to be controlled in order to optimize the design and the operating conditions of bioreactors.

Spinner flasks have been used for the production of articular cartilage *in vitro*. Assuming the existence of a relation between the cellular glycosaminoglycan (GAG) synthesis and the local shear stresses on the construct surfaces, this research focuses on the development of a model for cartilage growth in such devices. The flow produced in a model spinner flask is characterized experimentally using particle-image velocimetry (PIV). A computational fluid dynamic (CFD) model validated with respect to the laboratory measurements is constructed in order to predict the local shear stresses on the construct surfaces. Tissue growth experiments conducted in the prototype bioreactor permit construct histologies and GAG contents to be analyzed and then correlated with the shear-stress predictions. The integration of this relation into the CFD model enables the prediction of GAG synthesis through convective effects. Coupling this convective model to an existing diffusive model produces a complete cartilage-growth model for use in aiding the optimization of existing bioreactors, and in the design of new ones.

CHAPTER 1

INTRODUCTION

Cartilage structure

Cartilage is a connective tissue that composes most of the skeleton of vertebrate embryos and, except for a small number of structures, is replaced by bone during ossification in the higher vertebrates. The three major types of cartilage that can be found in the human body are hyaline cartilage, elastic cartilage and fibrocartilage. The most prevalent, hyaline cartilage, is present at the articular surface of joints. Its functions are to reduce the friction in the joint and to distribute the forces of weight bearing.

Articular cartilage is mainly composed of cells of a single type (chondrocytes) and an extracellular matrix (ECM) (**Figure 1.1a**). The chondrocytes are important in the control of matrix growth and resorption through the local production of cytokines and proteases. Those cells occupy only 2% of the total volume of articular cartilage and their metabolism is mainly affected by biochemical and mechanical signals (Muir, 1995). The ECM is composed of three basic components, water (75% by weight), a non-fibrillar matrix (20%), and a fibrillar matrix (5%) (Aigner and McKenna, 2002). The non-fibrillar matrix comprises aggrecan monomers attached to hyaluronic acid, link proteins, and negatively-charged glycosaminoglycans (GAG), forming proteoglycans. Those aggrecan aggregates secreted into the matrix serve to trap and hold water to regulate the hydration of the matrix. The interaction of water with the glycosaminoglycans, the most hydrophilic components of cartilage, determines the viscoelastic properties of the tissue (Maroudas, 1976; Maroudas and Venn, 1977). Type-IX, type-XI, and more predominantly type-II collagen fibers are the main components of the cross-linked fibrillar matrix. This particular

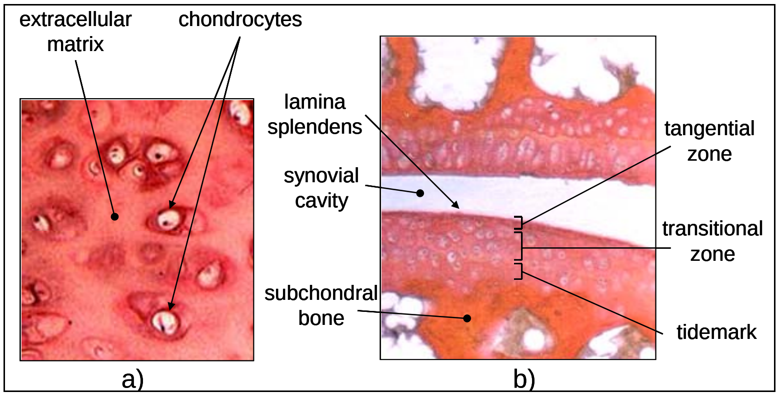

Figure 1.1: Hyaline cartilage structure (hematoxylin and eosin stain). a) Typical field of hyaline cartilage. The cells grouped into small clusters are the chondrocytes. The extracellular matrix (ECM) surrounding the cells is made of collagen type II, proteoglycans and water (School of Physical Therapy, Slippery Rock University). b) The organization of these components into three layers (tangential zone, transitional zone and radial zone) characterizes the mechanical properties of the cartilage tissue (College of Medicine, University of Florida).

fibrillar arrangement permits the anchoring of the cartilage to the bone, the control of the loss of synovial fluid through the cartilage, and prevents the loss of proteoglycans.

Numerous studies have shown that the organization of these structural components in different layers (**Figure 1.1b**) also affects the mechanical behavior of the tissue (Muir et al., 1970; Ogston, 1970). In the superficial tangential zone, the type-II collagen fibers are parallel to the joint surface and are compacted to form a protective layer. This organization provides the cartilage tissue with the ability to resist shear forces. The transitional zone composed almost entirely of proteoglycans is capable of deforming and absorbing weight forces. In the radial zone, the collagen fibers are attached to a layer of calcified cartilage called the tidemark. This particular configuration allows the distribution of the load and the large concentration of proteoglycans in this region helps cartilage to resist compression.

Cartilage disorders

As a load-bearing tissue, articular cartilage can be damaged gradually because of wear and tear. The progressive loss and deterioration of cartilaginous tissues commonly called osteoarthritis is often accompanied by pain, stiffness and limitation of movement. This degenerative joint disorder can be either age-related (primary osteoarthritis) or the result of a trauma or a disease (secondary osteoarthritis) (Risbud and Sittinger, 2002). Since articular cartilage is avascular, aneural and alymphatic, those damages are often irreversible and surgery may be necessary to recover joint function. Cartilage defects resulted in more than one million surgical procedures in the United States in 1991 (Langer and Vacanti, 1993) and are expected to affect about 60 millions of Americans by the year 2020 (Praemer et al., 1999). More specifically, osteoarthritis was estimated to affect more than 20 million Americans in 1998 (Lawrence et al., 1998). This widespread disorder resulting from the dysregulation of matrix turnover by the chondrocytes is mediated by both biochemical and mechanical pathways.

The inability of the tissue to respond to mechanical loading is a progressive process. First, osteoarthritis causes the cartilage to break down, making it thinner and then creating cracks in its surface (**Figure 1.2a**). Gaps in the cartilage can expand until they reach the bone itself (**Figure 1.2b**). The synovial fluid leaks into cracks which form in the bone surface. This causes further damage and in some cases can lead to cysts in the bone or other deformities (**Figure 1.2c**). Eventually, if not treated, damage can progress to the point where the bones in the joint become seriously and permanently deformed (**Figure 1.2d**).

Cartilage treatment strategies

Because cartilage does not heal itself, the objectives of the current therapies are focused on the reduction of the symptoms and the restoration of joint functions. Surgical and non-surgical techniques have been developed in order to offer patients less-invasive options than a full prosthetic joint replacement.

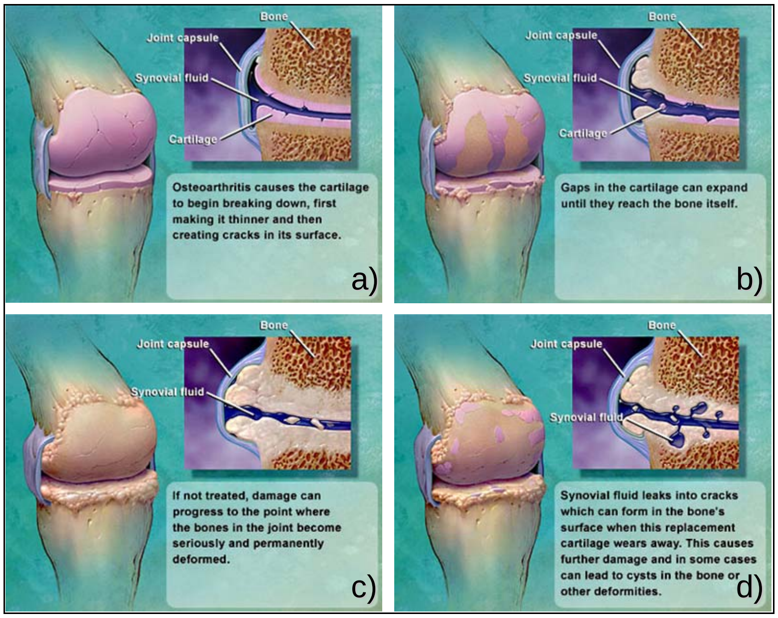

Osteoarthritis causes the cartilage to begin breaking down, first making it thinner and then creating cracks in its surface.

Gaps in the cartilage can expand until they reach the bone itself.

If not treated, damage can progress to the point where the bones in the joint become seriously and permanently deformed.

Synovial fluid leaks into cracks which can form in the bone's surface when this replacement cartilage wears away. This causes further damage and in some cases can lead to cysts in the bone or other deformities.

Figure 1.2: The different steps of osteoarthritis: a) breaking down of cartilage and formation of cracks in its surface; b) expansion of the gaps to the bone; c) penetration of synovial fluid into the cracks and formation of cysts; and d) permanent deformation of the bone in the joint (source: Medco Health Solutions, Inc).

Pharmacologic and viscosupplementation therapies are non-surgical treatments that are well-adapated for patients suffering mild cartilage lesions (Jackson et al., 2001). The pharmacologic procedure consists of the delivery of nonsteroidal anti-inflammatory drugs whereas viscosupplementation corresponds to the injection of hyaluronic acid. Although these procedures are thought to help relieve the signs related to osteoarthritis, their efficiency to limit joint degeneration has not been isolated.

More severe osteochondral lesions need to be treated with more invasive surgical procedures. Arthroscopic lavage and debridement that consist of the removal of cartilage debris and the contouring of the articular surfaces have only a limited potential for healing. A more efficient technique consists of stimulating cartilage repair by promoting the migration of repair cells into the osteochondral defects; the recruitment of potential repair cells is performed by drilling, abrasion or microfracture techniques (Jackson et al., 2001). Although this treatment option leads to the filling of the cartilage lesions, the newly formed tissue presents inferior mechanical properties than native cartilage.

Autologous transplantation techniques use the patient's own healthy tissue, carving it into a three-dimensional implant that is then substituted for the cartilage defect. In the so-called mosaicplasty procedure, the chondral lesion is excised and abrasion arthroplasty is performed in order to refresh the bone base of the defect (**Figure 1.3a**). Multiple individual osteochondral cores are harvested from a peripheral non-weight-bearing area of the knee (**Figure 1.3b, Figure 1.3c**). The grafts are press fit into the lesion in a mosaic-like fashion within drilled tunnels (**Figure 1.3d, Figure 1.3e**). Although, this technique is suitable to treat large lesions, it is associated with a high donor-site morbidity.

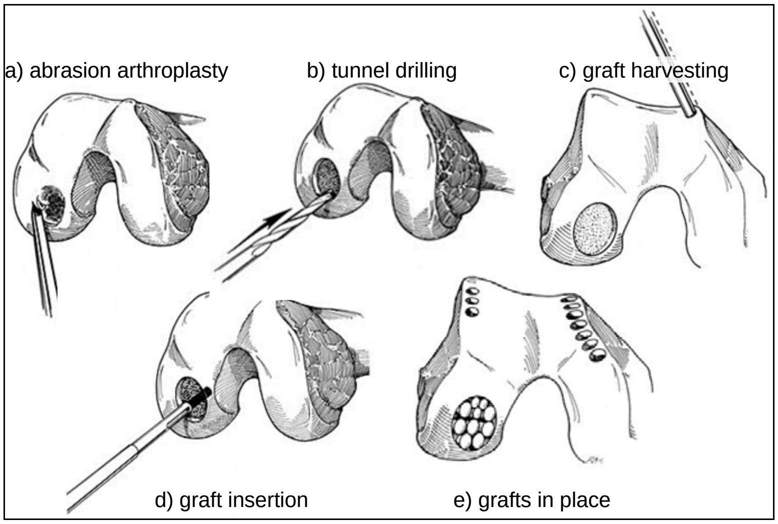

Figure 1.3: Schematic of the mosaicplasty technique: a) abrasion arthroplasty is performed to prepare the lesion; b) tunnels are drilled in the defect area; c) osteochondral cores are harvested from a peripheral area; d) the grafts are inserted into the tunnels; and e) the grafts are press fit into the lesion in mosaic-like fashion (source: http://www.maitrise.orthop.com).

CARTICEL, a viable FDA-licensed treatment option that employs a commercial process to culture the patient's own cartilage cells has been recently developed (Hauselmann et al., 1998).

In this technique, a biopsy of healthy cartilage from the patient is used as a cell source that is then expanded in culture (**Figure 1.4a**). Once a sufficient number of cells have been grown, the defect is prepared surgically for the introduction of the cultured cells (**Figure 1.4b**). A small piece of periosteum (i.e., bone-lining tissue) is harvested and sutured over the defect. The cultured cells are then injected under the periosteum where they can fill the defect with a durable cartilage (**Figure 1.4c**).

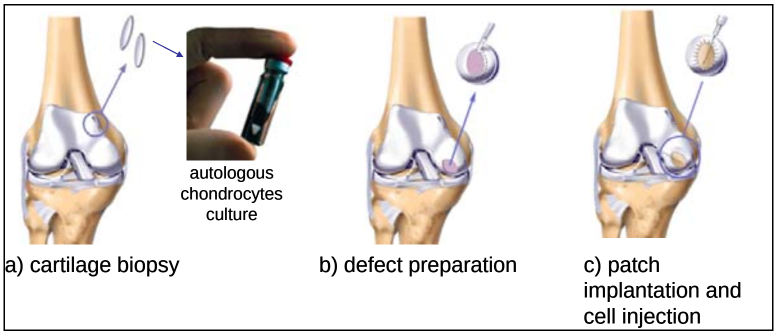

Figure 1.4: Schematic of the CARTICEL technique: a) a biopsy of cartilage is harvested and the cells are expanded in culture; b) the defect area is prepared prior to implantation; and c) a small piece of periosteum is sutured over the defect and cells are injected under the patch (source: http://www.maitrise.orthop.com).

This technique was shown to produce a hyaline-cartilage-like tissue, yet the lack of long-term, follow-up data from patients who have had the procedure does not permit one to draw any significant conclusion at this time. Finally, when the cartilage disorders are such that the above treatments are unlikely to be successful, a last option consists of replacing the damaged tissue with artificial polymeric implants or performing a total knee replacement.

Although the above-described therapies have been used extensively for years to repair cartilage degeneration, they raise some critical issues. Because the transplantation technique uses autologous cells, the tissue substitute is immune acceptable. However, this technique does not lend itself to off-the-shelf availability. The size and the shape of a required three-dimensional implant may also be difficult to obtain. Two-thirds of the patients who undergo a total knee replacement are over 65 years of age. In fact, many orthopedists are hesitant to recommend the procedure for young individuals because of the short viability of the prosthesis (10 to 15 years) (Cuckler, 1997). In addition, although the implantation of artificial prostheses relaxes the tissue availability limitation, it induces a problem of immuno-compatibility with the host. Finally, because they are fabricated from artificial materials, these implants poorly simulate the physiological and mechanical functions of native tissues.

Tissue engineering: challenges and issues

The difficulties associated with traditional therapies motivated recent pursuit of new treatments centered around tissue-engineered cartilage. At a National Science Foundation Workshop held in 1988, the term “tissue engineering” was officially defined as, “the application of principles and methods of engineering and life sciences toward fundamental understanding of structure-function relationships in normal and pathological mammalian tissue and the development of biological substitutes to restore, maintain or improve tissue function.” (Nerem and Sambanis, 1995). Ideally, this concept of treatment could be applied to cartilage restoration for patients suffering from cartilage damage. The challenge consists of engineering a functional tissue substitute with chondrocytes in culture that can be later implanted *in vivo* and integrated with its surrounding environment.

The basic concepts can be easily adapted to cartilage replacement, yet it remains much more difficult to achieve a satisfactory result. Schematically, isolated cells obtained from autologous cells, stem cells or continuous cell lines are seeded onto a biodegradable scaffold meeting the biological requirements of the tissue and providing the resulting tissue with structural and mechanical integrity. The culture system (i.e., cells and scaffold) is then placed in a well-characterized sterile environment (a bioreactor) providing the necessary nutrients. Under ideal conditions, tissue engineering would produce and maintain sterile cartilage tissue with defined shape and size that can be inserted in a patient’s body through traditional surgery (**Figure 1.5**).

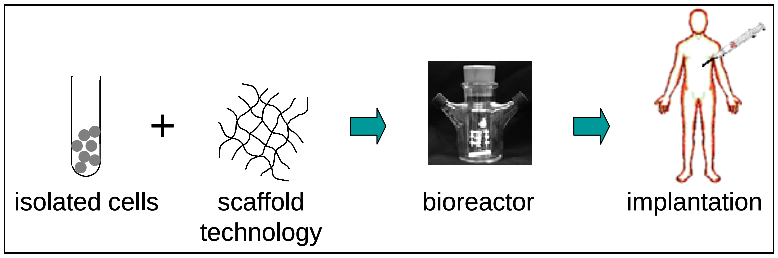

Figure 1.5: Schematic of the tissue-engineering technique. The main steps are the isolation of the cells, the development of a three-dimensional scaffold, the culture *in vitro* and the implantation in the host.

This promising strategy still faces major barriers. The development of three-dimensional constructs that enable a successful integration of the synthesized tissue with the host is one of them. Research in the field of biomaterials permitted the design of biodegradable and biocompatible scaffolds with a structure promoting cell attachment and tissue proliferation. Natural polymers such as hyaluronic acid and collagen have already been used with success but synthetic polymers such as polylactic acid (PLLA), polyglycolic acid (PGA), and copolymer (PLGA) yield better results (Agrawal and Ray, 2001; Grande et al., 1997). Despite such progress, current scaffold technologies require the use of invasive surgical interventions for transplantation (Risbud and Sittinger, 2002). In addition, off-the shelf availability of the tissue substitute implies high cell production. Therefore, bioreactor technology needs to be improved and optimized in order to meet this requirement. Another obstacle consists of the preservation of the newly synthesized tissue substitutes prior to implantation. In fact, although cryopreservation emerges as the method of choice to protect and maintain engineered tissues, its mechanisms and effects on the cells are still not fully understood. Finally, because tissue engineering is a recent strategy under development, only a few tissue-engineered cartilage products are readily available on the market. Despite the increasing number of companies focusing their activity on tissue engineering, only a few have already received the approval of the Food and Drug Administration (FDA) for the commercialization of their products. Since the long-term behavior of engineered tissues implanted in human bodies is not yet known, the validation of a tissue-engineered product is a long and costly procedure.

Although the tissue-engineering strategy is far from routine, it presents obvious advantages when compared with traditional treatments. First, the tissue product is made entirely of biological materials. Additionally, the manipulation of the artificial environment enables the growth of three-dimensional, fully functional cartilage substitutes that are immuno-compatible with the host. Finally, the scale-up made possible through the culture of such bioartificial substitutes solves the problem of the critical donor shortage presently limiting the application of the transplantation technique. Those benefits justify the current efforts to better control this treatment strategy and to address its challenges.

***In vitro* culture environment**

The success of the tissue-engineering technique depends mostly on the production of constructs capable of mimicking the compositional and mechanical properties of the native cartilage, and the achievement of the functional integration between the tissue-engineered constructs and the surrounding articular cartilage following implantation. Bioreactors are cell-culture systems designed to enable the growth of fully functional engineered tissues. The artificial environment they simulate can be controlled precisely to maximize the process efficiency.

As mammalian cells, cartilaginous cells are very different from other living cells. The only similarities they share with other cells are their basic needs: the delivery of nutrients and the removal of metabolites. Therefore, the culture conditions should enable adequate mass transfer of nutrients and oxygen along with removal of wastes. Compared with primitive microorganisms, mammalian cells are larger and more complex. Due to their large size, their lack of a protective wall and the presence of integrins inserted in their plasma membrane, mammalian cells are very sensitive to their dynamical environment and responsive to extracellular signals. The artificial environment of bioreactors used for the growth of cartilage tissue must accommodate these requirements. It must provide an appropriate surface of attachment promoting cell seeding and spreading, a serum containing the necessary nutrients and finally, an appropriate mixing strategy to enhance mass transfer.

The spinner-flask bioreactor is one such device that has been designed to better control the culture of cartilage tissue *in vitro* (**Figure 1.6**). The bioreactor vessel is a simple cylindrical glass container. A stirring element located at the bottom of the container ensures the mixing of the liquid culture medium. Polymer scaffolds such as biodegradable PGA are threaded onto

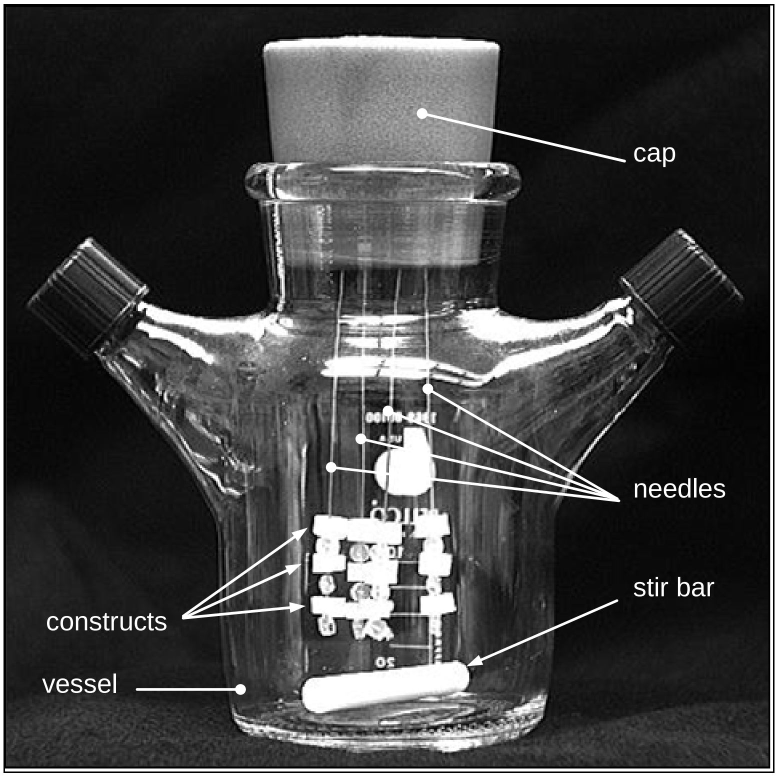

Figure 1.6: Spinner-flask bioreactor. The rotating stir bar at the bottom generates the mass transfer of the nutrients. The constructs are threaded onto four needles fixed in the cap of the vessel.

needles, separated by spacers. These provide attachment sites for chondrocytes and promote cell migration and differentiation. Once attached, the chondrocytes express ECM, ultimately producing a (hopefully) homogeneous solid piece of tissue. Each needle usually holds three scaffolds separated by small silicone-tubing cylinders (spacers). Two to four needles can be inserted into the cap of the bioreactor, holding the tissue constructs in fixed positions within the reactor vessel. Despite its simple geometry, this *in vitro* culture system generates a complex flow environment. Consistent with the work of Vunjak-Novakovic et al. (1996), if the length L of the stir bar is chosen as the characteristic length and twice the impeller tip speed as the velocity scale, the Reynolds number of the bulk flow is defined as

$$Re = \frac{\omega L^2}{\nu}, \tag{1-1}$$

where ω is the angular velocity of the impeller and ν is the kinematic viscosity of the liquid. The spinner flask modeled for this work contains four construct arrays and a stir bar that is 4.53 cm long and is typically operated at 50.0 rpm (i.e., 0.833 rev/s). A typical value of the kinematic viscosity of the culture medium is 0.971 cSt (Croughan et al., 1987) yielding a Reynolds number equal to 1760. Since this value is much larger than the critical impeller Reynolds number of 1000 for transition to turbulence determined by Nagata, 1975), the flow environment within such bioreactors is not only unsteady but also turbulent.

This particular bioreactor is well adapted for the growth of tissues *in vitro*. First, the spinner flask is capable of continuously perfusing fresh medium through the culture and removing depleted medium. In addition, this bioreactor generates the agitation required to distribute homogeneously critical components such as nutrients and dissolved oxygen throughout the culture medium. Finally, the presence of multiple constructs in the medium provides a surface-to-volume ratio large enough for the effective scale-up of the culture (Feder and Tolbert, 1983). The principal concern raised by this vessel is related to the possible damage that agitation might cause to the anchoring cells.

Cartilage response to mechanical environment

The proper control of biological parameters is crucial for the growth of a functional tissue *in vitro*. Several studies have shown that mechanical parameters significantly affect the structure and the proliferation rate of the growing tissues. The mixing rate, mass-transfer rate, stress level and flow regime, all of which affect the biochemical composition and the morphology of the resulting tissue, are determined by the hydrodynamics of the bioreactor. For cartilage, external mechanical forces have been shown to regulate the expression of extracellular matrix *in vivo* (Mow et al., 1991). The structure of this matrix determines the biochemical properties of the tissue. *In vitro*, external stresses can directly affect the shape of the cells and can even modify their function by inducing some changes in the mass-transfer rate of nutrients. Vunjak-Novakovic et al. (1996) have analyzed and quantified the effects of hydrodynamic forces on cells under turbulent flow conditions. Bovine chondrocytes were seeded under dynamic conditions and grown for eight weeks in a spinner flask under either mixed (50 rpm) or static incubation conditions. As shown in **Figure 1.7** and reported in their paper, constructs cultivated in mixed conditions were thicker, more homogeneous, stiffer, and contained more cells than constructs cultivated under static conditions. In an earlier study, Freed and Vunjak-Novakovic (1995) studied the growth of articular cartilage within both the near-free-fall environment of the NASA rotating-wall vessel (RWV) bioreactor and a spinner-flask bioreactor. Bovine articular chondrocytes were seeded onto fibrous PGA scaffolds. In terms of cellular development, the scaffolds populating the RWV were covered by one to two cell layers. In contrast, multiple cell layers could be observed on the cell-polymer constructs grown in the spinner flask. The different hydrodynamic environments existing in the two devices influenced the properties of the resulting

Figure 1.7: Cross-sections of cartilage tissues grown by Vunjak-Novakovic et al. (1996) after eight weeks. The construct grown under turbulent conditions (left) is thicker and contains more GAG than constructs grown in orbitally mixed Petri dish (middle) and under static incubation conditions (right). GAG is stained red with safranin-O.

tissues; cartilage grown in the RWV was characterized by fewer cells and more GAG than that grown the spinner flask.

In the work done by Freed et al. (1997), bovine chondrocyte cells were seeded on PGA scaffolds in RWVs fitted with a so-called "viscous pump" (Begley and Kleis, 2000; described below) and operated on both the Mir Space Station and on Earth. Eventually, both cultures presented viable and differentiated cells exhibiting the synthesis of proteoglycans and type-II collagen. Constructs grown in Space were more spherical in shape (**Figure 1.8**) and mechanically inferior than those grown on Earth in terms of aggregate modulus, hydrodynamic permeability, and dynamic stiffness. The principal difference between the two culture environments was the flow generated within the bioreactors. On Earth, the effect of gravity forced the constructs to settle near the bottom of the horizontally (i.e., the sysmmetry axis) oriented vessel and collide with its wall while in Space, the constructs floated freely in the medium, following the flow driven by the viscous pump.

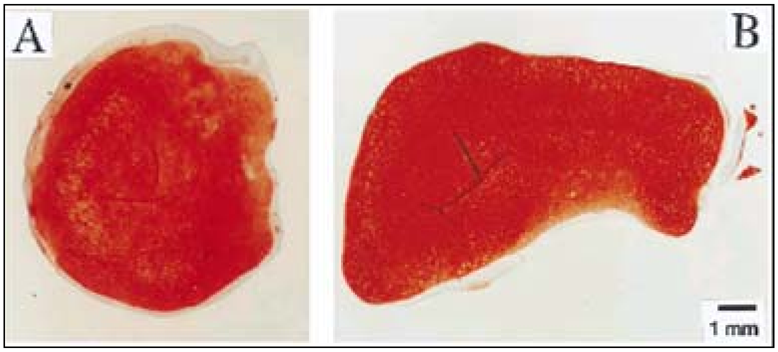

Figure 1.8: Cross-sections of constructs obtained by Freed et al. (1997) from: A) tissues grown in space; and B) on Earth. In the absence of gravity, the engineered tissue was more homogeneous in shape than the tissue exposed to terrestrial gravity. GAG is stained red with safranin-O.

Gooch et al. (2001) have also addressed the effects of the hydrodynamic environment on tissue-engineered cartilage under both static and mixed conditions. Although increasing mixing rates stimulated the synthesis of GAG and collagen by the cells, they decreased the fraction of GAG retained by the constructs. Finally, more than the mixing intensity, the presence or absence of mixing was identified as the primary key parameter affecting the GAG and collagen content in the constructs.

Finally, Saini and Wick (2003) have subjected cartilage constructs to a controlled shear-stress environment through the use of a concentric-cylinder bioreactor. They found that cell counts, collagen, and GAG content per construct were all affected by the level of applied stress. In addition, the composition of the constructs was shown to be highly dependent on the duration of the exposure to the mechanical environment (**Figure 1.9**). The above observations support the hypothesis that dynamic flow conditions significantly affect the quality of cartilage grown within bioreactors.

Flow studies in bioreactors

Although the ideal conditions for optimal cell cultivation have not yet been completely identified, a conclusion can be drawn from the preceding that the hydrodynamic environment

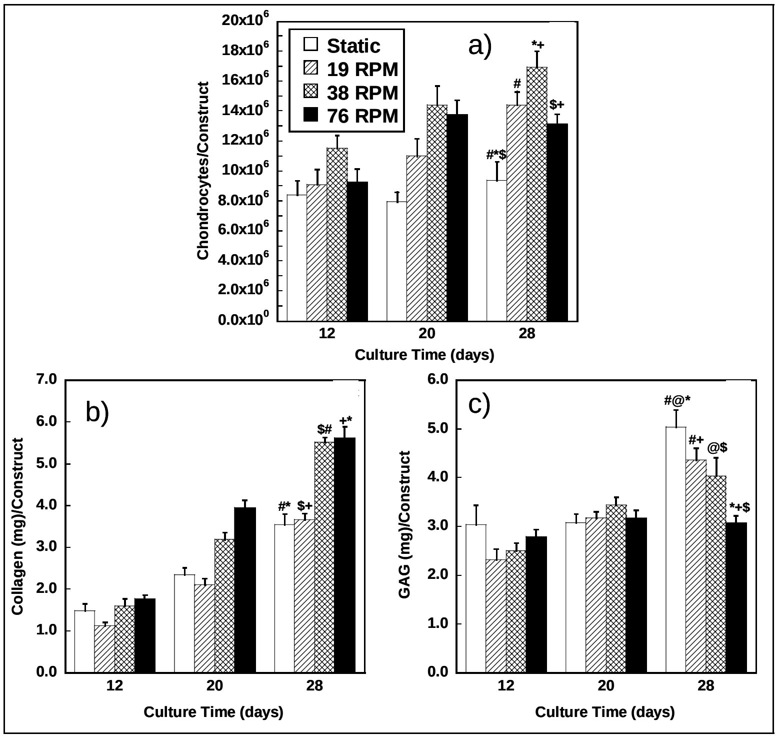

Figure 1.9: a) Chondrocytes; b) collagen; and c) GAG content of cartilage tissue constructs grown in a concentric-cylinder bioreactor (Saini and Wick, 2003).

within bioreactors plays a major role in determining the eventual structure of tissue-engineered cartilage. It affects mass-transfer rates of critical components such as oxygen, carbon dioxide, and nutrients as well as elicits a physiological response from the growing tissue as exhibited by its influence on GAG production. An additional consideration in subjecting tissues to the dynamic environment with a bioreactor is the fragility of mammalian cells. Because tissues grown *in vitro* are fixed on scaffolds (or, in other applications, on microcarrier beads), the relative motion between the static tissue and the agitated fluid medium generated by the mixing exposes the cells to shear and normal stresses. One must insure that these stresses are *locally* below levels that can cause harm to the growing tissue. Thus, it can be argued that to predict the behavior of tissues cultured within bioreactors, one must understand both the local environment experienced by these tissues and the cause-and-effect relationship between the environment characteristics and the growing tissue. This, in turn, requires detailed knowledge of both, the flow field in the vicinity of tissue constructs and the changes in the flow field induced by the synthesis of extracellular matrix on the construct surfaces. Existing studies are few.

Experimental investigation of the flow field within a spinner-flask bioreactor as employed for tissue culture on microcarrier beads has been conducted by Venkat et al. (1996). The vessel contained microcarrier beads and the flow was observed using stereo particle tracking velocimetry. Different impeller regimes were studied, corresponding to varying shear intensities. This work provided details on the velocity field in critical regions of the reactor. Three flow domains could be identified: a tangential bulk flow generated by the stir bar, a trailing vortex region at the tip of the bar and a converging flow region near the center of the vessel. The study focused on the last two regions characterized by high velocity gradients and thus particularly relevant to microcarrier cultures. The assessment of the cell damage level was approximated by calculating the dissipation function (i.e., the rate of work done on a fluid element).

Brown (1998) designed an experimental setup capable of quantifying the laminar fluid environment within a rotating-wall bioreactor in the absence of living tissues. The flow field was investigated via flow visualization and particle-image velocimetry (PIV). A model bioreactor and model scaffolds had to be designed in order to provide the optical access required by the PIV technique while meeting the dynamic similarity requirement with the vessel prototype. A MATLAB code based on an algorithm initially developed by Bernal (1996) was used to perform the cross-correlation routine, yielding the velocity fields and the shear-rate fields in the vicinity of the suspended model construct. Different flow cases were produced by imposing synchronous (i.e., two cylinders rotating at the same angular velocity) or differential (i.e., two cylinders rotating at different rates) cylinder rotations, in the same or opposite directions, for a range of angular velocities (from 13 to 37 rpm for the inner cylinder, from 13 to 20 rpm for the outer cylinder). The PIV experiments focused on the flow regimes compatible with tissue culture. Three types of construct motions could be identified: i) relatively stationary position near the outer cylinder; ii) relatively stationary position near the inner cylinder, and iii) orbital rotation about a fixed point in the flow. PIV provided qualitative results in good agreement with flow visualizations. The experiments also yielded relevant quantitative data regarding the shear-rate level in the vicinity of and on the surface of the tissue construct. High shear-rate levels were obtained near the edges of the construct, at the intersection between the flat and the cylindrical surfaces.

Computational-fluid-dynamics (CFD) simulations performed by Neitzel et al. (1998) provided additional insight to the flow field characterization within rotating bioreactors. A three-dimensional vessel similar to the reactor used by Brown (1998) was modeled computationally using the commercial CFD package FLUENT. The construct was approximated as a stationary solid in the annular gap, at a location determined from the previous flow-visualization results for a case of differential rotation. A refined mesh was used in the vicinity of the construct in order to enhance the reliability of the numerical results. The boundary conditions for the inner and outer walls were set to simulate a viable tissue-growth environment, in accordance with previous observations made by Brown (1998). The computed results (velocity and shear-rate fields) showed good qualitative and quantitative agreement with the experimental PIV measurements discussed above. The model could then be exploited to calculate other quantities relevant for tissue-growth *in vitro*. Mass-transfer computations were performed to resolve the concentration of critical nutrients such as dissolved oxygen within the annular gap of the vessel. The results pointed out the influence of the flow field on the concentration boundary layers localized at the surface of the model scaffold.

Begley and Kleis(2000) employed numerical methods to investigate the flow field within a rotating-wall, perfused vessel fitted with a so-called viscous pump. The viscous pump is a solid disk mounted near one end of the reactor and rotated differentially with respect to the main body, acting as a centrifugal pump to circulate culture medium within the reactor, especially under conditions of microgravity. Their model, validated against laser-Doppler velocimetry measurements, was used to predict flow characteristics such as streamlines and mean shear-stress levels under both microgravity and terrestrial operating conditions.

Finally, computational fluid dynamics methods have also been applied to the flow field within a roller-bottle bioreactor. Unger et al. (2000) have performed simulations using the commercial software package FLUENT for both creeping- and inertial-flow conditions. The observation of the velocity fields revealed the influence of the vessel endwalls on the axial fluid mixing.

Although the above studies have enhanced our knowledge of the dynamic environment produced within those bioreactors, efforts to characterize the flow environment produced within spinner flasks are few. The understanding of the tissue-growth process in such devices would benefit from the design of a computational model capable of predicting the flow in this complex geometry and would help studying the local flow effects on tissue growth.

Objectives

As suggested by the studies cited earlier, the optimization of techniques for producing high-quality tissue depends on the knowledge of the relationships between the growing tissue and the growth environment. More specifically, in bioreactors generating the motion of the culture medium with respect to a freely moving or fixed construct, studies have shown that GAG production correlates with the fluid shear stress (Neitzel et al., 1998; Saini and Wick, 2003). From this observation, a hypothesis can be inferred that the production of a functional tissue with the desired properties requires the detailed knowledge of the relationship between the production of critical cartilage structural components (mainly, GAG and type-II collagen) and shear stress. This knowledge transcribed into a validated numerical model would also permit one to investigate new bioreactor designs.

This thesis addresses the design of a CFD-based tissue-growth model for cartilage in a spinner-flask bioreactor. The fluid flow produced in a dynamically similar vessel will be characterized using particle-image velocimetry (PIV). A computational flow model will be developed and validated with respect to the accompanying laboratory measurements. This model will permit the computation of the shear stresses on the surfaces of the constructs placed in the bioreactor. In parallel, cartilage tissue will be grown in the prototype spinner flask. Construct histologies and GAG content will be analyzed and correlated to the shear-stress levels predicted by the CFD model. The integration of this correlation into the numerical model will enable the prediction of cartilage growth (in terms of GAG synthesis) in the presence of convective effects generated within such a device. Eventually, the diffusive effects to cartilage formation within the constructs will be accounted for by coupling the CFD-based growth model to the model developed by Obradovic et al. (2000). The resulting convective-diffusive model will constitute a predicting tool for cartilage growth in spinner-flask bioreactors.

CHAPTER 2

PARTICLE-IMAGE VELOCIMETRY: PRINCIPLES AND DEVELOPMENTS

Particle-image velocimetry

Description

The experimental description of the flow field was carried out using particle-image velocimetry (PIV) (Adrian, 1991; Willert and Gharib, 1991). This optical method is capable of determining the instantaneous velocity vector field in a two-dimensional environment. Image acquisition and image processing constitute the two main steps (**Figure 2.1**). Schematically, the flow is seeded with small tracer particles and illuminated with a sheet of laser light. A camera

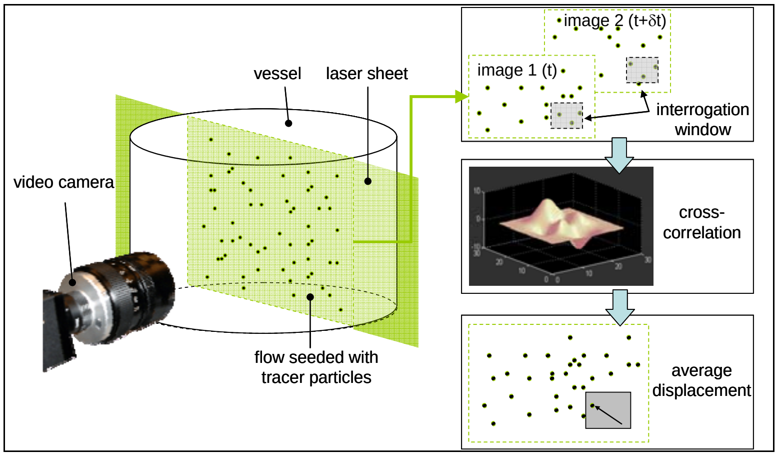

Figure 2.1: Description of the PIV technique. The flow is seeded with tracer particles and a cross-section is illuminated with a laser sheet. A video camera placed perpendicular captures an image pair in a time interval δt. The cross-correlation of small interrogation windows created in both images yields the mean displacement of the particles contained within this region during δt. Repeating this procedure over the entire surface of each image yields the instantaneous-displacement field at the time the first image was captured.

captures image pairs at a given frequency. The displacement function of the tracer particles describing their motion from the first image of one pair to the second image of the same pair can be calculated by the statistical technique of spatial cross-correlation (Keane and Adrian, 1992; Willert and Gharib, 1991). The cross-correlation coefficient is an indicator of the matching of the particles with themselves between the two individual pictures of one image pair. The higher the cross-correlation coefficient, the more particles match up with their spatially shifted images. Therefore, the location of the highest peak with respect to the origin determines the average spatial displacement of the particles in that region. The knowledge of the mean displacement of the particles between two images and the image capture frequency enables the calculation of the mean-velocity field in that region. Once the sampling domain has been cross-correlated, the window is then shifted to a neighboring region that overlaps the previous one. By repeating this process, the cross-correlation can be performed over the entire image yielding the instantaneous flow velocity at the time the first picture of the pair was captured.

Common issues

Because of issues such as the noise caused by the particles moving off the edges of the sampling region or those disappearing due to three-dimensional motions in the laser sheet, the characteristics of the grid geometry and interrogation window are crucial in the implementation of cross-correlation.

The PIV grid is a rectangular grid consisting of equidistant points at which the flow velocity is calculated. The spacing between consecutive points determines the resolution of the results. Because the resolution in turn affects the dependence of neighboring velocity estimates as described later, the choice of a small grid spacing might not produce the most accurate results.

The interrogation window is the domain centered on a grid point in which cross-correlation is performed. After the location of the cross-correlation peak has been determined and the mean velocity deduced, the center of the sampling window is shifted to the next grid point.

Therefore, the size of the interrogation window is an important factor that controls not only the size of the domain over which cross-correlation is performed but also the overlap between two successive windows, two parameters found critical for successful PIV measurements (Adrian, 1991; Keane and Adrian, 1992; Westerweel, 1997; Willert and Gharib, 1991). In fact, the reliability of the cross-correlation results depends on the number of matching particles located in two temporally-shifted interrogation windows (i.e., windows of similar size, centered on the same grid point, but generated on two successive PIV frames). The presence of a small number of matching particles prevents the accurate determination of the mean-displacement (or mean-velocity) estimate. Therefore, the seeding density, the size, and the average velocity of the tracer particles must be accounted for in the definition of the sampling window size. In addition, the overlap defines the degree of dependence between the velocity vectors calculated at neighboring grid points. For a square interrogation window, the percentage overlap is calculated as

$$\text{overlap} = 100\left(1 - \frac{\Delta x}{\Delta l}\right), \tag{2-1}$$

where Δx is the grid spacing and Δl is the side length of the sampling domain. The more overlapped two consecutive interrogation windows, the more similar the set of tracer particles they contain. Therefore, a compromise has to be found between grid spacing and interrogation window size that maximizes the resolution of the results and minimizes the dependence of consecutive results. Studies have shown that in most flows, 50%- or 75%-overlapped interrogation windows of 32 × 32 pixels comply with this requirement for acceptable computation times.

Phase-locking and ensemble-averaging

The flow produced in the spinner flask was expected to be fully turbulent ($\mathrm{Re} = 1760$, as calculated in Chapter 1). Because the principal characteristic of such flows is randomness (Tennekes and Lumley, 1972), their description by the PIV technique requires the development of specific experimental protocols and tools based on statistical methods. The complex geometry of the bioreactor prevented the flow from being isotropic or even homogeneous, making space averaging inappropriate. Likewise, because the flow was turbulent and unsteady in the mean, the determination of mean and turbulent flow quantities required the use of ensemble, rather than time, averaging (Bradshaw, 1971). Each ensemble represented the flow at a given stir-bar orientation; averaging the velocity at each point in the flow field over several ensembles permitted the determination of the appropriate mean and fluctuating velocities at each point. Ensemble averaging further required that measurements be phase-locked, i.e., timed to the precise location of the stir bar at each time an image pair was captured by the system.

Initial PIV software

Brown (1998) adapted a cross-correlation algorithm initially developed by Bernal (1996) to the processing of single-exposure double-frame digital data to characterize the laminar flow field in the vicinity of model-tissue constructs within a rotating-wall bioreactor. The initial algorithm consisted of three separate subroutines, i.e., pre-processing, cross-correlation, and post-processing of the PIV data.

The pre-processing routine consisted of the acquisition of the flow and PIV parameters in a graphical-user interface shown in **Figure 2.2**. During this step, the number of image pairs, the fluid properties, and the frame resolution could be entered. The quality of the captured images could be enhanced optionally in terms of brightness, contrast, and gamma correction. More importantly, this step included the definition of the PIV grid geometry and the sampling window characteristics.

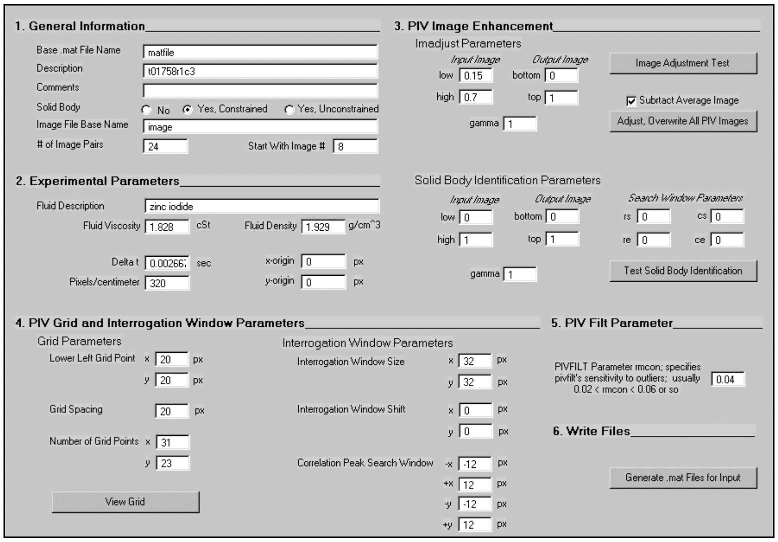

1. General Information
Base .mat File Name: matfile
Description: t01758r1c3
Comments:
Solid Body: ○ No ● Yes, Constrained ○ Yes, Unconstrained
Image File Base Name: image
\# of Image Pairs: 24
Start With Image #: 8

2. Experimental Parameters
Fluid Description: zinc iodide
Fluid Viscosity: 1.828 cSt
Fluid Density: 1.929 g/cm^3
Delta t: 0.00266 sec
x-origin: 0 px
Pixels/centimeter: 320
y-origin: 0 px

3. PIV Image Enhancement
Imadjust Parameters
Input Image
low: 0.15
high: 0.7
Output Image
bottom: 0
top: 1
gamma: 1
☑ Subrtact Average Image

Solid Body Identification Parameters
Input Image
low: 0
high: 1
Output Image
bottom: 0
top: 1
gamma: 1
Search Window Parameters
rs: 0
cs: 0
re: 0
ce: 0

4. PIV Grid and Interrogation Window Parameters
Grid Parameters
Lower Left Grid Point x: 20 px
y: 20 px
Grid Spacing: 20 px
Number of Grid Points x: 31
y: 23

Interrogation Window Parameters
Interrogation Window Size x: 32 px
y: 32 px
Interrogation Window Shift x: 0 px
y: 0 px
Correlation Peak Search Window -x: -12 px
+x: 12 px
-y: -12 px
+y: 12 px

5. PIV Filt Parameter
PIVFILT Parameter rmcon; specifies pivfilt's sensitivity to outliers; usually 0.02 < rmcon < 0.06 or so: 0.04

6. Write Files

Figure 2.2: Graphical-user interface used for the input of the PIV and flow parameters required for cross-correlation.

The standard cross-correlation method commonly used in two-dimensional PIV had to be modified to account for the presence of a construct in the flow. In fact, the presence of a solid boundary in the interrogated sub-regions of two successive frames inhibited the displacement of the tracer particles, resulting eventually in an erroneous location of the correlation peak. This issue particularly relevant for the cross-correlation analysis was solved by using a masking technique. Prior to PIV processing, a binary image of the solid body was constructed with MATLAB image-processing functions; this was then eliminated from each image (**Figure 2.3**). Grid points falling within the construct were systematically assigned zero fluid velocity. The velocity components at all other points were determined by correlating corresponding interrogation windows at a given grid point using a Fast Fourier Transform (FFT). Fitting a Gaussian curve to the correlation peak allowed the determination of the average particle-image displacement, to sub-pixel accuracy. The raw velocity field obtained by the systematic application of this analysis to all the grid points of an image pair could then be filtered by performing an average over neighboring points in order to avoid missing data, and by applying a median filter in order to reduce measurement noise.

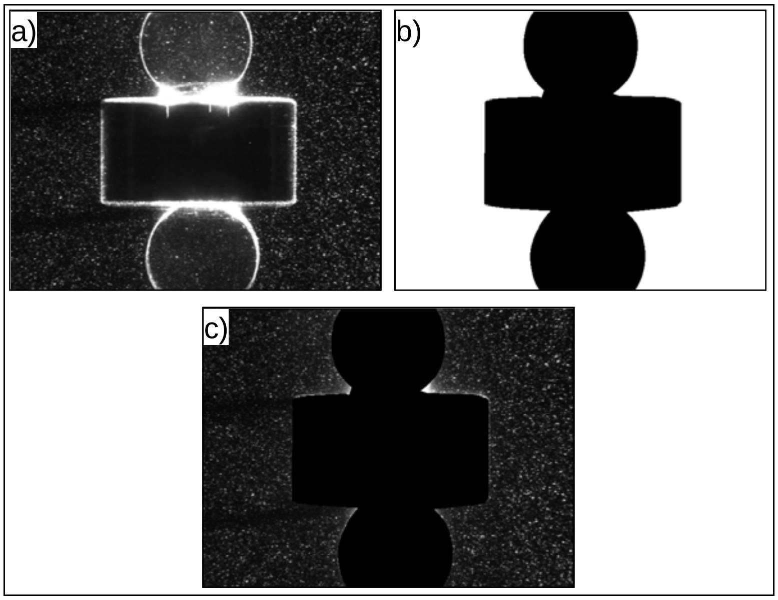

Figure 2.3: Typical images of the flow around a construct at different steps of the PIV processing: a) image captured by the frame grabber; b) binary image of the solid body; and c) image synthesized by subtraction of the binary image (b) from the unprocessed image (a), and suitable for cross-correlation.

The analysis of the resulting data consisted of two MATLAB subroutines. The first one allowed the visualization of the instantaneous velocity-vector field $\tilde{\mathbf{U}}_{\mathbf{ij}}(\mathbf{x},t)$ in the PIV grid contained in the plane $(\mathbf{e_i},\mathbf{e_j})$. The second consisted of the calculation and visualization of the instantaneous shear stress component contained within the PIV plane defined as

$$\tilde{\tau}_{ij}(\mathbf{x},t)=\mu\left[\frac{\partial\tilde{U}_i(\mathbf{x},t)}{\partial x_j}+\frac{\partial\tilde{U}_j(\mathbf{x},t)}{\partial x_i}\right], \tag{2-2}$$

where μ is the dynamic viscosity and $\tilde{U}_i$ and $\tilde{U}_j$ are the velocity components in the $\mathbf{e_i}-$ and $\mathbf{e_j}-$directions, respectively, of the instantaneous velocity $\tilde{\mathbf{U}}_{\mathbf{ij}}(\mathbf{x},t)$. The shear stress field was calculated at each grid point using second-order accurate finite-differences. Grid points at the edge of the fluid domain (i.e., on the border of the user-defined grid) were processed with backward and forward differences, as required.

Overview of new program features

Although the original code was shown to yield acceptable velocity estimates in flows without solid bodies, or in the bulk of flows containing solid bodies, improvements needed to be made to obtain accurate velocity measurements near solid walls. In addition, because the calculation of shear stresses in the vicinity of the constructs was of particular interest in this work, new computational methods producing reliable velocity-gradient estimates had to be investigated. Finally, the initial PIV software had to be adapted to the treatment of phase-locked PIV realizations. For this purpose, post-processing routines were designed and ensemble-averaging capabilities were added to the original code.

In the new PIV software, "DoctorPiv plus", the production of instantaneous, ensemble-averaged velocity fields was carried-out by averaging the velocity data obtained by cross-correlation at each grid point (i.e., $\tilde{\mathbf{U}}_{\mathbf{ij}}\left(\mathbf{x},t\right)$) over a certain number of realizations. This procedure made possible by the capture of the PIV frames in phase-locked mode resulted in a unique series of data, each containing the ensemble-averaged velocity field at an instant of time, i.e.,

$$\bar{\mathbf{U}}_{\mathbf{ij}}\left(\mathbf{x},t\right)=\frac{\sum_{n=1}^{n_r}\tilde{\mathbf{U}}_{\mathbf{ij}}\left(\mathbf{x},t;n\right)}{n_r}, \qquad (2\text{-}3)$$

where n_r is the number of PIV realizations.

The specific flow produced in the spinner flask also had to be characterized in terms of turbulent quantities. The knowledge of the instantaneous and average velocity fields at each instant of time allowed the calculation of the fluctuating velocity field as

$$\mathbf{u_{ij}}\left(\mathbf{x},t\right)=\tilde{\mathbf{U}}_{\mathbf{ij}}\left(\mathbf{x},t\right)-\bar{\mathbf{U}}_{\mathbf{ij}}\left(\mathbf{x},t\right). \tag{2-4}$$

From the knowledge of the velocity fluctuations, other turbulent quantities could be determined such as the Reynolds stress component contained in the PIV plane and expressed as

$$\tau_{ij}(\mathbf{x},t)=\overline{\rho u_i(\mathbf{x},t)u_j(\mathbf{x},t)}, \tag{2-5}$$

where the overbar denotes ensemble-averaged quantities.

Finally, a graphical-user interface was designed in order to simplify the input of the PIV parameters and to integrate all the routines involved in the PIV technique (i.e., image processing, folders management, PIV inputs, ensemble-averaging, and data visualization) within a unique graphic window (**Figure 2.4**).

The graphic interface featured a viewer to monitor in real time the cross-correlation process (in terms of the percentage of bad and spurious data points contained in the PIV grid of an image pair) as well as the visualization of the computed quantities of interest.

Adapted cross-correlation

The initial cross-correlation routine developed by Bernal (1996) yielded the mean displacement (and hence, the mean velocity) of the particles contained in an interrogation window centered on a grid point, and assigned this displacement (or velocity) to the center of that window. This calculation is considered valid as long as the seeding particles present in the fluid

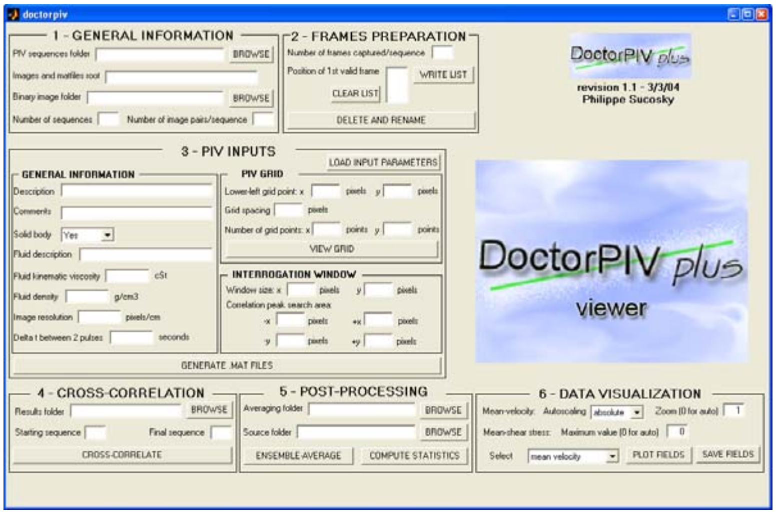

Solid body: Yes

Mean-velocity: Autoscaling: absolute; Zoom (0 for auto): 1

Mean-shear stress: Maximum value (0 for auto): 0

Select: mean velocity

Figure 2.4: "DoctorPiv plus" graphical-user interface used to manipulate the inputs required for cross-correlation. An integrated viewer allows the visualization of the data calculated at each step of the processing.

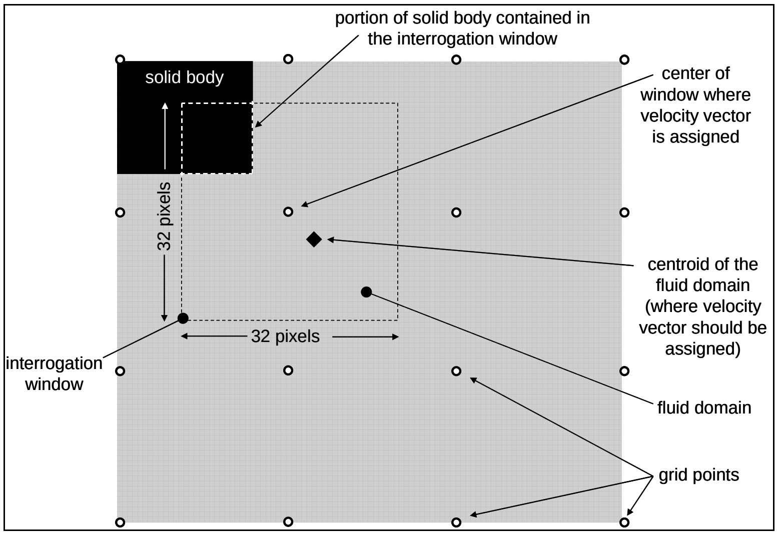

Figure 2.5: Error generated by standard cross-correlation in velocity-vector positioning near a solid wall. The mean displacement of the particles seeding the fluid domain of the 32×32-pixel interrogation window should be assigned to the centroid of this domain rather than to the centroid of the window.

occupy the entire interrogated region and are homogeneously distributed over that region. If the window is partially occupied by a solid, it is more reasonable to assign the mean displacement calculated by cross-correlation to the centroid of the region within the window occupied by fluid rather than the center of the interrogation window (**Figure 2.5**), since it is the fluid that contains the tracer particles whose correlation peak is being determined. This statement is justified if the seeding particles are homogeneously distributed over the fluid domain, which is a necessary hypothesis in PIV measurements. In an effort to improve the accuracy of the velocity estimates in the vicinity of constructs, the original code was modified in that sense. The precise location of the velocity vectors calculated near the wall was determined by the adapted cross-correlation technique whose flowchart is reported in **Figure 2.6** and complete description is as follows.

After the binary image of the solid body was constructed and subtracted from each image pair, the coordinates of each grid point stored in two matrices, $[x_{i\ rs}]$ and $[x_{j\ rs}]$ (where r and s are the number of grid points along the vertical and horizontal directions, respectively), were tested. Zero velocity was assigned to the grid points contained within the solid body (i.e., black pixels on the binary image) whereas the standard FFT cross-correlation was performed for all other grid points falling in the fluid region (i.e., white pixels on the binary image). A local binary image (i.e., essentially a sub-region of the full-size binary image created prior to PIV processing) centered on a grid point and of the same size as the interrogation window was constructed for each grid point falling in the fluid domain. In this image, any construct part was displayed as a black region and any fluid domain as a white region. The standard cross-correlation routine needed not be modified if this binary image contained a fluid domain only since the centroid of the fluid region also corresponded to the center of the interrogation window, and hence, to the grid point itself. On the contrary, when the binary image contained some black and white pixels, the code had to be adapted. The local binary image was processed by a MATLAB subroutine that calculated the centroid coordinates of the fluid region. Standard cross-correlation was performed

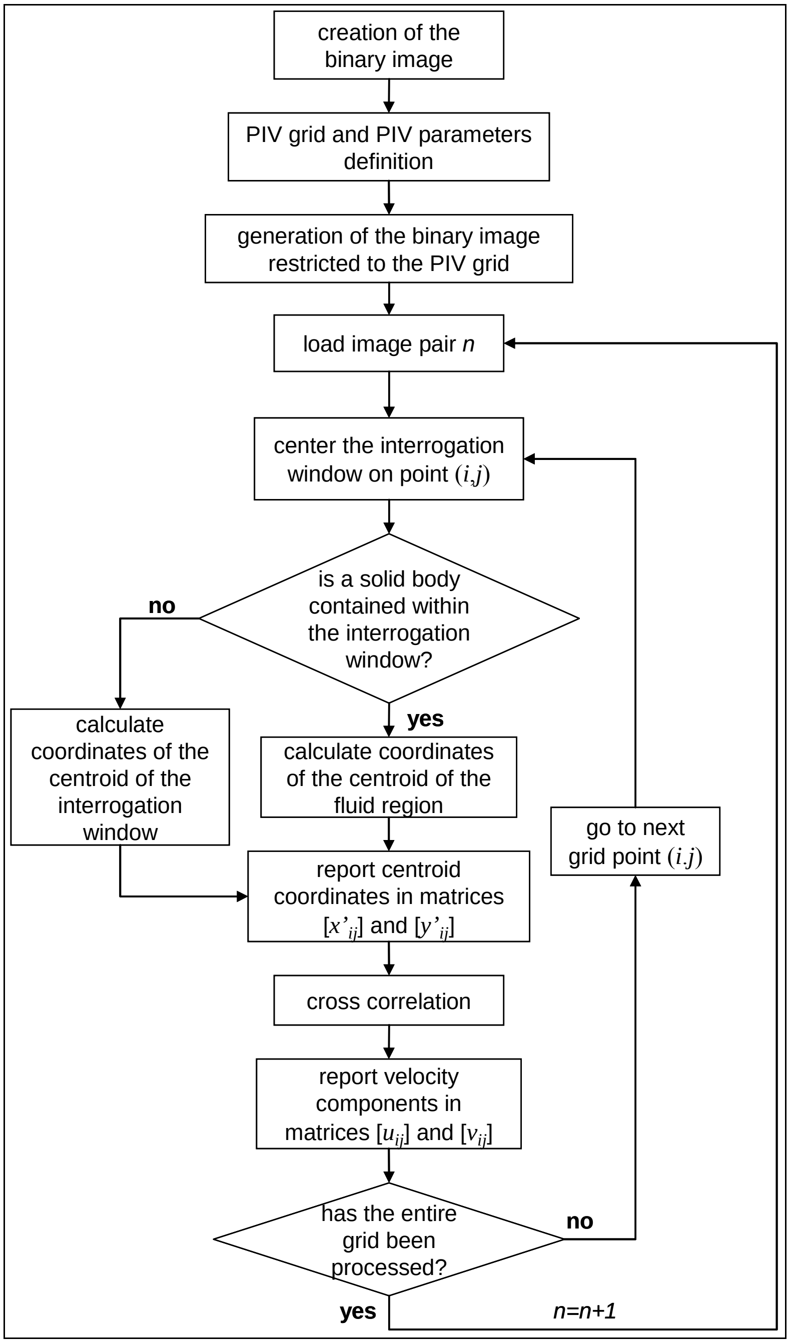

Figure 2.6: Flowchart of the new "DoctorPiv plus" algorithm based on adapted cross-correlation.

and the resulting mean-displacement vector of the particles was assigned to this location. As a result, four matrices were generated: $[x'_{i\,rs}]$ and $[x'_{j\,rs}]$ containing the x_i- and x_j-coordinates of each velocity-vector location, and $[\tilde{U}_{i\,rs}]$ and $[\tilde{U}_{j\,rs}]$ containing the x_i- and x_j-components of the velocity vectors at each point of coordinates $\left(x'_{i\,rs}, x'_{j\,rs}\right)$. The matrices $[x_{i\,rs}]$ and $[x_{j\,rs}]$ only differed from $[x'_{i\,rs}]$ and $[x'_{j\,rs}]$ for the grid points where the adapted cross-correlation routine had to be performed (i.e., grid points for which the local binary image contained both a fluid and a solid-body domains). For all other points far enough from the wall, $x_{i\,rs} = x'_{j\,rs}$ and $x_{j\,rs} = x'_{j\,rs}$. Consequently, as compared with the initial Cartesian grid, the velocity data calculated with the adapted cross-correlation were defined *a priori* on a non-rectangular and non-equally spaced grid defined by the rectangular matrices $[x'_{i\,rs}]$ and $[x'_{j\,rs}]$.

Tests and validation

The validity of the new cross-correlation algorithm was investigated using synthetic PIV images of a Couette flow on an inclined plane (10-degree slope) whose layout is described in **Figure 2.7**. The inclination with respect to the grid insured that the difficulties encountered with the previously used PIV algorithm were present. Two 640×480-pixel synthetic images simulating the presence of 3,000 tracer particles randomly positioned within the field were constructed using a MATLAB program. The PIV computation was performed using a 32×32-pixel interrogation window on a grid containing 1,632 points equally spaced by 8 pixels, resulting in a 75% overlap between two adjacent interrogation windows. A comparison between the velocity-vector field obtained in the vicinity of the wall with the initial algorithm and that calculated with the new algorithm is shown in **Figure 2.8a** and **Figure 2.8b**, respectively. The displayed fields occupy a region of 133×100 pixels. The exact location of the wall is indicated by a solid line. As expected, the velocity vectors are parallel to the wall and their magnitude increases linearly with distance

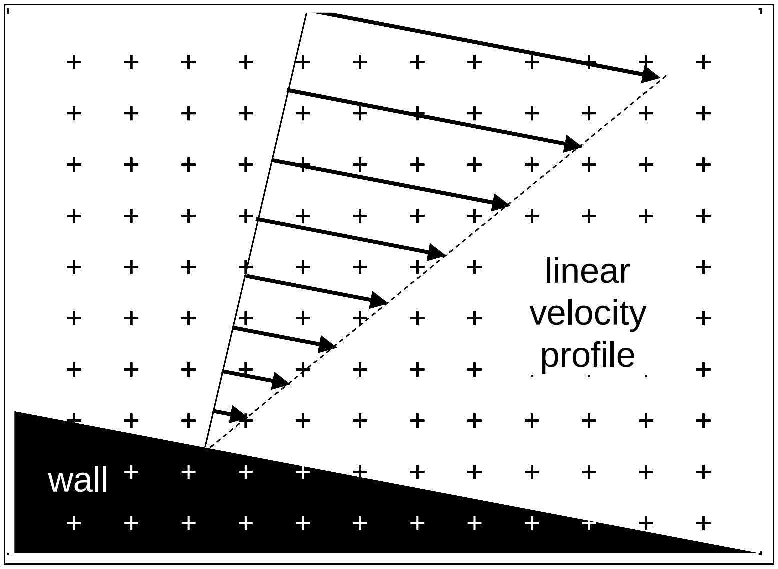

Figure 2.7: Schematic of the Couette-flow configuration used to generate the PIV synthetic images. The flow is from left to right and the plane has a 10-degree slope with respect to the horizontal. Theoretically, the velocity vector at any point in the flow is parallel to the plane and its magnitude increases linearly with the normal distance from the wall.

normal to the wall. The orientations and magnitudes of the velocity vectors obtained with the two cross-correlation techniques are similar since the velocities were calculated based on the same sets of tracer particles. The locations of the velocity vectors produced by the two techniques are similar in the bulk of the flow where the data points are regularly spaced and aligned on the PIV grid. In the field produced by the new code, one can notice the displacement of the first two points closest to the wall to a corrected location. **Figure 2.9** shows the velocity magnitude obtained with the new and the old algorithm along a column of the PIV user-defined grid (i.e., in the vertical direction) as compared to the theoretical magnitude. Good qualitative and quantitative greements were obtained between the theoretical and the PIV-processed fields. The calculation of the RMS error confirmed the better performance of the adapted cross-correlation (RMS error = 0.228 pixel/s) over the old algorithm (RMS = 0.249 pixel/s).

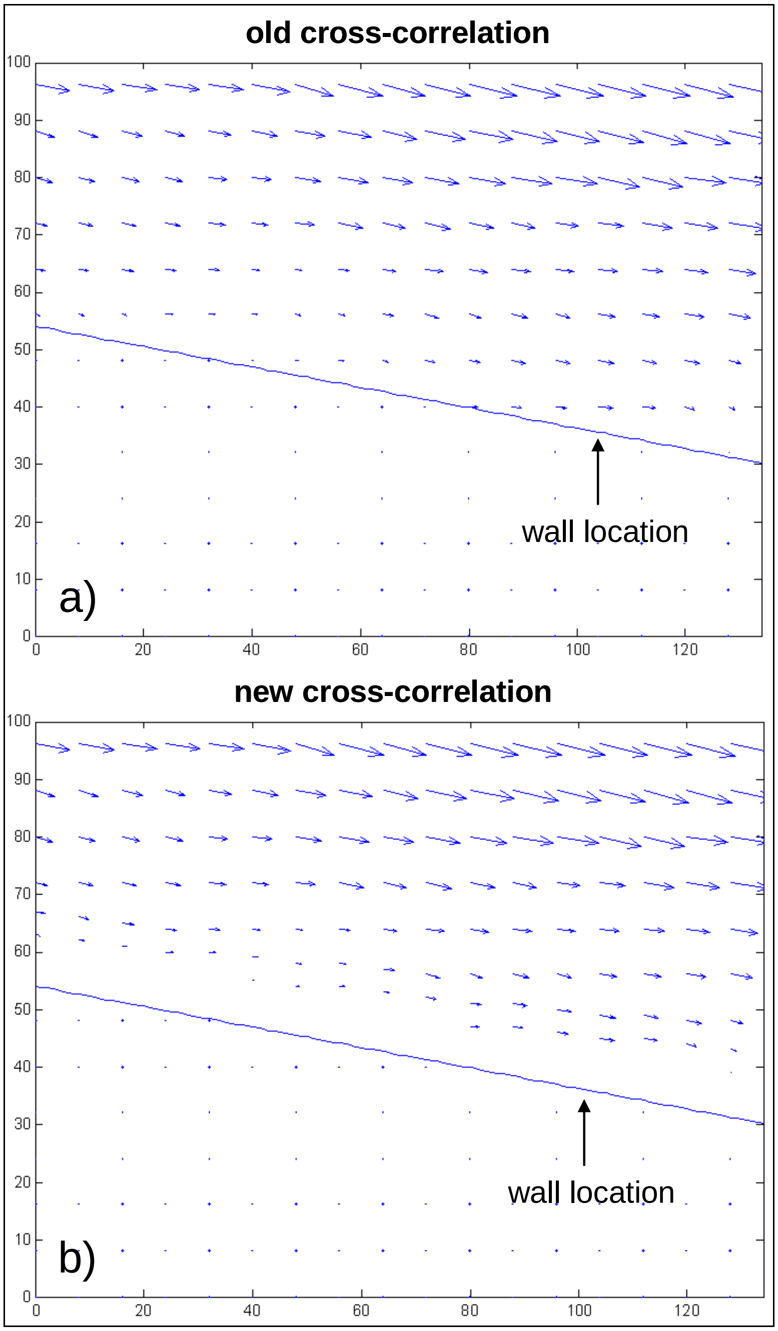

Figure 2.8: Comparison between the velocity measurements based on synthetic PIV images obtained with: a) the unmodified code; and b) the adapted cross-correlation algorithm.

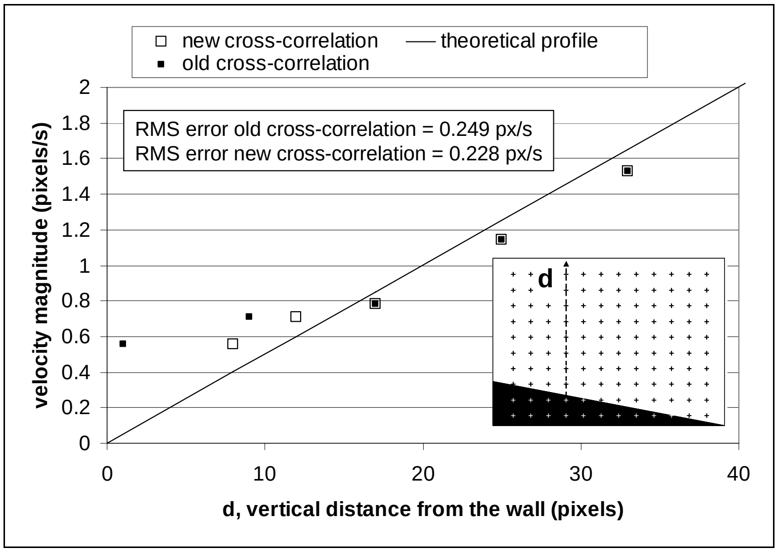

Figure 2.9: Comparison between the theoretical (solid line) and the measured velocity magnitude with the old (black squares) and new (white squares) cross-correlation, as a function of the vertical distance from the wall (d).

Shear-stress calculation

Issues

The velocity measurements obtained with PIV were used to estimate the mean-shear stress component contained in the plane illuminated by the laser sheet, i.e.,

$$\bar{\tau}_{ij}\left(\mathbf{x},t\right)=\mu\left[\frac{\partial \bar{U}_i\left(\mathbf{x},t\right)}{\partial x_j}+\frac{\partial \bar{U}_j\left(\mathbf{x},t\right)}{\partial x_i}\right]. \tag{2-6}$$

The numerical evaluation of this expression required the spatial velocity gradients to be discretized over the grid where the velocity components had been measured. As explained earlier, the grid produced by the adapted cross-correlation procedure contained non-equally spaced points located near solid boundaries, which made the discretization of **Equation (2-6)** more difficult. Since the wall-shear stress was a critical quantity in this work, a specific differentiation method had to be developed. However, one should note that the standard PIV technique is not capable of producing accurate estimates of the spatial velocity gradients. The principal difficulty arises from the lack of resolution that prevents the complete determination of the velocity profile between the solid boundary where the velocity is zero and the first PIV-grid point where the velocity is calculated by cross correlation. Among other issues, the difficulty in precisely locating the construct edges in the observed flow and the errors caused by measurement noise are the most critical. Although complex interpolation methods could be developed to estimate the unknown velocity field near solid walls, the calculation of the wall-shear stress would be biased by the choice of the interpolation scheme. In an effort to produce fair shear-stress estimates while maintaining low computational costs, a simple differentiation method based on finite differences was developed.

Method

The numerical scheme adopted for the calculation of the mean-shear stress consisted of two steps: the interpolation of the velocity information obtained by the adapted cross-correlation on the non rectangular, non-equally spaced grid onto the original grid defined by the user prior to cross-correlation, and the calculation of the spatial gradients of the resulting interpolated velocity field.

The interpolation of the velocity field was achieved using a thin-plate smoothing spline. The *tpaps* function featured in the spline toolbox 3.1.1 of MATLAB 6.5 (release 13) was used for this purpose. This function constructs a thin-plate spline function f that satisfies exactly the equation $Z = f\left(x_i', x_j'\right)$ for prescribed values Z at scattered data sites $\left(x_i', x_j'\right)$ in the plane. In the present application, two spline functions $f_{\tilde{U}_i}$ and $f_{\tilde{U}_j}$ had to be constructed for the interpolation of the x_i- and x_j-components of the velocity field, respectively. Two sets of prescribed values, $Z_{\bar{U}_i}$ and $Z_{\bar{U}_j}$, containing the velocity information calculated by adapted cross-correlation, had to be used. The thin-plate spline produced by *tpaps* can be expressed as:

$$f(\mathbf{x}) = \sum_{b=1}^{n_c} a_b \psi\left(\mathbf{x} - \mathbf{c_b}\right) \tag{2-7}$$

where $\mathbf{x}$ is an arbitrary point of coordinates $\left(x_i, x_j\right)$, $\left(a_b\right)$ is a set of n_c unknown coefficients, ψ is the basis function and $\left(\mathbf{c_b}\right)$ is the set of n_c prescribed sites of coordinates $\left(x'_{i_b}, x'_{j_b}\right)$ where the measured velocity value Z_b satisfies:

$$f\left(\mathbf{c_b}\right) = Z_b \quad , \quad \forall b \in \left[1 \;\; n_c\right]. \tag{2-8}$$

For the current application, the prescribed sites consisted of a point relocated by the adapted cross-correlation procedure, and eight, five, or three surrounding grid points, depending on the position of the point on the grid (i.e., in the middle of the grid, on a border, or at a corner, respectively). One of the requirements for the construction of this interpolating surface is the minimization of the energy function $E(f)$, defined as:

$$E\left(f\right) = \iint_{\Re^2} \left(\frac{\partial^2 f}{\partial {x_i}^2}\right)^2 + 2\left(\frac{\partial^2 f}{\partial x_i \partial x_j}\right)^2 + \left(\frac{\partial^2 f}{\partial {x_j}^2}\right)^2 dx_i dx_j \tag{2-9}$$

This condition is automatically satisfied if the basis function ψ is defined at any point $\mathbf{x}$ as:

$$\psi(\mathbf{x}) = \|\mathbf{x}\|^2 \log\left(\|\mathbf{x}\|^2\right) \tag{2-10}$$

Substituting (2-10) into (2-7) yields the complete form of the thin-plate spline:

$$f(\mathbf{x}) = \sum_{b=1}^{n_c} a_b \left\|\mathbf{x} - \mathbf{c_b}\right\|^2 \log\left(\left\|\mathbf{x} - \mathbf{c_b}\right\|^2\right) \tag{2-11}$$

The condition imposed by the coordinates of each prescribed point **c** is:

$$Z_g = \sum_{b=1, b\neq g}^{n_c} a_b \left\|\mathbf{c_g} - \mathbf{c_b}\right\|^2 \log\left(\left\|\mathbf{c_g} - \mathbf{c_b}\right\|^2\right) \quad , \quad \forall g \in \left[1 \;\; n_c\right] \tag{2-12}$$

By introducing the collocation matrix $[\psi_{bg}]$,

$$\psi_{bg} = \left\|\mathbf{c_g} - \mathbf{c_b}\right\|^2 \log\left(\left\|\mathbf{c_g} - \mathbf{c_b}\right\|^2\right), \tag{2-13}$$

condition (2-12) can be expressed as:

$$Z_g = \sum_{b=1}^{n_c} a_b \psi_{\mathrm{bg}} \quad , \quad \forall g \in \left[1 \;\; n_c\right] \tag{2-14}$$

Therefore, the determination of the interpolating thin-plate spline involved the solution of a linear system of n_c equations with n_c unknown coefficients $\left(a_b\right)$. By repeating this process at each point whose coordinates have been modified by the adapted cross-correlation, the interpolated mean-velocity field could be obtained on the rectangular and equally-spaced PIV grid initially defined by the user. The shear rate was then estimated by applying second-order-accurate finite differences at each grid point falling in a fluid region.

Concluding remarks

The PIV software written by Brown (1998) was supplemented with important features to permit the experimental investigation of the turbulent flow produced in the spinner flask. Ensemble-averaging capabilities have been developed in order to allow the analysis of phase-locked PIV realizations. The velocity calculation was significantly improved in the vicinity of solid boundaries thanks to the design of an adapted cross-correlation code. Although difficulties remain for the calculation of the spatial velocity gradients in those regions, a comprehensive method has been developed to assess shear stress levels. Finally, the program was added a graphic interface that simplified the manipulation of the inputs and results, and significantly reduced the processing time of the PIV data.

CHAPTER 3

EXPERIMENTAL FLOW CHARACTERIZATION

Bioreactor model

The reliability and accuracy of the PIV technique depend not only on the cross-correlation algorithm but also on the quality of the optical system. PIV requires the illumination of a section of the flow with a thin laser sheet. Therefore, its application to the determination of the velocity field within the spinner-flask bioreactor required some design modifications.

The circular geometry of the spinner-flask prototype raised some important issues. First, an incident laser sheet is partially reflected when hitting the curved outer surface of the reactor. In addition, when filled with culture medium, the bioreactor did not allow a direct observation of the actual flow field because of the deformation caused by the refraction of light at the wall-fluid interface. Finally, the culture medium used in the actual bioreactor contains quantities that render it less than completely transparent. Its opacity would have prevented the laser sheet from penetrating with enough intensity into the vessel. In order to improve optical access, a model bioreactor with flat, perpendicular outer walls made of a transparent material was designed. The refraction of light at the interface between the fluid medium and the inner wall of the bioreactor was compensated for by implementing an index-matching technique. The choice of a working fluid sharing the same index of refraction as the bioreactor material prevented the incident laser sheet from refracting.

Based on this analysis, Brown designed a model spinner flask. The bioreactor was made of acrylic with a refractive index of 1.48 – 1.49. Hendricks and Aviram (1982) had found that an

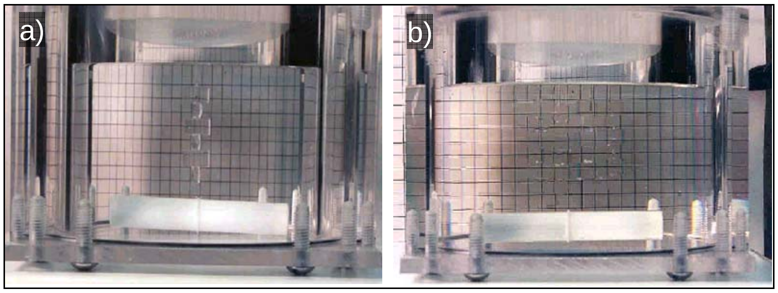

Figure 3.1: Illustration of the index-matching technique. The two pictures show the model bioreactor made of acrylic and containing one construct array. A square grid has been placed behind the bioreactor. When filled with water (a), the grid looks deformed and the edges of the construct array can be clearly identified. When filled with an index-matching solution of zinc iodide (b), deformation is attenuated and the construct array is hardly visible. This configuration allows the direct observation of the flow field by PIV.

aqueous solution of zinc iodide was suitable for flow research in this refractive-index range (**Figure 3.1**). The requirement of dynamic similarity between the model bioreactor and the prototype used by Vunjak-Novakovic et al. (1996) led to the design of a 1.6:1-scale model (**Figure 3.2**). The four equi-angularly spaced construct arrays fixed in the cap of the bioreactor can be positioned every 5 mm in the radial direction. The stirring element is driven by a two-phase stepper motor through a gear train and the power was delivered by an electronic controller, enabling smooth rotation and accurate control of the actual angular velocity. The use of a tachometer measuring the stepper motor angular speed also permits the collection of phase-locked data at specified angular orientations of the stir bar. This is required due to the unsteady nature of the flow and the need to employ ensemble averaging for the determination of turbulence quantities, as described in the previous chapter. The experimental and numerical characterizations of the flow field within the spinner flask were carried out for this model bioreactor. The instantaneous velocity and shear stress can then be quantified in the prototype bioreactor using scaling considerations, i.e.,

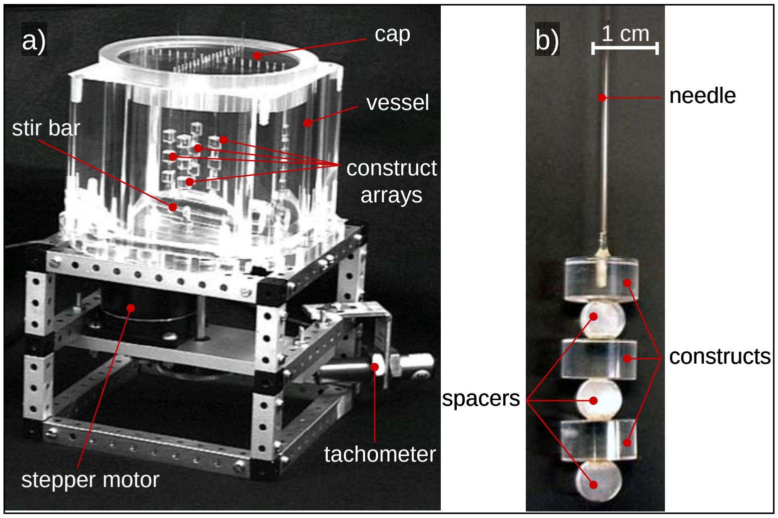

Figure 3.2: Model spinner flask made of acrylic and designed at a scale 1.6 with respect to the prototype bioreactor. The model vessel shown in picture (a) has flat external walls and is driven by a stepper motor. Picture (b) shows a model construct array also made of acrylic. Three constructs and spacers were used in this study.

$$\tilde{\mathbf{U}}_{\mathbf{ij}_p}\left(\mathbf{x},t\right)=\left(\frac{\nu_p L_m}{\nu_m L_p}\right)\tilde{\mathbf{U}}_{\mathbf{ij}_m}\left(\mathbf{x},t\right), \tag{3-1}$$

and

$$\tilde{\tau}_{ij_p}\left(\mathbf{x},t\right)=\left(\frac{\mu_p \nu_p L_m d_m}{\mu_m \nu_m L_p d_p}\right)\tilde{\tau}_{ij_m}\left(\mathbf{x},t\right), \tag{3-2}$$

where the indices $_m$ and $_p$ are relative to model and prototype quantities, respectively, $\tilde{\mathbf{U}}_{\mathbf{ij}}$ is the instantaneous-velocity vector in the plane $\left(\mathbf{e_i},\mathbf{e_j}\right)$, $\tilde{\tau}_{ij}$ is *ij*-component of the instantaneous-shear stress tensor, μ is the dynamic viscosity of the working fluid, ν is the kinematic viscosity of the working fluid, L is the length of the stir bar, and d is the diameter of a construct.

PIV setup description

The PIV setup used in this work was that implemented by Brown (1998). A double-head Nd:YAG laser (New Wave Research Minilase III) is used to generate a pulsed output beam with a wavelength of 532 nm, an energy of 50 mJ and a pulse length of 5-7 ns. The optical system designed to focus and drive the beam and to form the laser sheet consists of two mirrors and three lenses (Melles-Griot 01 LPK 015/078, 01 LPX 237/078 and 01 LCN 001/078). The thickness of the light sheet at the vessel axis is approximately 1 mm. The different components are mounted onto a TMC optical table to permit accurate positioning and alignment.

A Pulnix progressive-scan camera employing a non-interlaced charge-coupled device (CCD) array with a resolution of 768x484 pixels, a Navitar 50 mm TV lens and a 20 mm extension are used to take images of the flow. An Imagenation frame grabber (PX610) is coupled to a Pentium Pro 200 computer (96 Mb of RAM, 3 Gb of storage capacity) to capture the pictures and convert them from NTSC to 8-bit bmp format. An electronic circuit with inputs from the tachometer and the NTSC video signals and outputs to the frame grabber and laser controller is integrated with the PIV apparatus to enable phase-locked frame capturing.

The program used for the capture of the PIV pictures was essentially an upgrade of the software provided by Imagenation to operate the frame grabber. The characteristics of the video camera and frame grabber allow the capture of images at a frequency of 30 Hz. The original C code was modified by Brown in order to synchronize the capture of the PIV frames with the laser pulses, and to integrate phase-locking capability. Because the PIV technique aims at producing the instantaneous velocity field of a flow observed during the time separating the two frames of an image pair, it is critical that those two frames were captured within the smallest time interval. The repetition rate of the laser allows the time interval between two successive frames to be set at 2.7 ms. Because the video camera was capable of integrating each frame at a frequency of 30 Hz, the shortest time interval between the capture of two image pairs is 66 ms (**Figure 3.3**).

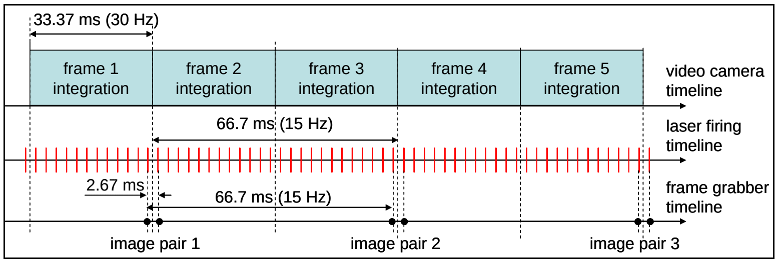

Figure 3.3: Diagram showing a comparison of the timelines for the frame integration by the video camera, the firing of the laser, and the frame acquisition by the frame grabber. The PIV system used in this work was capable of illuminating two successive frames in a time interval of 2.67 ms and storing one image pair every 66.7 ms.

Experimental protocol

Operating conditions

A solution made of 60% zinc iodide, 38% distilled water and 2% sodium bisulfite (percentages are by total mass) is used as the model culture medium (density: $\rho_m = 1901.5$ kg/m^3, kinematic viscosity: $\nu_m = 1.61$ cSt), to meet the refractive-index matching condition. Dynamic similarity of the flows within the geometrically similar model and prototype bioreactors is achieved by matching their respective Reynolds numbers as

$$\frac{L_m{}^2 \omega_m}{\nu_m} = \frac{L_p{}^2 \omega_p}{\nu_p}, \tag{3-3}$$

where the indices $_m$ and $_p$ are relative to model and prototype quantities, respectively. From the knowledge of the prototype Reynolds number of 1760, the required model stir-bar rotation rate is 32.4 rpm. The dimensions and characteristics of the model and prototype bioreactors are summarized in **Table 3-1**. The measurements of the kinematic viscosity and the angular stir-bar velocity introduce an uncertainty of 1.5% (**Appendix A**) on the desired value of the Reynolds

Table 3-1: Characteristics and operating conditions of the prototype and model bioreactors.

	prototype bioreactor	model bioreactor
bioreactor material	glass	acrylic
construct material	polyglycolic acid (PGA)	acrylic
spacer material	silicone tubing	acrylic
working fluid	cell culture medium	zinc iodide
fluid kinematic viscosity	0.971 cSt	1.61 cSt
fluid density	1.03 g/cm^3	1.90 g/cm^3
fluid volume	120 cm^3	529 cm^3
bioreactor diameter	6.50 cm	10.5 cm
free-surface height	3.8 cm	6.1 cm
stir-bar length	4.53 cm	7.24 cm
stir-bar diameter	0.787 cm	1.27 cm
construct diameter	0.693 cm	1.12 cm
construct thickness	0.377 cm	0.607 cm
spacer diameter	0.396 cm	0.638 cm
spacer thickness	0.168 cm	0.269 cm
stirring rate	50.0 rpm	32.4 rpm

number (Kline and McClintock, 1953). Therefore, the Reynolds number at which the model bioreactor is operated can be estimated as 1760 ± 27. Given this set of operating conditions, the velocity and shear-stress scaling factors given in **Equation 3-1** and **Equation 3-2**, respectively, may be calculated as

$$\tilde{\mathbf{U}}_{\mathbf{ij}_p}\left(\mathbf{x},t\right) = 0.96\ \tilde{\mathbf{U}}_{\mathbf{ij}_m}\left(\mathbf{x},t\right), \tag{3-4}$$

and

$$\tilde{\tau}_{ij_p}\left(\mathbf{x},t\right) = 0.51\ \tilde{\tau}_{ij_m}\left(\mathbf{x},t\right). \tag{3-5}$$

The four equi-angularly spaced construct arrays are positioned at 20 mm from the center of the cap of the model bioreactor. The vertical distance between the lower surface of the bottom construct and the stir-bar is fixed at 15 mm. Glass spheres (Potters Industries, 5000E) with a density of 2.54 g/cm^3 and a mean diameter of 11 μm are used as the flow-visualization tracers. When placed in the 1901.5 kg/m^3 zinc iodide solution, the dynamic conditions within the bioreactor model prevent the particles from settling out of the flow, and for visualization purposes the low sedimentation rate (13.8 μm/s for 11 μm particles, **Appendix B**) is not expected to lead to significant error in the velocity measurements.

<u>Measurement description</u>

The PIV measurements focus on the detailed characterization of the flow field in the vicinity of a construct array. Because the stir bar rotates in a clockwise direction when viewed from above, one expects a mean flow of the same sense; for the front construct array defined in **Figure 3.4**, this corresponds to flow from right-to-left. This assumption is verified by investigating a mean-velocity field obtained in the plane $(\mathbf{e}_1, \mathbf{e}_2)$ of the Cartesian reference frame

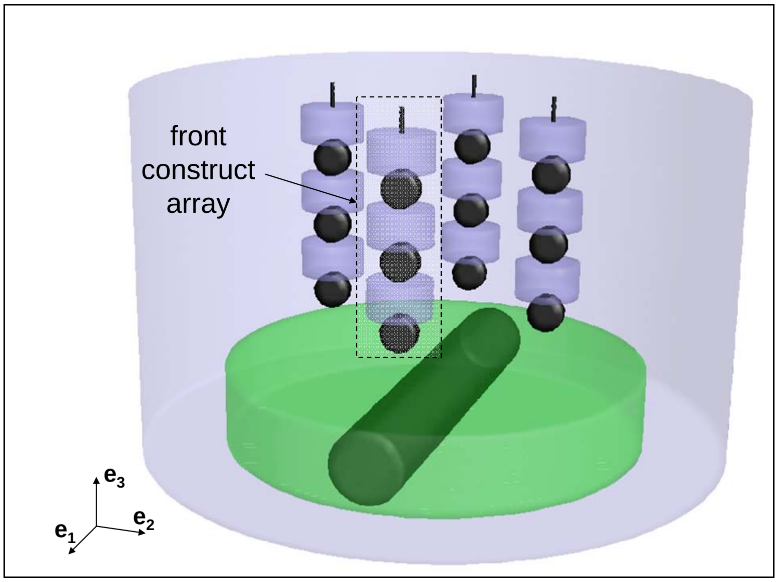

Figure 3.4: Schematic showing the position of the reference construct array in the model bioreactor and the definition of the Cartesian reference frame $(\mathbf{e}_1, \mathbf{e}_2, \mathbf{e}_3)$.

$(\mathbf{e}_1, \mathbf{e}_2, \mathbf{e}_3)$ whose origin is located at the center of the bottom of the bioreactor (see **Figure 3.4**). The flow is observed in the section located 2.8 cm from the bottom of the vessel, in the absence of constructs. For this purpose, the video camera is placed at the top of the bioreactor in a vertical position and focused on a quarter of the bioreactor, as shown in the inset of **Figure 3.5**. The instantaneous velocity field $\overline{\mathbf{U}}_{23}(\mathbf{x},t)$ depicted in **Figure 3.5** confirms that the flow generated by the impeller is essentially tangential. Based on this observation, the plane crossing the median section of the front construct array should contain the main velocity component. For this reason, the section of the flow containing the unit vectors $(\mathbf{e}_2, \mathbf{e}_3)$ is chosen as the reference plane (i.e., 0-degree cross-section). PIV measurements were also carried out in the plane passing through the axis of the needle and orthogonal to the reference cross-section described above (see **Figure 3.6**).

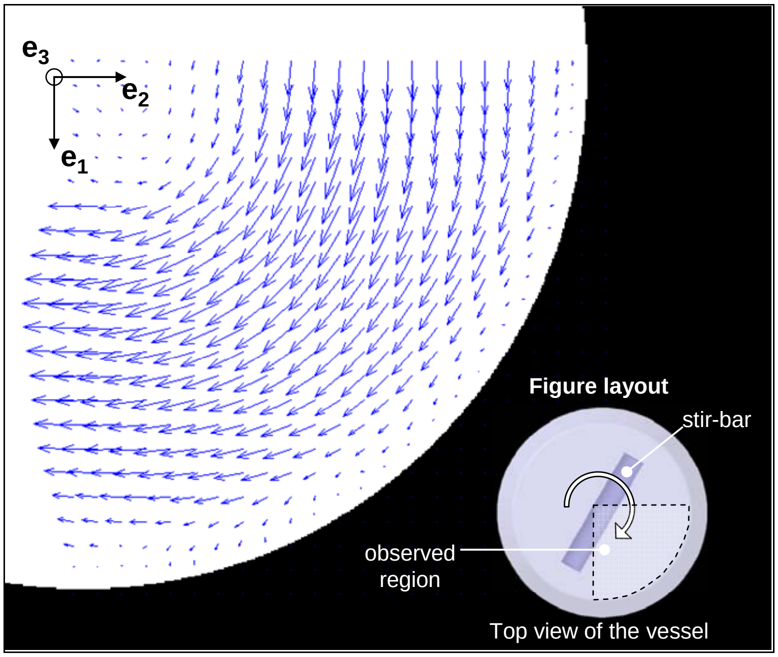

Figure 3.5: Mean velocity-vector field obtained with PIV in a quarter of the section $(\mathbf{e}_1, \mathbf{e}_2)$ of the vessel. As expected, the main flow is dominated by the tangential velocity component.

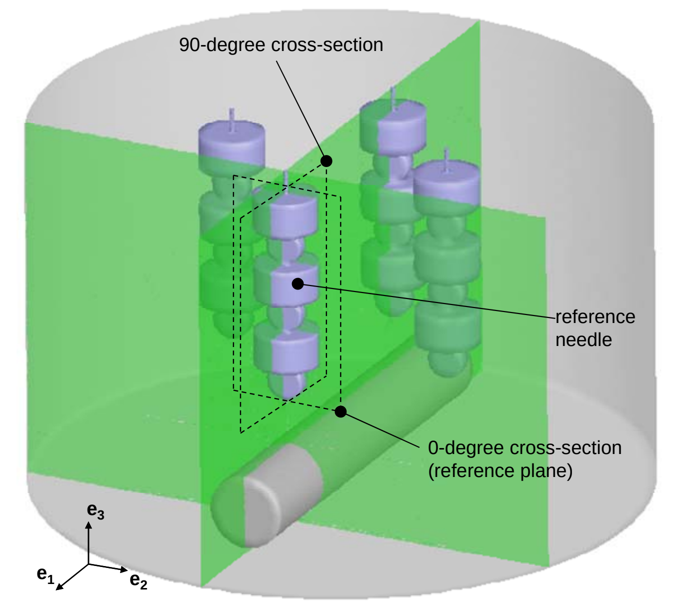

Figure 3.6: Construct cross-sections studied during the PIV experiments.

Because the flow is expected to be spatially dependent, multiple experiments were carried out for each cross-section, each focusing on a different construct (i.e., bottom, middle, or top construct). The PIV experiments resulted in the study of six flow fields (i.e., three constructs in two cross-sections). Each flow field is characterized in terms of velocity, mean-shear stress and Reynolds stress. Storage requirements limit the collection of 200 PIV realizations per field (each corresponding to one twenty-four-position stir-bar revolution), and thus 200 ensembles at each point in the field at each angular position. The capture of the first image of each series is triggered by the stir bar passing through the same fixed position.

The cross-correlation algorithm described in the previous chapter is implemented using an interrogation window of 32×32 pixels employing no shift between image pairs. The calculation of the Kolmogorov scale corresponding to the smallest eddies in the flow was used to determine a grid resolution suitable to retrieve the details of the turbulence. Based on the work of Cherry and Papoutsakis (1988), the smallest scales present in the turbulent flow produced by the spinner flask could be estimated as

$$\eta = \left(\frac{\nu^3}{\varepsilon} \right)^{\frac{1}{4}}, \tag{3-6}$$

where ν is the kinematic viscosity of the working fluid, and ε, the energy dissipation rate, can be in turn expressed as

$$\varepsilon = \frac{N_P \omega^3 L^5}{V}, \tag{3-7}$$

where ω is the angular speed of the stirrer, L is the length of the stir bar, and V is the volume of fluid in the vessel, and N_P, the power number, is a dimensionless parameter relating the resisting torque of the stirrer to its inertia force. For a turbulent flow (i.e., $\mathrm{Re} > 1000$), this number can be considered constant and equal to 0.5. The operating conditions used for the experimental description of the flow yield an eddy size of 345 μm.

In order to limit the computation time, the cross-correlation of an image pair is conducted in two different grids, one on the downstream and the other on the upstream side of each construct (**Figure 3.7**). Grids of 34 × 48 points equally spaced by 8 pixels (i.e., 261 μm, given the resolution of the frames captured by the system) were found to be a suitable compromise to collect sufficiently resolved data while limiting the CPU calculation time. This particular configuration produces an overlap of 75% between two neighboring interrogation windows. Eventually, the data collected on both sides of each construct are merged to yield a unique grid consisting of 68 × 48 points. The total computational time required to process 200 series of 24 image pairs is about 20 hours.

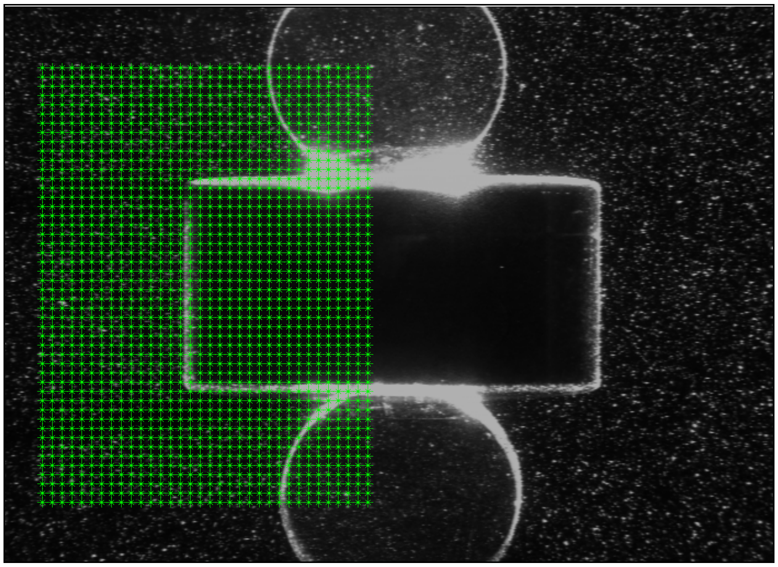

Figure 3.7: Grid points used on one side of the construct and superimposed on a typical PIV frame. Two identical grids were used for the processing of the flow field, each on one side of the construct.

Results

Mean velocity

The observation of the mean-velocity field $\overline{\mathbf{U}}_{23}(\mathbf{x},t) = \overline{U}_2(\mathbf{x},t)\mathbf{e}_2 + \overline{U}_3(\mathbf{x},t)\mathbf{e}_3$ computed by the PIV code in the upstream and downstream regions of the front construct array within the reference cross-section invites some comments. **Figure 3.8c** shows an instantaneous mean-velocity field on the upstream (right) and downstream (left) sides of the bottom construct. Upstream, the temporal variation over the course of an entire rotation period is rather small, except very close to the bar. The flow is dominated by suction created in the low-pressure wake of the stir bar, drawing fluid down and to the left. Because of inertia, the fluid cannot follow the sharp angle between the vertical wall and horizontal lower surface of the construct and the flow separates, leading to the existence of a separation bubble between the lower surface of the construct and the cylindrical spacer. In this region, the flow is nearly stagnant, compared with the main flow. In the left portion of the downstream region, the particles flow from top to bottom;

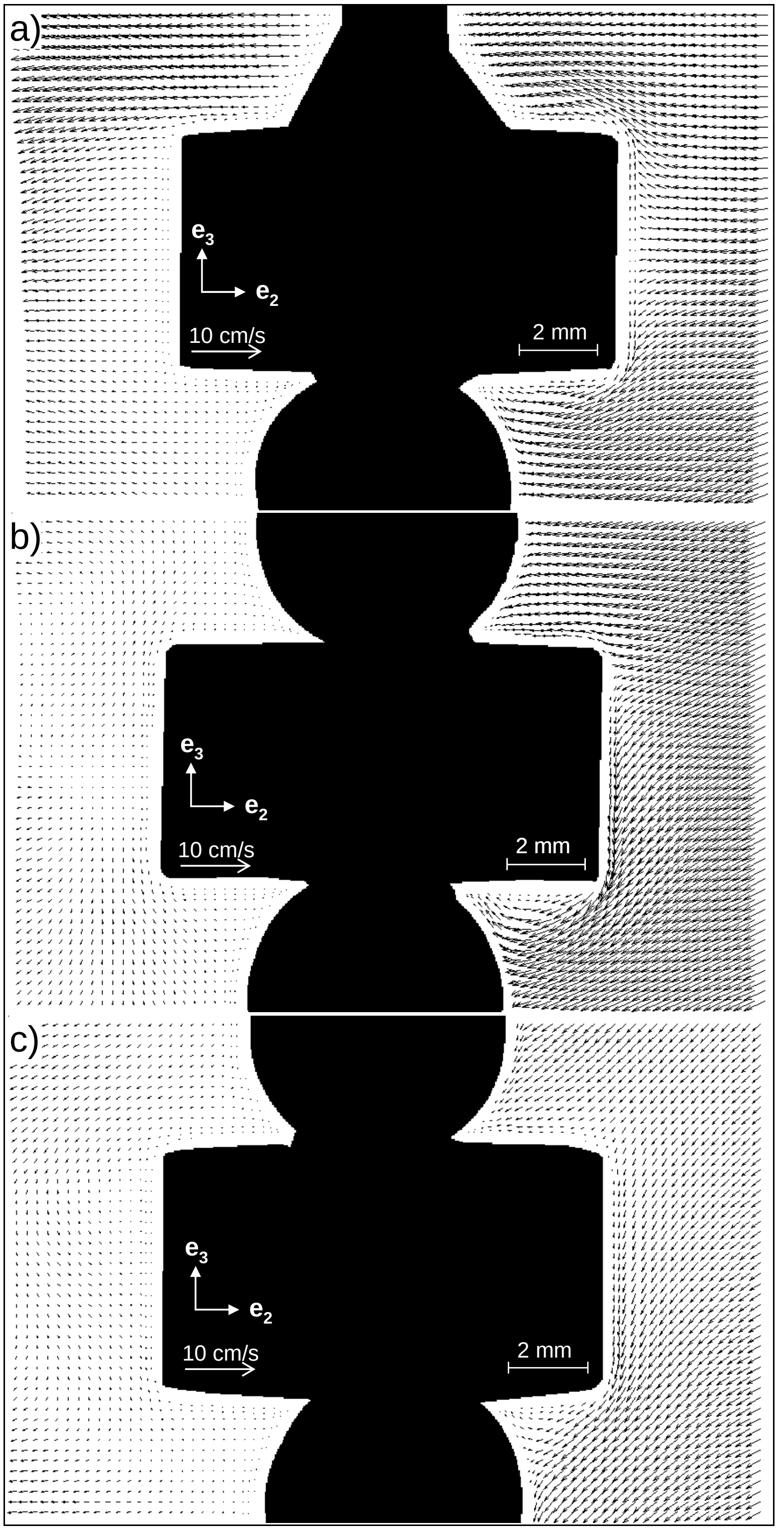

Figure 3.8: Mean-velocity fields obtained in the vicinity of the a) top, b) middle, and c) bottom constructs, in the plane $(\mathbf{e}_2, \mathbf{e}_3)$.

this flow pattern persists over the entire period of the flow, indicating the strong suction created by the stir bar. The bottom portion of the downstream region is characterized by large variations of the velocity field over the entire stir-bar revolution cycle. The mean velocity changes in both magnitude and direction, varying from strictly horizontal to strictly vertical flow. The drastic variations of the velocity in this region of the flow are obviously related to its proximity to the rotating bar. Finally, the flow separates at a point close to the lower surface of the construct for the same reasons as those described on the upstream side of the construct. The velocity components on the downstream side of the flow are relatively small compared with those in the main flow region.

The flow observed in the vicinity of the middle construct (**Figure 3.8b**) does not differ significantly from that near the bottom construct. On the upstream side of the construct the flow is oriented from the top right to the bottom left of the window. A stagnation point is located along the lateral wall, near the top surface of the construct. As compared with the flow surrounding the bottom construct, larger velocity magnitudes are observed on the upstream side. Downstream the construct (i.e., on the left of the window), the velocity magnitudes are much smaller due to the presence of the construct blocking the path of the upcoming flow.

Finally, the flow observed in the vicinity of the top construct (**Figure 3.8a**) presents significant differences with that obtained near the bottom construct. On the upstream (i.e., right) side of the construct, the flow is essentially driven by the tangential component of the velocity. At that distance from the bottom of the bioreactor, the effects of the impeller rotation are mild and do not induce significant perturbations on the vertical velocity component. The fluid flows horizontally towards the construct and the temporal velocity variations over one period are very small. A stagnation point characterized by zero fluid velocity can be observed on the lateral wall of the construct, halfway between the upper and lower surfaces. Along the edge of the construct, the fluid follows the vertical wall profile with increasing velocity as it flows away from the stagnation point. The separation bubble located near the bottom surface of the top construct is not as obvious as that identified near the bottom construct. In fact, in the vicinity of the top construct the fluid has much less momentum than near the stir bar and viscous effects dominate over inertial effects. On the downstream (i.e., left) side of the top construct, the flow follows the same horizontal trajectory as on the upstream side but with a much lower velocity magnitude. The nearly-stagnant fluid located near the vertical wall of the construct gains momentum as it moves further downstream. Finally, the flow in the upper part of the downstream region is characterized by higher horizontal velocity magnitudes than in the lower part. The cylindrical spacer located below the top construct is a bigger obstacle for the flow than the thin needle located above the construct.

The observation of the flow in the plane perpendicular to the main flow (i.e., 90-degree cross-section) permits the characterization of the mean velocity field $\overline{\mathbf{U}}_{13}(\mathbf{x},t) = \overline{U}_1(\mathbf{x},t)\mathbf{e}_1 + \overline{U}_3(\mathbf{x},t)\mathbf{e}_3$ in the vicinity of the bottom, middle and top constructs, as shown on **Figure 3.9**. The flow features observed near the bottom (**Figure 3.9c**) and middle (**Figure 3.9b**) constructs are relatively similar. In those regions, the mean velocity field $\overline{\mathbf{U}}_{13}(\mathbf{x},t)$ obtained near the center of the bioreactor (i.e., on the left of the constructs) is similar to that observed near the bioreactor wall (i.e., on the right of the constructs). On both sides of each construct, the flow is essentially oriented vertically and downward. Although the velocity scale shown in **Figure 3.9** demonstrates the existence of velocity magnitudes lower than those observed in the reference plane (i.e., 0-degree cross-section), the maximum velocity magnitude that attains 2.1 cm/s in the model bioreactor suggests the presence of a strong secondary flow created by the rotation of the impeller. The directions and magnitudes of the velocity vectors remain relatively constant over one period of the stir bar. In the wake of the two constructs (i.e., at the bottom of the figures), the fluid is nearly stagnant and progressively gains momentum as it is driven away from the construct by the surrounding flow. Finally, the fluid located above the

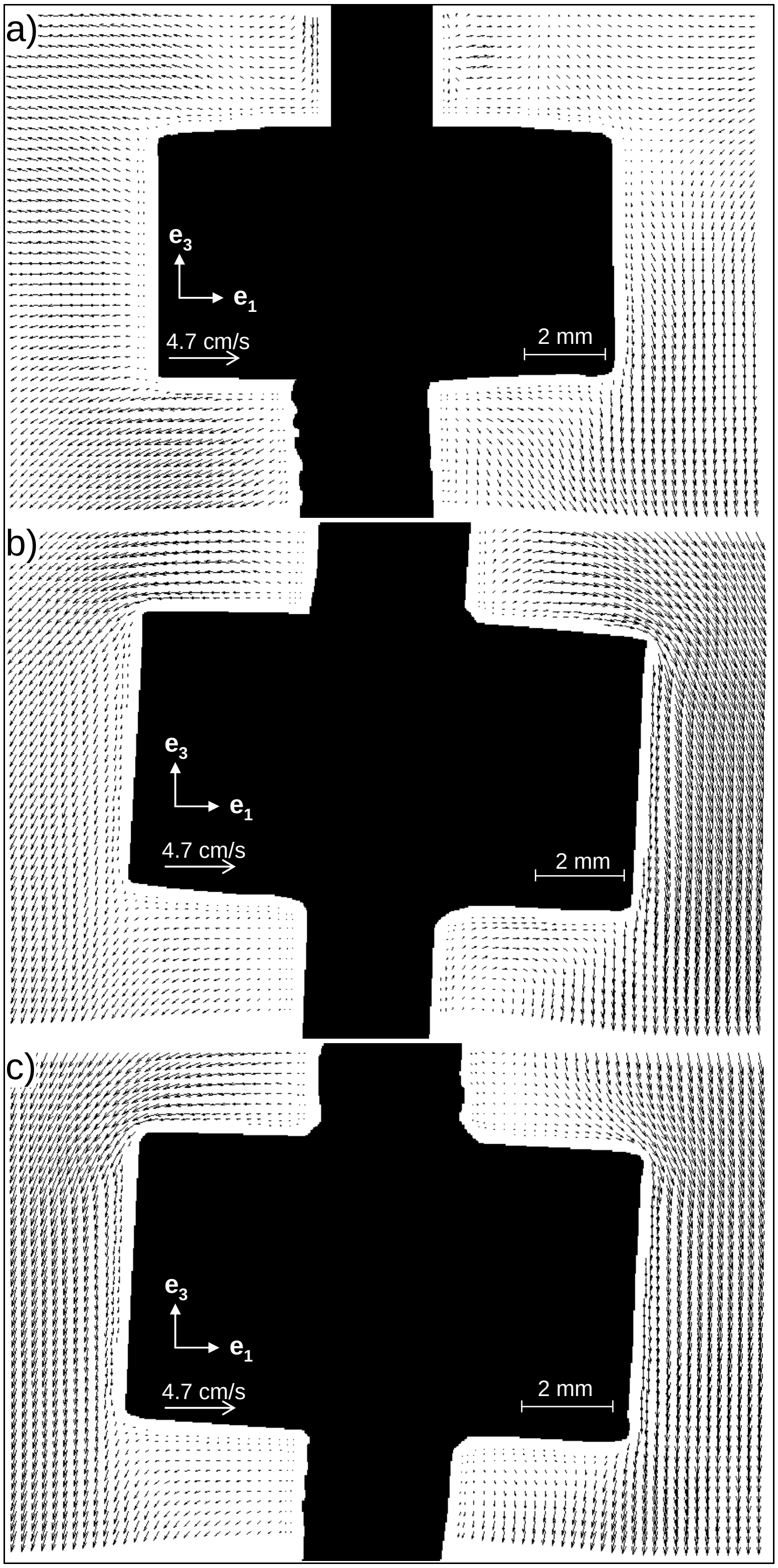

Figure 3.9: Mean-velocity fields obtained in the vicinity of the a) top, b) middle, and c) bottom constructs, in the plane $(\mathbf{e}_1, \mathbf{e}_3)$.

bottom construct is not significantly affected by the secondary flow. Because it is in the wake of the middle construct, this region is characterized by low velocity magnitudes. The same observation can be made for the flow above the middle construct.

The flow surrounding the top construct (**Figure 3.9a**) shares some features with those surrounding the bottom and middle constructs. In the region between the construct and the vessel wall (i.e., on the right of the construct), the fluid flows vertically downward as observed previously. In contrast, the mean velocity $\overline{\mathbf{U}}_{13}(\mathbf{x},t)$ on the side of the construct closer to the center of the bioreactor (i.e., on the left of the construct) is dominated by the $\bar{U}_1$-component. The magnitudes of the velocity vectors are dependent on the distance from the bottom of the vessel, with high velocities in regions close to the impeller (i.e., bottom half of the figure) and lower velocities in regions further from it (i.e., top half of the figure).

Flow periodicity

The periodicity of the flow field in the vicinity of the bottom, middle, and top constructs was characterized by the time variation of $\bar{U}_3(\mathbf{x},t)$ (i.e., vertical component of the mean velocity) over one stir-bar revolution, at 3 pairs of points as shown in **Figure 3.10**. Points 1, 2 and 3 (**Figure 3.10a**) are located in the reference plane (i.e., 0-degree cross-section), on the upstream side of the construct. Points 1', 2' and 3' (**Figure 3.10b**) in the 90-degree cross-section are located on the construct side closer to the vessel wall.

The flow exhibits π-periodicity at points close to the stir bar (points 1, 1', 2 and 2'), as expected. Near the top construct (i.e., at points 3 and 3'), the amplitude of the velocity magnitude is small and the periodicity is less obvious. This observation suggests a possible simplification of the experimental protocol for the measurement of the flow field in that region. Because the time dependence of the flow produced far from the stir bar is mild, the mean-flow quantities could be calculated by performing a standard time average. This averaging method could be implemented

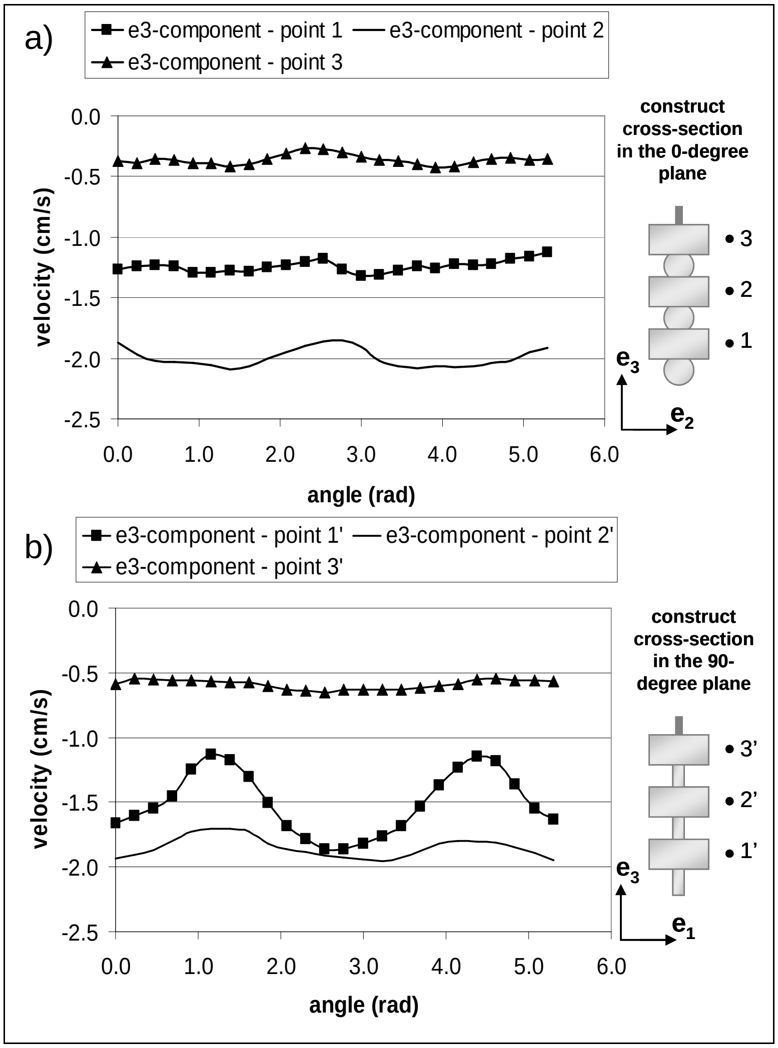

Figure 3.10: Periodicity study. Temporal variations of the x_3 – component of the mean velocity at three points located: a) on the upstream side of the construct; and b) on the side of the construct closer to the vessel wall.

by running a single PIV realization over one period of the stir bar. The study of the periodicity also suggests the spatial dependence of the flow field in the spinner flask. In both cross-sections, the change of velocity magnitude from one point to another follows the same trend: the velocity increases from point 1 (or 1') to point 2 (or 2') and then decreases from point 2 (or 2') to point 3 (or 3').

Mean-shear stress

Because the capabilities of the PIV setup used in this work were limited to the measurement of the mean-velocity field in a plane, $\overline{\mathbf{U}}_{\mathbf{ij}}(\mathbf{x},t)$, it was possible to determine only two of the six non-diagonal components of the corresponding mean-shear stress tensor, i.e., $\overline{\tau}_{ij}(\mathbf{x},t)=\mu\left(\frac{\partial \overline{U}_i}{\partial x_j}+\frac{\partial \overline{U}_j}{\partial x_i}\right)$ and its symmetric component, $\overline{\tau}_{ji}(\mathbf{x},t)$. Although the knowledge of the third component of the velocity, $\overline{U}_k$, in the direction perpendicular to the laser sheet would allow the determination of the remaining four components (i.e., $\overline{\tau}_{ik}(\mathbf{x},t)$, $\overline{\tau}_{ki}(\mathbf{x},t)$, $\overline{\tau}_{jk}(\mathbf{x},t)$, and $\overline{\tau}_{kj}(\mathbf{x},t)$), the complete mean-shear stress tensor would be known only in a plane within the flow. As observed earlier on the mean-velocity fields obtained in the vicinity of the reference needle, the flow created in the spinner flask is spatially-dependent and one can expect the shear stress to follow the same trend. Therefore, it is important to note that the determination of only two components of the mean-shear stress in the PIV plane, $\overline{\tau}_{ij}(\mathbf{x},t)$ and $\overline{\tau}_{ji}(\mathbf{x},t)$, only permits a local and incomplete characterization of the flow stresses around the constructs. A more detailed study of the flow stresses will be carried out in the next chapter using CFD tools.

The observation of the flow field in the plane $(\mathbf{e_2},\mathbf{e_3})$ (i.e., 0-degree plane) permits the calculation of the $\overline{\tau}_{23}$-component of the mean-shear stress tensor in the vicinity of the bottom, middle and top constructs. Near the bottom construct (**Figure 3.11c**), this shear stress is

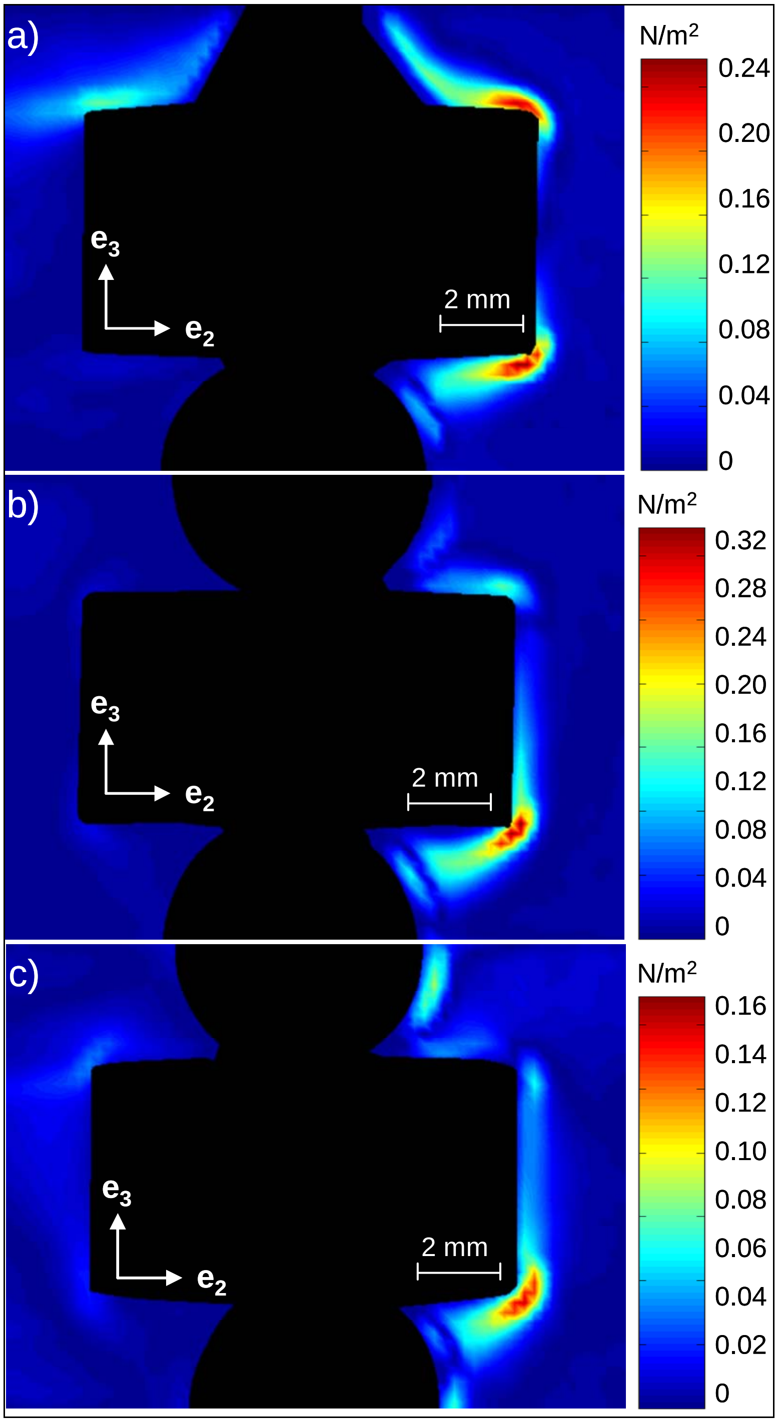

Figure 3.11: Mean-shear stress fields obtained in the vicinity of the a) top; b) middle; and c) bottom constructs, in the plane $(\mathbf{e}_2, \mathbf{e}_3)$.

concentrated on the upstream side (i.e., on the right of the construct), near the lower surface of the construct. The shear stress is dominated by the $\mu \frac{\partial \overline{U}_3}{\partial x_2}$ contribution and the existence of a viscous boundary layer on the construct surface. The shear stress attains its maximum value at the sharp corner at the intersection of the vertical wall with the lower surface of the construct, where the flow separates from it, and continues to remain high along the vertical construct wall as well as in the shear layer associated with the observed separation bubble. Quantitatively, the maximum shear stress attained in this region of the flow is 1.6 dyn/cm^2 in the model (i.e, 0.80 dyn/cm^2 in the prototype). As expected, observations of the temporal variations of the mean-shear stress field showed that this quantity was also π-periodic. On the downstream side (i.e., on the left) of the construct, the level of shear stress is negligible as compared with that obtained on the upstream side. The low magnitude and directional variations of the mean-velocity field obtained in this region over one period of the stir bar justify this observation.

Not surprisingly, the mean-shear stress field obtained in the vicinity of the middle construct (**Figure 3.11b**) is characterized by the same features because of the presence of a similar velocity field. The maximum shear stress is attained in the bottom right corner of the construct and remains relatively high along the upstream edge of the construct edge as well as in the shear layer. Velocity gradients calculated on the downstream side are milder than on the upstream side. Beside those common features, the maximum stress level attained near the wall of the middle construct (i.e., 3.1 dyn/cm^2 in the model, 1.6 dyn/cm^2 in the prototype) is twice that calculated near the bottom construct. This increase in shear stress can be explained by the presence of higher velocity magnitudes near the wall of the middle construct.

In the vicinity of the top construct (**Figure 3.11a**), the maximum value of $\overline{\tau}_{23}$ is also obtained upstream, near the sharp intersections of the lateral wall with the lower and upper surfaces of the construct. Quantitatively, the shear-stress level attained in those regions (i.e., 2.3

dyn/cm^2 in the model, 1.2 dyn/cm^2 in the prototype) is of the same order as that observed near the bottom construct. Downstream and in the bulk of the flow, the mild spatial variations of the mean-velocity field described earlier do not produce significant stresses.

The observation of the flow field in the 90-degree cross-section of the reference needle permitted the calculation of the $\overline{\tau}_{13}$-component of the mean-shear stress tensor (**Figure 3.12**). In the region surrounding the bottom construct (**Figure 3.12c**), the stress distribution is symmetric with respect to the vertical axis of the construct. The stresses obtained near the vessel wall (i.e., on the right of the construct) and near the center of the bioreactor (i.e., on the left of the construct) are qualitatively and quantitatively similar. The maximum stress level (i.e., 1.3 dyn/cm^2 in the model, 0.064 dyn/cm^2 in the prototype) observed at the intersections of the lateral wall with the top and bottom surfaces of the construct is not significantly lower than that obtained for $\overline{\tau}_{23}$ in the reference cross-section. Stress levels remain high along the lateral wall and in the boundary layer of the construct. Similar to the observations made in the reference plane, the shear stress level is relatively low further from the construct boundaries.

Near the middle construct (**Figure 3.12b**), the distribution of $\overline{\tau}_{13}$ is more asymmetric, with high levels obtained on the construct side closer to the vessel wall and relatively low levels on the side closer to the center of the bioreactor. Due to the orientation of the flow in this region, the location of the maximum shear stress corresponds to the stagnation point observed earlier between the lateral wall and the top surface of the construct. Quantitatively, the maximum value of $\overline{\tau}_{13}$ (1.6 dyn/cm^2 in the model, 0.80 dyn/cm^2 in the prototype) is similar to that observed near the bottom construct. The construct side closer to the center of the vessel is characterized by milder stresses except at the intersection between the lateral wall and the top surface of the construct.

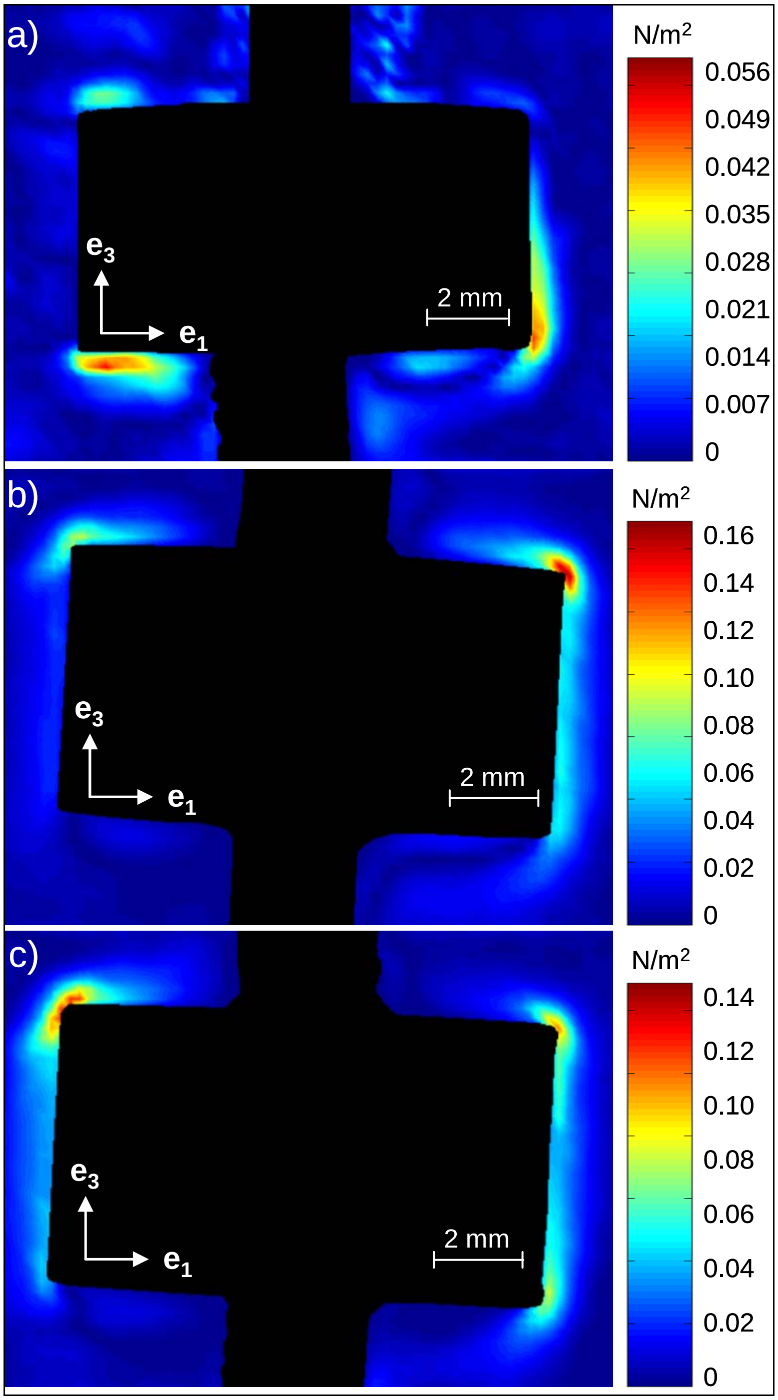

Figure 3.12: Mean-shear stress fields obtained in the vicinity of the a) top; b) middle; and c) bottom constructs, in the plane $(\mathbf{e}_1, \mathbf{e}_3)$.

Finally, the maximum value of $\overline{\tau}_{13}$ in the region surrounding the top construct (**Figure 3.12a**) occurs near the intersection of the bottom surface with the lateral wall of the construct but the maximum stress (0.56 dyn/cm^2 in the model, 0.29 dyn/cm^2 in the prototype) is only half that calculated in the vicinity of the bottom construct. A summary of the maximum mean-shear stresses observed in the cross-sections of each construct is reported in **Table 3-2** where the values corresponding to the model have also been scaled to the prototype.

Table 3-2: Summary of the maximum mean-shear stresses found in the vicinity of the bottom, middle and top constructs, for the PIV experiments conducted in the 0-degree and 90-degree cross-sections of the reference needle.

	$\overline{\tau}_{23}$ (0-degree plane)		$\overline{\tau}_{13}$ (90-degree plane)	
	model	prototype	model	prototype
top construct	2.3 dyn/cm^2	1.2 dyn/cm^2	0.56 dyn/cm^2	0.29 dyn/cm^2
middle construct	**3.1 dyn/cm^2**	1.6 dyn/cm^2	**1.6 dyn/cm^2**	0.80 dyn/cm^2
bottom construct	1.6 dyn/cm^2	0.83 dyn/cm^2	1.3 dyn/cm^2	0.64 dyn/cm^2

Turbulence correlation coefficient

The correlation between the fluctuating-velocity components $u_i(\mathbf{x},t)$ and $u_j(\mathbf{x},t)$ can be characterized by the turbulence correlation coefficient ρ_{ij} (Tennekes and Lumley, 1972) defined as

$$\rho_{ij}(\mathbf{x},t)=\frac{\overline{u_i(\mathbf{x},t)u_j(\mathbf{x},t)}}{\left[\overline{u_i^2}(x,t)\right]^{\frac{1}{2}}\left[\overline{u_j^2}(x,t)\right]^{\frac{1}{2}}}. \tag{3-8}$$

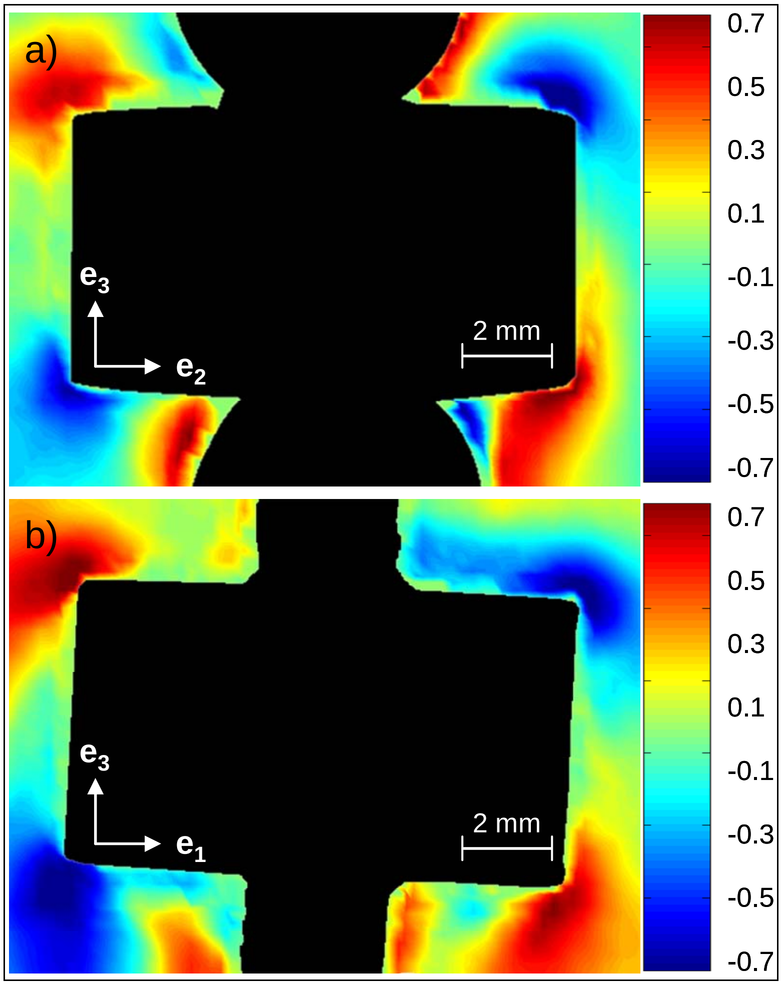

Figure 3.13: Snapshot of the turbulence correlation coefficient calculated at one instant of time in the vicinity of the bottom construct in a) the plane $(\mathbf{e}_2,\mathbf{e}_3)$; and b) the plane $(\mathbf{e}_1,\mathbf{e}_3)$.

The turbulence correlation coefficient was calculated in the vicinity of the bottom construct, in the plane containing the main flow (i.e., plane $(\mathbf{e}_2,\mathbf{e}_3)$) and in the plane perpendicular to the main flow (i.e., plane $(\mathbf{e}_1,\mathbf{e}_3)$). In the former, the coefficient ρ_{23} correlates the velocity components u_2 and u_3. In the latter, the coefficient ρ_{13} correlates the velocity components u_1 and u_3. **Figure 3.13** is a snapshot of the coefficient distribution obtained in the plane $(\mathbf{e}_2,\mathbf{e}_3)$ (**Figure 3.13a**) and in the plane $(\mathbf{e}_1,\mathbf{e}_3)$ (**Figure 3.13b**). The results suggest a correlation coefficient ranging from -0.7 to 0.7, depending on the location in the observed region. Although a coefficient of ± 0.7 indicates a strong correlation between the two velocity components, it is not characteristic of the entire flow field since it applies only to very small regions. The results obtained at different times over an entire period of the stir bar are very similar and invite the same comments.

Reynolds stress

The Reynolds stress is an apparent stress due to nonlinear interactions of the turbulent fluctuations that characterizes the impact of the turbulence on the mean flow (Tennekes and Lumley, 1972). For the same reasons as those explained for the calculation of the mean-shear stresses, the components of the Reynolds stress tensor calculable from the PIV data collected in the 0-degree and 90-degree planes were $\tau_{23}\left(\mathbf{x},t\right)$ and $\tau_{13}\left(\mathbf{x},t\right)$, respectively. **Figure 3.14** shows the magnitude of $\tau_{23}\left(\mathbf{x},t\right)$ at an instant of time, in the vicinity of the bottom, middle and top constructs of the reference needle. In the upstream region of the bottom construct (**Figure 3.14c**), it is seen that the Reynolds stresses are largest in the shear layer that separates from the sharp edge of the construct, as might be expected. In the vicinity of the construct surfaces, the Reynolds stress is very small, due to the inhibition of turbulent fluctuations by the solid walls. Although the largest turbulent stresses can be observed in the shear layer, the maximum Reynolds stress obtained over one period is approximately 1.0 dyn/cm^2 in the model (0.51 dyn/cm^2 in the prototype). This value is only 61% that of the maximum mean shear-stress in this region of the flow. Similar observations can be made on the Reynolds-stress fields in the vicinity of the middle (**Figure 3.14b**) and top (**Figure 3.14a**) constructs, suggesting the dominance of the mean shear-stress over the Reynolds stress near the three tissue constructs, at each instant of time, for the conditions at which these experiments were performed. This observation is in agreement with the typical structure of turbulent flows in the viscous sublayer in a thin region near a wall

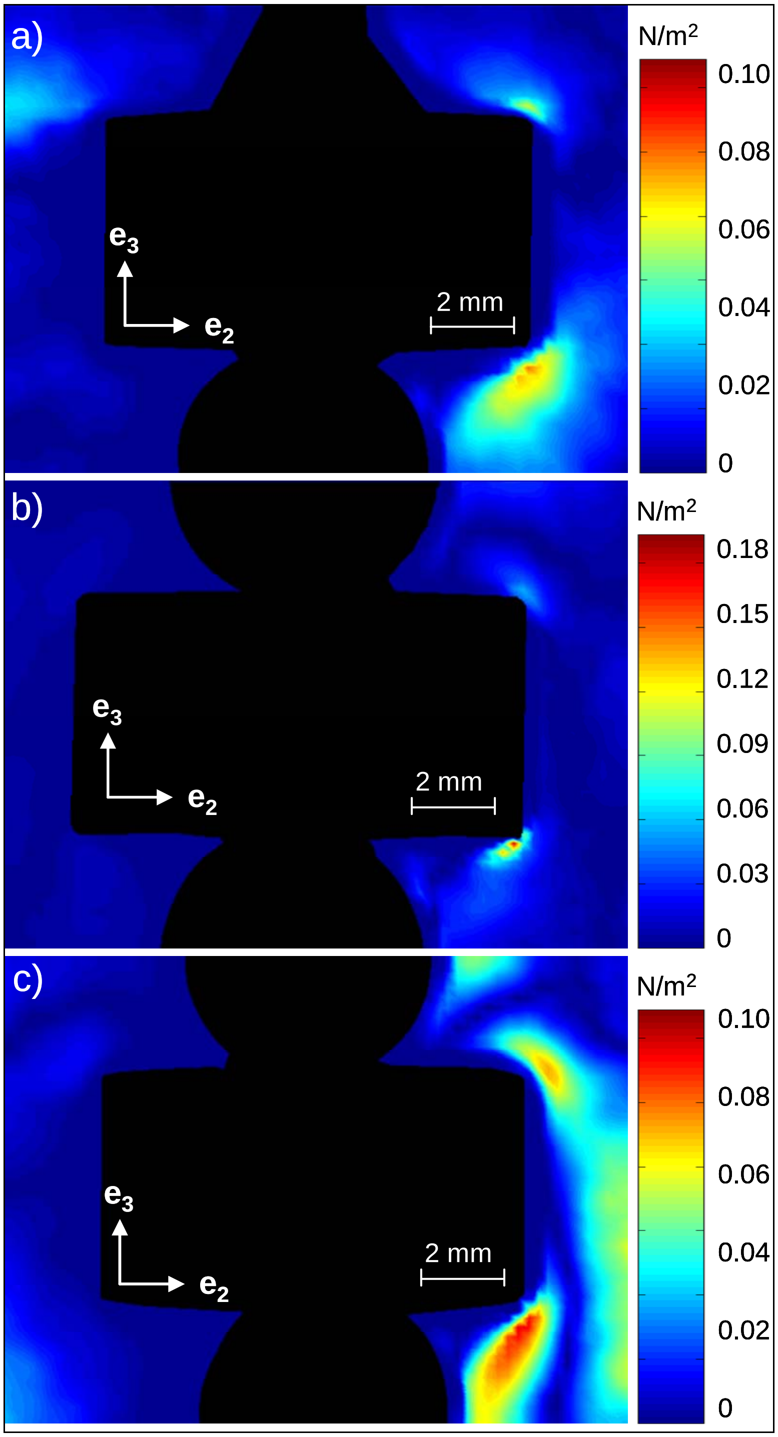

Figure 3.14: Reynolds stress fields obtained in the vicinity of the a) top; b) middle; and c) bottom constructs, in the plane $(\mathbf{e}_2, \mathbf{e}_3)$.

characterized by the dominance of the laminar shear-stress over the turbulent shear-stress. The maximum Reynolds stress observed in the 0-degree cross-section of the reference needle is 1.8 dyn/cm^2 for the model (0.92 dyn/cm^2 for the prototype) and is localized near the middle construct (**Figure 3.14b**). On the downstream flow region of each construct, the Reynolds stress remains low over the entire cycle of the impeller. The maximum value of the Reynolds stress observed in this region of the flow is approximately 0.50 dyn/cm^2 for the model (0.26 dyn/cm^2 for the prototype) and is localized near the middle construct. This level has to be compared with the maximum value of 1.8 dyn/cm^2 found in the upstream region of the same construct. The net decrease of Reynolds stress from the upstream to the downstream side of the scaffold can be explained by the presence of the construct, constituting an obstacle in the path of the main flow.

The PIV data collected in the 90-degree cross-section of the reference needle permitted the calculation of the τ_{13}-component of the Reynolds stress tensor. The magnitude of this component in the vicinity of the bottom, middle and top constructs are illustrated in **Figure 3.15c**, **Figure 3.15b**, and **Figure 3.15a**, respectively. For the same reasons discussed above, this component of the Reynolds stress has very low levels along solid walls and is concentrated near the intersections of the lateral wall of the constructs with the top and bottom surfaces. This observation along with those made in the plane $(\mathbf{e_2},\mathbf{e_3})$ permit one to conclude that the influence of the turbulence on the mean flow is negligible near the constructs. Although the Reynolds stress is necessarily zero at the construct surface, it does play a role in the redistribution of momentum, impacting mean-flow velocity gradients. As already observed on the fields relative to the $\overline{\tau}_{13}$-component of the mean-shear stress, the corresponding turbulent stress is symmetrically distributed with respect to the construct axis. As compared with the Reynolds stress obtained in the 0-degree cross-section of the needle, those obtained in the orthogonal plane are even smaller, with a maximum of 0.80 dyn/cm^2 (0.41 dyn/cm^2 in the prototype) attained in the vicinity of the

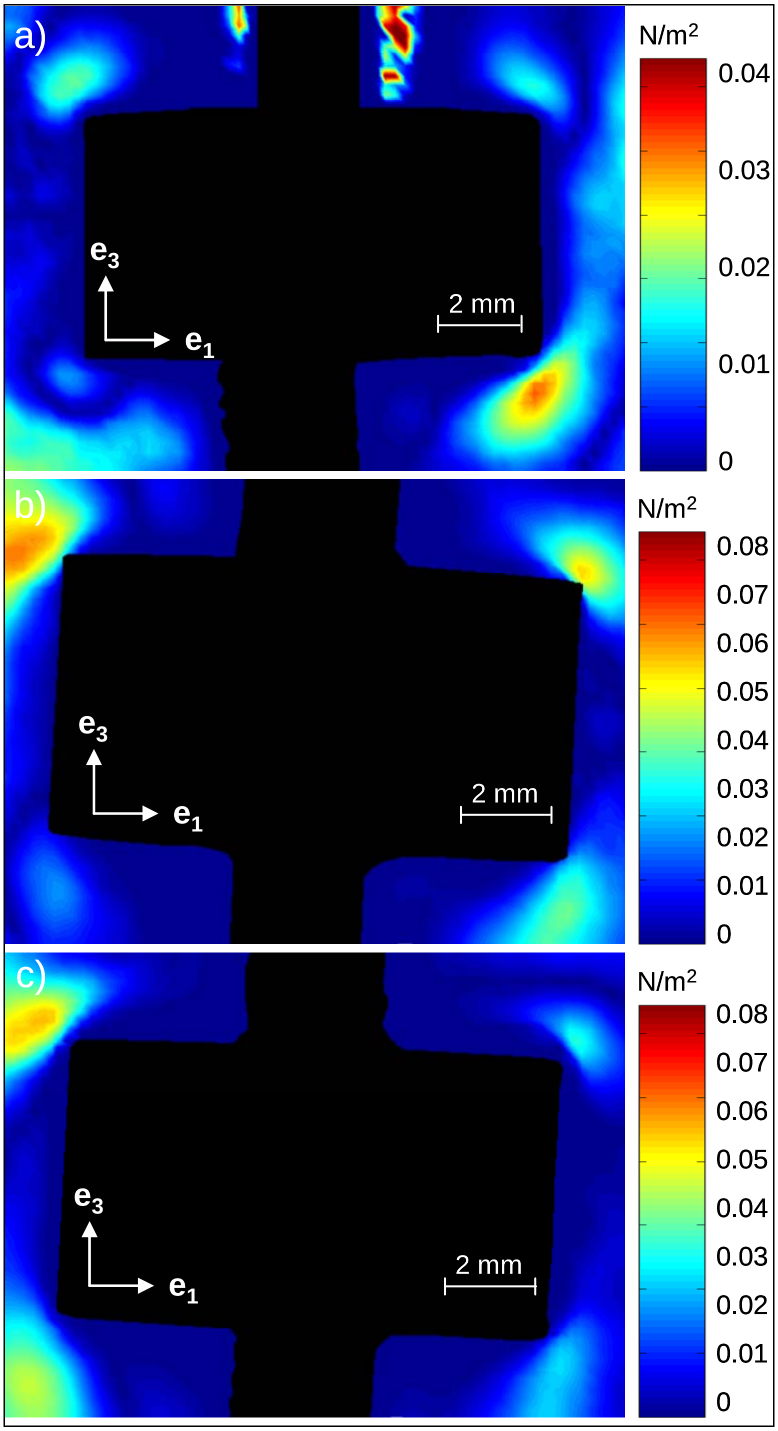

Figure 3.15: Reynolds stress fields obtained in the vicinity of the a) top; b) middle; and c) bottom constructs, in the plane $(\mathbf{e}_1, \mathbf{e}_3)$.

middle construct. **Table 3-3** proposes a summary of the maximum Reynolds stresses observed in the two cross-sections of each construct, for the model and the prototype.

Table 3-3: Summary of the maximum Reynolds stresses found in the vicinity of the bottom, middle and top constructs, for the PIV experiments conducted in the 0-degree and 90-degree cross-sections of the reference needle.

	τ_{23} (0-degree plane)		τ_{13} (90-degree plane)	
	model	prototype	model	prototype
top construct	1.0 dyn/cm^2	0.51 dyn/cm^2	0.40 dyn/cm^2	0.20 dyn/cm^2
middle construct	**1.8 dyn/cm^2**	0.92 dyn/cm^2	**0.80 dyn/cm^2**	0.41 dyn/cm^2
bottom construct	1.0 dyn/cm^2	0.51 dyn/cm^2	0.80 dyn/cm^2	0.41 dyn/cm^2

Measurement validation

In an effort to strengthen the conclusions drawn from this experimental analysis, the validity of the velocity measurements performed by the PIV setup had to be checked. The method adopted for this purpose consisted of verifying the requirement of mass conversation at one point in the flow. The applicability of the continuity equation throughout a specific flow guarantees that the mass of fluid entering a fixed control volume either leaves that volume or accumulates within it. The general continuity equation for a Newtonian fluid can be written in Cartesian coordinates as:

$$\frac{\partial\left[\rho(\mathbf{x},t)\right]}{\partial t}+\frac{\partial\left[\rho(\mathbf{x},t)U_i(\mathbf{x},t)\right]}{\partial x_i}=0, \tag{3-9}$$

where $\rho(\mathbf{x},t)$ is the density of the fluid, $U_i(\mathbf{x},t)$ is the x_i-component of the instantaneous velocity, and $\frac{\partial}{\partial t}$ and $\frac{\partial}{\partial x_i}$ denote the temporal and spatial derivatives, respectively. Averaging this equation and assuming an incompressible flow, the continuity equation can be simplified as:

$$\frac{\partial\left[\bar{U}_i(\mathbf{x},t)\right]}{\partial x_i}=0\,. \tag{3-10}$$

where $\bar{U}_i(\mathbf{x},t)$ is the x_i-component of the mean velocity. For an incompressible flow to be physically possible in terms of mass conservation, this equation must hold throughout the flow field.

The continuity equation was tested at the point REF1 of coordinates $(x_1,x_2,x_3)=(2,\ 0.77,\ 4.36)$ located at 0.21 cm on the upstream side of the middle construct threaded on the reference needle. This validation required the three components of the mean-velocity to be determined at that particular point. Since the setup implemented in the lab only allowed two-dimensional measurements of the flow (i.e., measurements of the velocity components contained in a plane), two experiments had to be carried out using two orthogonal laser sheets intersecting at the point of interest. **Figure 3.16** shows the laser-sheet configuration relative to each experiment. The experiments already performed in the plane $(\mathbf{e}_2,\mathbf{e}_3)$ passing through the axis of the reference needle allowed the extraction of the velocity components $\bar{U}_2$ and $\bar{U}_3$ at the reference point. The illumination of the plane $(\mathbf{e}_1,\mathbf{e}_3)$ passing through the point of investigation permitted the measurement of the third component $\bar{U}_1$. Because both experiments were run consecutively with slight differences in fluid properties due mainly to temperature variations, it was important to verify that the flow conditions were identical. For this purpose, the

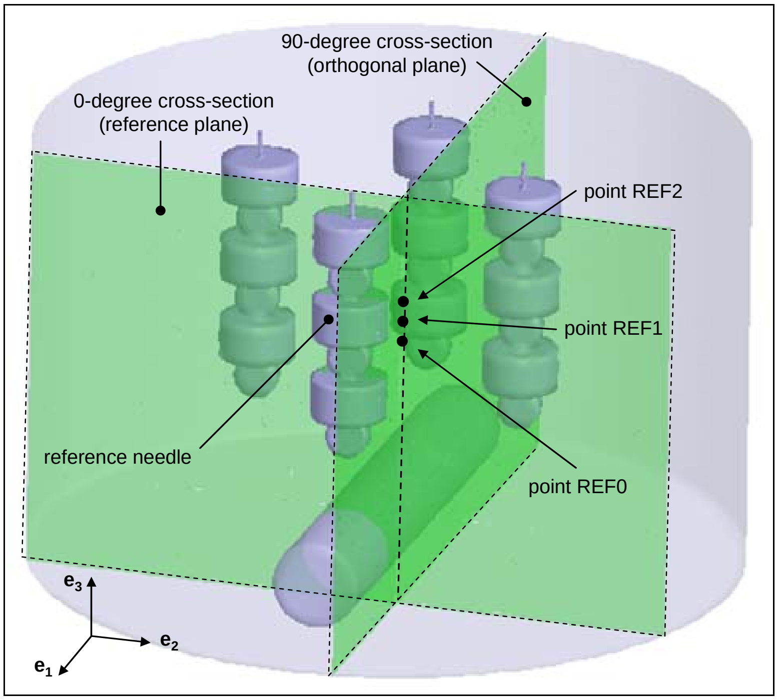

Figure 3.16: Flow-continuity study. The three mean-velocity components necessary for the calculation of the normalized continuity value were measured at point REF1 located 2 mm from the wall of the middle construct threaded on the reference needle by carrying out PIV experiments in two orthogonal planes. Points REF0, REF1 and REF2 aligned along the intersection between the two planes were used to compare $\bar{U}_3(\mathbf{x},t)$ measured in each plane.

temporal variations of $\bar{U}_3(\mathbf{x},t)$ were compared between both realizations at three points (i.e., REF0, REF1 and REF2) located along the intersection between the two planes (see **Figure 3.16**). Points REF0 and REF2 were located 0.3-mm below and above point REF1, respectively. As shown in **Figure 3.17**, the signals obtained in both experiments at each point showed nearly similar phases and intensities. From the knowledge of $\bar{U}_1(\mathbf{x},t)$, $\bar{U}_2(\mathbf{x},t)$ and $\bar{U}_3(\mathbf{x},t)$ at three points collinear to $\mathbf{e_1}$, $\mathbf{e_2}$ and $\mathbf{e_3}$, respectively, one of which located in front of the reference point REF1 and the other behind, permitted the calculation of $\frac{\partial \bar{U}_1}{\partial x_1}$, $\frac{\partial \bar{U}_2}{\partial x_2}$, and $\frac{\partial \bar{U}_3}{\partial x_3}$,

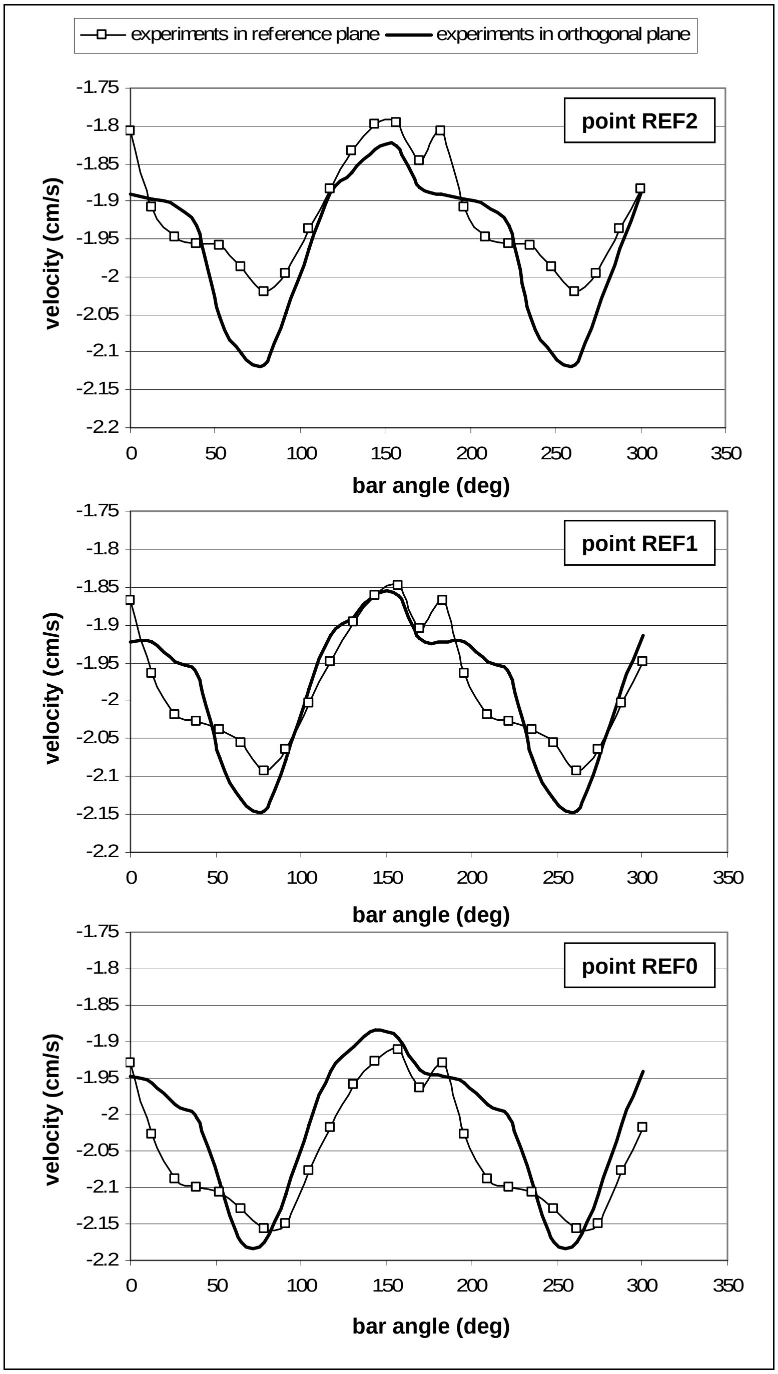

Figure 3.17: Time variations of $\overline{U}_3(\mathbf{x},t)$ measured in the reference and orthogonal planes, at points REF0, REF1 and REF2. Although the experiments were conducted consecutively in two different planes, the flow conditions were almost identical.

respectively, using second-order accurate centered finite differences. The continuity value C defined as

$$C = \left| \frac{\partial \bar{U}_1}{\partial x_1} + \frac{\partial \bar{U}_2}{\partial x_2} + \frac{\partial \bar{U}_3}{\partial x_3} \right| \tag{3-11}$$

was then calculated at the reference point REF1 over one period of the stir bar. Normalizing this value by a quantity reflecting the magnitude of the velocity derivatives in each direction yielded

$$\|C\| = \frac{\left| \frac{\partial \bar{U}_1}{\partial x_1} + \frac{\partial \bar{U}_2}{\partial x_2} + \frac{\partial \bar{U}_3}{\partial x_3} \right|}{\left[\left(\frac{\partial \bar{U}_1}{\partial x_1} \right)^2 + \left(\frac{\partial \bar{U}_2}{\partial x_2} \right)^2 + \left(\frac{\partial \bar{U}_3}{\partial x_3} \right)^2 \right]^{\frac{1}{2}}} . \tag{3-12}$$

The results shown in **Figure 3.18** suggest a maximum and minimum value of 0.325 and 0.128, respectively. The mean value over half a stir bar rotation was estimated at 0.230. Although the reported values of $\|C\|$ do not match closely the theoretical value of 0, they do not diverge significantly from it. One of the reasons for this result is the difficulty to produce two orthogonal laser sheets intersecting at the exact location where the continuity value is to be calculated. Although the close match obtained between the measurements of the $x_3 -$component of the mean velocity in the two planes at three different points demonstrates that this issue could be fairly overcome, other difficulties impact the production of a good normalized continuity value. First, the calculation of spatial derivatives of a noisy signal such as a velocity component in a turbulent flow induces some errors. Although the flow field was ensemble-averaged over 200 PIV realizations, the resulting mean-velocity history at one fixed point over one period still exhibited

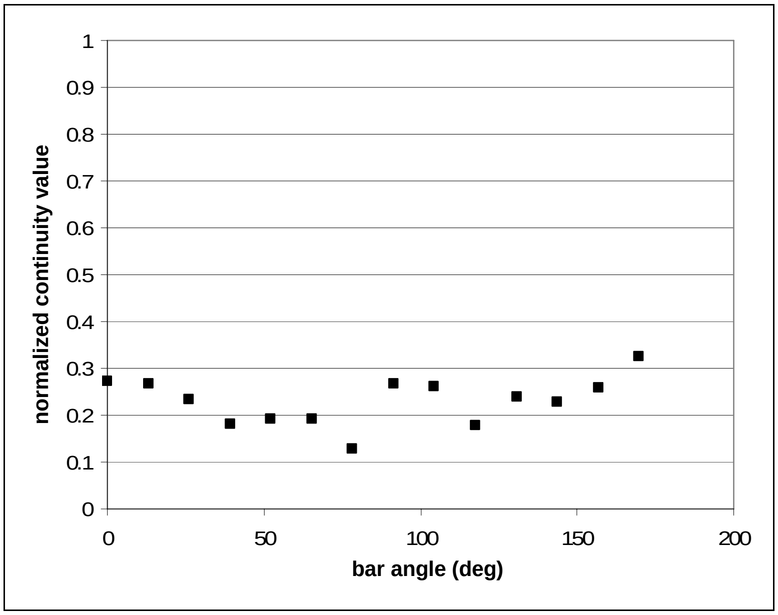

Figure 3.18: Normalized continuity value calculated at point REF1 over one period of the stir bar. The mean normalized continuity value was found to be 0.230 over one period.

randomness and noise due to its turbulent nature (see **Figure 3.17**). In addition, the calculation of the continuity value was made at a point located at 2 mm from the wall of the middle construct. The proximity of a solid wall suggests the presence of high velocity gradients which might be difficult to capture accurately using PIV. Given all those difficulties, the results obtained in this section were considered sufficient to serve as a validation for the PIV measurements.

Concluding remarks

The investigation of the flow field produced by the spinner flask in the vicinity of a model construct array by particle-image velocimetry permitted the characterization of the mean and turbulent flow quantities. The tools developed for the analysis of the resulting experimental data permitted the assessment of the mean velocity, mean-shear stress, and Reynolds stress environments. The reliability of the velocity estimates calculated by cross-correlation was addressed by testing the validity of the continuity equation at a reference point located near the construct wall. The results obtained by this analysis in a region characterized by large velocity gradients raises some questions on the capability of the PIV setup to measure quantities such as mean-shear stresses. Because this work focuses on the dependence of tissue growth on the shear-stress level produced on the construct surface, the measurement accuracy of this flow quantity is critical. However, although the description of the flow characteristics is relevant for tissue growth, it is strongly dependent on the operating conditions and on the geometric layout chosen to conduct the measurement. Therefore, in order to extend our knowledge of the flow field in this particular bioreactor, more systematic methods such as computational fluid dynamics had to be employed. For this reason, the experimental protocol described in this section was aimed primarily at producing accurate velocity measurements permitting the design and validation of this computational model. The experimental characterization of the mean-shear stress environment was expected to be more qualitative.

CHAPTER 4

COMPUTATIONAL FLOW MODEL DEVELOPMENT

FLUENT finite-difference software

The numerical fluid-flow model was constructed for the spinner flask with the commercial CFD package, FLUENT. This computer program has been designed for modeling fluid flow in complex geometries. FLUENT offers several mesh options. Tetrahedral, hexahedral, pyramid, wedge elements or any combination of those can be used to discretize complex three-dimensional flow domains. The software is capable of refining the meshed region in a portion of the flow domain defined by the user. FLUENT automatically updates the mesh structure in that region and at the interface between the coarse and the refined mesh. In addition, the program can handle dynamic geometries. Translating and deforming meshes can be implemented and solved by updating their structures at each time step. FLUENT is based on a code written in the C computer language that offers the users the possibility to create custom functions including basic quantities computed by the solver. The graphical-user interface and the Windows™-like menu system add ease of use and conviviality to the software.

The software package consists of a solver, a preprocessor for geometry modeling and mesh generation, and an additional preprocessor that can generate volume meshes from existing boundary meshes. The overall steps involved in the solving process are the preprocessing, the calculation of the results and the post-processing. During the preprocessing step, the model geometry and grid are generated and the grid is checked and validated. The preliminary calculation step consists of the definition of the basic equations to be solved, the specification of the material properties, the definition of the boundary conditions and the initialization of the flow field. Once all the information has been entered, the calculation can be performed. This step ends with the production of the flow results. In the post-processing step, the data and images are reorganized and analyzed.

Three-dimensional geometry and mesh generation

The bioreactor geometry was built on the design proposed by Osorio (2001). The original model was expanded and was added several features aiming at improving its capabilities and accuracy. The spinner-flask bioreactor was modeled with GAMBIT, a mesh generator software. The entire geometry was divided into four distinct zones: the cylindrical spacers threaded onto the four equi-angularly spaced needles modeled as solid entities, the constructs modeled first as solid and later as porous media, a sliding zone enclosing the rotating stir bar, and finally the fluid zone, i.e., the entire vessel volume from which the three previous zones have been subtracted.

As pointed out by Osorio, one of the challenges in this geometry was the design of the rotating impeller. The presence of this moving boundary was accounted for by creating a cylindrical zone centered on the stir bar and rotating at the same angular speed. Another issue arose from the sharp connection between a construct and its neighboring spacer(s). In the actual bioreactor, the spacers were tangential to the constructs, creating a linear contact between those two solids. This narrow intersection could be a problem when meshing the entire vessel volume. A rectangular contact zone was created to overcome this issue (**Figure 4.1**). The entire geometry and the different elements described above can be appreciated in **Figure 4.2**.

The choice of an acceptable mesh constituted another challenge in the design of the geometry. In fact, the spinner flask contained elements of different scales (e.g., the diameter of the needles was 0.81 mm whereas that of the constructs was 1.12 cm and that of the vessel was 10.5 cm). The presence of a wide range of dimensions was expected to affect the quality of the mesh to be generated. Although GAMBIT offers a variety of meshing elements, the TGRID option was the only one to yield an acceptable mesh in terms of cell equi-angle skew and aspect

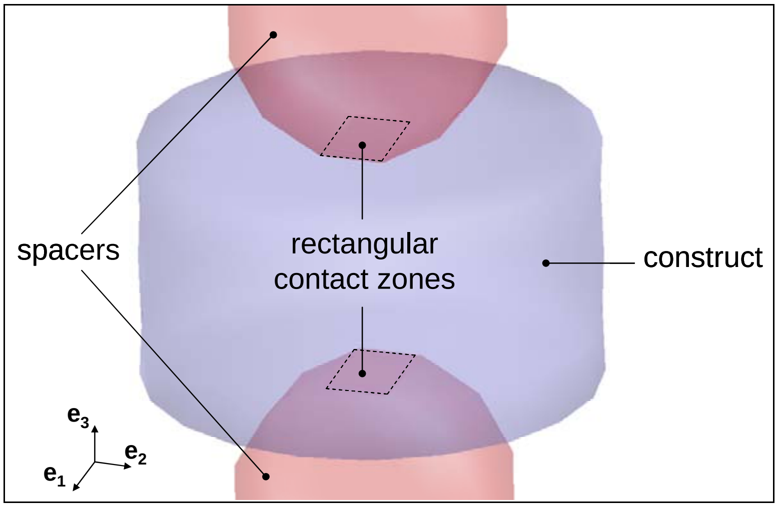

Figure 4.1: Detail of the contact zone between a construct and its neighboring spacers.

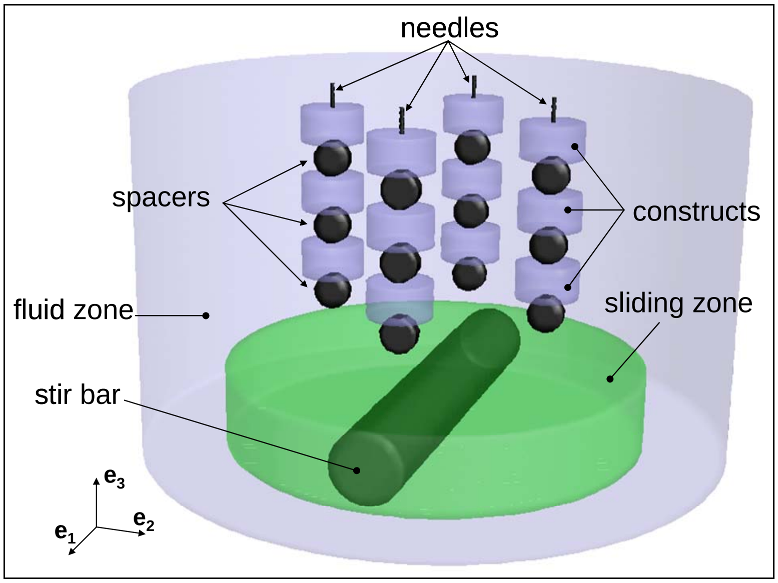

Figure 4.2: Three-dimensional geometry of the spinner flask constructed with GAMBIT. At time $t = 0$, the stir bar is aligned in the $\mathbf{e}_1$ – direction.

ratio. This meshing algorithm primarily uses tetrahedral elements to mesh volumes, and pyramidal or hexahedral elements where needed. The available computational resources (Pentium 4, 2.2 GHz, 2Gb of RAM, 111 Gb of storage capacity) allowed the implementation of a relatively fine mesh size. A coarse mesh with an interval size of 0.18 cm was generated in the two fluid regions of the vessel (i.e., the sliding zone and the fluid zone). The volume occupied by the constructs was treated with a thinner mesh size of 0.10 cm in order to provide the computed results at that critical location with more resolution. The coarse mesh featured 517,431 cells, 1,135,655 faces and 110,535 nodes.

The default measure of mesh quality in GAMBIT is expressed by the maximum equiangle skew (i.e. a normalized measure of skewness) defined as

$$\chi = \max\left[\frac{\theta_{\max} - \theta_e}{180}, \frac{\theta_e - \theta_{\min}}{\theta_e}\right], \qquad \text{(4-1)}$$

where $\theta_{\max}$ is the largest angle in the cell, $\theta_{\min}$ is the smallest angle, and θ_e is the angle of an equiangular cell (i.e., 60° for tetrahedral elements, 90° for a hexahedral elements). The value obtained in the coarse mesh was 0.93, with 82.56% of the elements having a skewness ranging between 0.2 and 0.5 (**Table 4-1**). This value was below the critical value of 0.98 above which numerical convergence was likely to fail. The maximum cell volume detected by GAMBIT was 4 mm^3. Finally, the aspect ratio of the cells was shown to range between 1 and 7.

The free surface of the liquid contained within the vessel was modeled as undeformed, satisfying the condition of zero shear stress. On the surfaces of the cylindrical spacers, the needles, the vessel and the stir bar were applied no-slip conditions. The same condition was imposed on the surface of the constructs when they were modeled as solids.

Table 4-1: Mesh-quality report produced by GAMBIT for equiangle skew.

From value	To value	Count in range	% of total count
0	0.1	15497	2.99
0.1	0.2	25897	5.00
0.2	0.3	100764	19.47
0.3	0.4	215528	41.65
0.4	0.5	110946	21.44
0.5	0.6	32885	6.36
0.6	0.7	12378	2.39
0.7	0.8	3504	0.68
0.8	0.9	28	0.01
0.9	1.0	4	0.00

Turbulence modeling

The results obtained by Osorio (2001) demonstrated that a simple turbulent viscosity model was capable of fairly simulating the turbulent flow generated in the spinner flask. This type of model is typically constructed on the Boussinesq hypothesis that relates the components of the Reynolds stress tensor to the turbulent kinetic energy, the mean velocity gradients and the turbulent viscosity as

$$\overline{u_i u_j} = \frac{2}{3} k \delta_{ij} - \nu_t \left(\frac{\partial \overline{U_i}}{\partial x_j} + \frac{\partial \overline{U_j}}{\partial x_i} \right), \tag{4-2}$$

where $\overline{u_i u_j}$ is the Reynolds stress tensor, k is the turbulent kinetic energy per unit mass, $\frac{\partial \overline{U_i}}{\partial x_j}$ and $\frac{\partial \overline{U_i}}{\partial x_j}$ are the mean-velocity gradients, and ν_t is the turbulent viscosity. In a turbulent viscosity model, ν_t can be in turn related to the turbulent kinetic energy and the energy dissipation rate as

$$\nu_t = C_\mu \frac{k^2}{\varepsilon}, \tag{4-3}$$

where ε is the energy dissipation rate per unit mass, and C_μ is an empirical constant depending on the flow configuration. In the standard $k-\varepsilon$ model, the standard value of C_μ adopted for a large number of flows is 0.09 (Pope, 2000).

Although the standard $k-\varepsilon$ model has been implemented in a large number of flows, its applicability is limited by two deficiencies, non-realizability and specificity. In fact, substituting (4-3) into (4-2), the normal components of the Reynolds stress tensor can be calculated as:

$$\overline{u_i u_i} = \frac{2}{3}k - 2C_\mu \frac{k^2}{\varepsilon}\frac{\partial U_i}{\partial x_i}. \tag{4-4}$$

Therefore, in the case of large strain rates (i.e., $\frac{\partial U_i}{\partial x_i} > \frac{1}{3C_\mu}\frac{\varepsilon}{k}$), the standard $k-\varepsilon$ model does not prevent the normal components of the Reynolds stress tensor from being negative, making the model non-physical or non-realizable. In addition, in the standard $k-\varepsilon$ model, the velocity field and the length scales are determined by solving two transport equations for k and ε. While the transport equation for k can be exactly derived from the Navier-Stokes equations as

$$\rho \frac{Dk}{Dt} = \frac{\partial}{\partial x_i}\left[\left(\mu + \frac{\mu_t}{\sigma_k}\right)\frac{\partial k}{\partial x_i}\right] + \frac{1}{4}\mu_t\left(\frac{\partial \bar{U}_i}{\partial x_j} + \frac{\partial \bar{U}_j}{\partial x_i}\right)^2 - \rho\varepsilon, \tag{4-5}$$

the transport of ε is modeled empirically as:

$$\rho \frac{D\varepsilon}{Dt} = \frac{\partial}{\partial x_i}\left[\left(\mu + \frac{\mu_t}{\sigma_\varepsilon}\right)\frac{\partial \varepsilon}{\partial x_i}\right] + \frac{1}{2} C_{1\varepsilon}\mu_t \frac{\varepsilon}{k}\left(\frac{\partial \bar{U}_i}{\partial x_j} + \frac{\partial \bar{U}_j}{\partial x_i}\right)^2 - C_{2\varepsilon}\rho\frac{\varepsilon^2}{k}, \qquad (4\text{-}6)$$

where ρ is the fluid density, μ is the fluid dynamic viscosity, $C_{1\varepsilon}$ and $C_{2\varepsilon}$ are model constants, $\bar{U}_i$ is the mean-velocity component in the direction $\mathbf{e_i}$, and σ_k and σ_ε are the turbulent Prandtl numbers for k and ε, respectively. Therefore, the empirical nature of the equation for ε prevents the standard $k-\varepsilon$ model from constituting a universal model applicable to any type of flow.

The realizable $k-\varepsilon$ model developed by Shih et al. (1995) aims at extending the capabilities of the standard $k-\varepsilon$ model to flows presenting large strain rates and characterized by rotation. This new model differs from the standard model by proposing a new formulation for the turbulent viscosity and a new transport equation for the energy dissipation rate. As suggested in **Equation (4-4)**, the only possibility to guarantee that the normal Reynolds stresses stay positive, even in the situation of large strain rate, is to make the coefficient C_μ variable. In the realizable $k-\varepsilon$ model, C_μ is expressed as

$$C_\mu = \frac{1}{A_0 + A_S \dfrac{U^* k}{\varepsilon}}, \qquad (4\text{-}7)$$

where A_0 and A_S are constants, and U^* is a function of the mean strain and rotation rates. This new formulation for C_μ ensures the realizability of the model.

The new transport equation is based on the observation that, away from solid boundaries, at high Reynolds number, the energy-dissipation rate can be directly related to the mean-square vorticity fluctuations as,

$$\varepsilon = \nu \overline{\omega_i \omega_i} \tag{4-8}$$

where ω_i is the vorticity fluctuation in the $\mathbf{e_i}$ direction. The exact derivation of the mean-square vorticity fluctuations from the Navier-Stokes equations and the modeling of the unclosed terms yields the final form of the transport equation for ε

$$\rho \frac{D\varepsilon}{Dt} = \frac{\partial}{\partial x_i}\left[\left(\mu + \frac{\mu_t}{\sigma_\varepsilon}\right)\frac{\partial \varepsilon}{\partial x_i}\right] + \rho C_1 S \varepsilon - \rho C_2 \frac{\varepsilon^2}{k + \sqrt{\nu \varepsilon}} \tag{4-9}$$

where C_1 is a constant depending on k, ε and the mean strain rates, C_2 is a model constant, and S is a function of the mean strain rate. Because the rate of energy dissipation contains the effects of the vorticity statistics, this model is expected to perform better than the standard model in the case of flows involving rotation.

The experimental flow characterization described in the previous chapter showed that the flow was primarily driven by the rotation of the stir bar. The turbulent flow field was also characterized by a strong secondary flow caused by the suction occurring in the wake of the stir bar. Recirculation regions could finally be isolated near the lower surface of the construct closest to the impeller. The presence of such features suggested the implementation of the realizable $k-\varepsilon$ model. Because this work constituted the first attempt to apply this model in such a geometry, the constants defined in the transport equations were fixed at their standard values, i.e., σ_k = 1.0 (Launder and Spalding, 1972), σ_ε = 1.2 and C_2 = 1.9 (Shih et al., 1995).

Solver parameters

FLUENT offers many different numerical schemes to compute the time- and space-dependent variables involved in the flow equations. The solver computes the flow solution using a control-volume approach by integrating the governing equations on the discreet control volumes contained in the grid, and solving the linearized equations to obtain updated values of the flow quantities at the cell nodes and faces. The numerical scheme chosen for the implementation of the realizable $k-\varepsilon$ model in the bioreactor geometry was the segregated method. This iterative scheme solves the flow variables sequentially. First, the current values of the flow variables are used to compute a solution to the Reynolds-averaged Navier Stokes equations. Corrections on the pressure, mean-velocity components and face mass fluxes are then determined and applied to the calculated variables so that the computed velocity field satisfies the condition of continuity. In the last step, the transport equations for k and ε are solved. Finally, a new iteration is performed unless convergence based on user-defined criteria is obtained.

The spatial and temporal linearization methods associated with the segregated solver are implicit, i.e., the value of a given variable in a specific cell in the domain is computed from known and unknown values in neighboring cells. Therefore, the complete determination of a particular flow quantity throughout the entire geometry was performed by solving a linear system of equations in which the unknowns were the values of the variable of interest in each cell. Because the flow generated in the spinner flask was periodic, the governing equations also had to be discretized temporally. The first-order-accurate backward scheme that computes a specific flow variable in the entire geometry at the current time step from the values obtained at the previous time step was chosen for this purpose.

Wall treatment

Because the numerical model focused on the determination of the level of mean-shear stress on the surface of the constructs, the flow computation in the near-wall region was critical. The presence of walls in a flow field is known to affect both the mean flow and the turbulence. The no-slip and no-penetration conditions that must be satisfied on the wall surface impose different constraints on the flow velocity. In fact, turbulence is attenuated in the viscous sublayer where viscosity affects momentum transfer, whereas it is stimulated by the presence of large mean-velocity gradients in the fully-turbulent layer. Because the general turbulence models are only capable of predicting the characteristics of the flow in the bulk region, the complex physical modifications occurring in the near-wall region must be accounted for by other means.

The realizable k-ε model was implemented along with the enhanced-wall treatment available in FLUENT. Rather than using wall functions to resolve the turbulence in the near-wall region, this procedure locally modifies the turbulence model to make it applicable continuously throughout the entire flow field. Following this approach, the flow domain was subdivided into a fully-turbulent region where the flow was predicted by the realizable $k-\varepsilon$ model, and a viscosity-affected region where the flow was solved by a one-equation model relating the turbulent viscosity to the turbulent kinetic energy (Wolfstein, 1969).

Porous construct modeling

Porosity and permeability

The constructs used during tissue growth are porous in order to let the cells attach, migrate, and synthesize their matrix. A porous medium is defined essentially by two properties, porosity and permeability. The porosity is related to the microstructure of the medium. It represents the ratio of pores (i.e., void) in the medium to its total solid volume. In tissue-engineering applications, the scaffold pore size is a critical parameter depending on the type of cells in culture, and porosities as high as 97% are common. The permeability relates the microstructure of the medium to its resistance to conduct a fluid flow. This property is dependent on multiple characteristics such as pore size, shape, orientation and distribution. Because the medium is generally not homogeneous, the permeability is often defined as a 3×3 diagonal tensor $\left[\alpha_{ij}\right]$ whose components are the permeability values along each of the three principal directions of the porous medium. This tensor can then be related to the pressure gradient and fluid velocity across the medium using the Darcy law expressed as

$$\left[\alpha_{ij}\right]\nabla\mathbf{P}=-\mu\mathbf{U}\,, \tag{4-10}$$

where $\nabla\mathbf{P}$ is the pressure gradient across the medium, μ is the dynamic viscosity of the liquid, $\left[\alpha_{ij}\right]$ is the permeability tensor, and $\mathbf{U}$ is the average-velocity of the fluid across the porous medium. For a homogeneous porous medium, the permeability is constant for any direction and the diagonal elements are all equal. The one-dimensional form of **Equation (4-10)** can then be simplified as

$$\nabla P=-\frac{\mu}{\alpha}U\,, \tag{4-11}$$

where ∇P is the pressure gradient, U is the velocity component, and α is the permeability of the medium in the direction along which ∇P and U are measured. When the constructs were modeled as porous media, this form of the Darcy law was implemented in FLUENT to resolve the flow within the scaffolds.

Permeability measurements

The scaffolds used in the prototype spinner flask were small cylinders (diameter: 1 cm; thickness: 3 mm) made of PGA, and with a porosity of 97%. Because the permeability is a function of the pressure drop imposed across the medium, its value was not readily available for this specific material. Therefore, experiments had to be designed to measure the permeability of the constructs used during tissue growth. The measurements were based on the one-dimensional Darcy law derived from **Equation (4-11)**. By generating a known and constant pressure drop across a construct of given thickness, and by measuring the flow rate of fluid across the construct, the permeability could be deduced. The setup designed for the measurements is shown in **Figure 4.3**. The scaffolds provided by Smith & Nephew were non-woven PGA discs (1 cm in diameter, 2 mm in thickness). The base of a perfusion bioreactor designed by Advanced Tissue Science was used as a holder to maintain the construct in position. The holder was placed above a large beaker

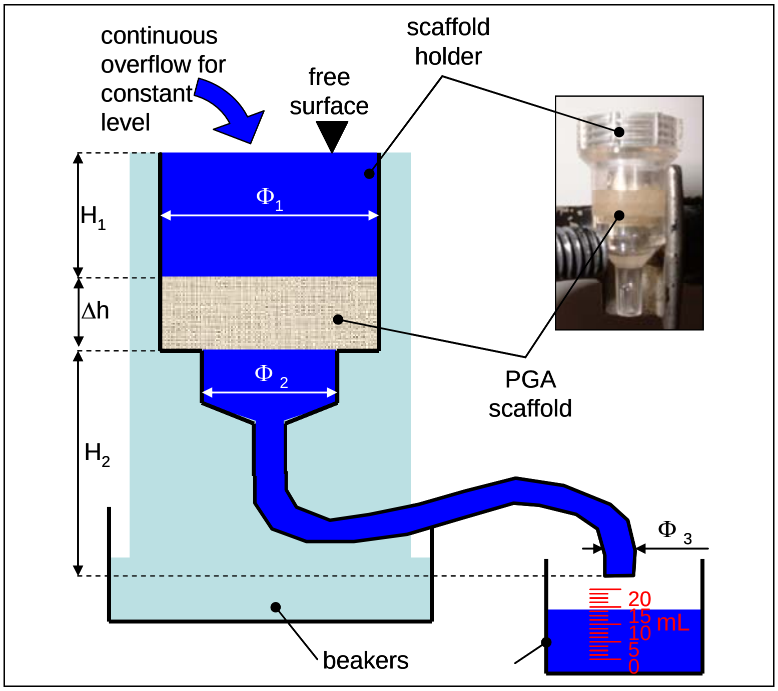

Figure 4.3: Schematic of the setup designed for the measurement of the PGA scaffold permeability.

to retrieve the liquid continuously supplied to the upper chamber. A plastic pipe connected to the end section of the bioreactor was placed above a smaller scaled beaker where the liquid exiting the apparatus could be collected. This setup allowed one to continuously overflow the construct holder in order to maintain a constant level of liquid above the porous scaffold. The pressure gradient in the vertical direction could be determined by applying the Bernoulli equation successively between the free surface of the liquid at the top of the apparatus and the top surface of the construct, and between the lower surface of the construct and the outlet of the connected pipe. Assuming atmospheric pressure at the free surface and at the pipe exit, and accounting for the major head loss in the pipe, the pressure gradient could be calculated as

$$\nabla P = \frac{8\rho Q^2}{\pi^2 \Delta h}\left(\frac{1}{{\Phi_3}^4} - \frac{1}{{\Phi_2}^4} + \frac{1}{{\Phi_1}^4} + \frac{16\mu\pi L_3}{\rho Q {\Phi_3}^4}\right) - \frac{\rho g_r \left(H_1 + H_2\right)}{\Delta h}, \tag{4-12}$$

where Q is the flow rate of liquid exiting the pipe, Δh is the thickness of the porous medium, Φ_1 is the diameter of the holder above the scaffold, Φ_2 is the diameter of the holder below the scaffold, Φ_3 is the diameter of the pipe, L_3 is the pipe length (i.e., 8 cm), g_r is the gravity constant, H_1 is the vertical distance between the free surface and the top surface of the construct, and H_2 is the vertical distance between the lower surface of the construct and the pipe exit. By stacking multiple constructs on top of one another and thus changing the value of Δh, it was possible to modulate the pressure drop imposed across the porous medium. The knowledge of the pressure gradient across the construct and the measurement of the flow rate at the pipe exit permitted the calculation of the permeability using **Equation (4-11)**. Because of limitations such as the size of the scaffold holder, the setup allowed the measurement of the permeability for four pressure gradients with absolute values ranging from 8.3×10^4 to 4.2×10^5 N.m^{-3}. For each of those, the permeability measurements were averaged over five realizations. Prior to each realization, the porous medium was thoroughly wetted with ethanol in order to reduce its hydrophobicity and prevent the formation of air bubbles within its pores. The experiments were carried out with distilled water at a temperature of 25°C ($\rho = 997$ kg/m^3 and $\mu = 9 \times 10^{-4}$ N.s/m^2). The variations of the permeability versus the pressure gradient are reported in **Figure 4.4**. The calculation of the uncertainty intervals is given in **Appendix C**. The permeability decreased from $2.22 \times 10^{-10} \pm 9.83 \times 10^{-12}$ to $6.98 \times 10^{-11} \pm 5.59 \times 10^{-12}$ m^2 with increasing pressure gradients yielding a mean permeability of 1.72×10^{-10} m^2 over the studied range of pressure gradient. Permeabilities of the same order had been found by Agrawal et al. (2000) in PLA-PGA scaffolds. The trend observed on the graph suggests the strong dependence of the material permeability on the imposed pressure gradient. In fact, variations in pressure gradient are accompanied by modifications in the microstructure of the porous medium, resulting

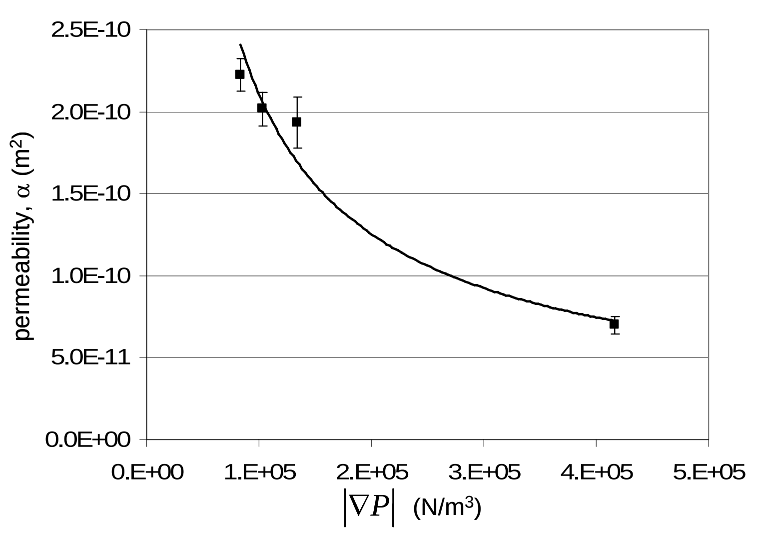

Figure 4.4: Variation of the PGA scaffold permeability as a function of the pressure gradient.

in a modification of its permeability. Fitting a power law to the data permitted an analytical relation between permeability and pressure gradient to be obtained:

$$\alpha = 1\times 10^{-6}\left|\nabla P\right|^{-0.75}, \tag{4-13}$$

The correlation coefficient relative to this fit is calculated as $R^2 = 0.972$.

Model validation

The performance of the turbulence model in the spinner flask was assessed by comparing the computational results with those from the PIV measurements described in the previous chapter. The model bioreactor was chosen to operate at 32.4 rpm in order to simulate an actual angular velocity of 50 rpm in the prototype reactor used by Vunjak-Novakovic et al. (1996). The effects of gravity were accounted for when solving the Reynolds-averaged Navier-Stokes equations. Since the flow experiments were performed in a bioreactor featuring solid constructs, those elements were also modeled as solids in the CFD geometry. The flow field was initialized at time $t = 0$, with the stir bar aligned along the $\mathbf{e_1}-$direction (**Figure 4.2**). Half a revolution of the stir bar was discretized into 40 time intervals, resulting in a time step $\Delta t = 23.1$ ms. About 800 iterations were needed to obtain convergence at the first time step. After the first time step, convergence could be obtained in 10 iterations. **Figure 4.5** shows the time history of the $x_2-$and x_3-components of the mean velocity at a point located on the upstream side (i.e., 2 mm from the construct wall) of the top construct threaded on the front array. The π-periodic sinusoidal pattern of the velocity components corresponds to the periodicity of the flow. Transient effects were considered negligible after 2040 time steps, i.e., a flow time of 47.1 s. The computation required 200 hours of processing time. The geometry and data files were stored every 80 time steps, occupying eventually 7.8 Gb.

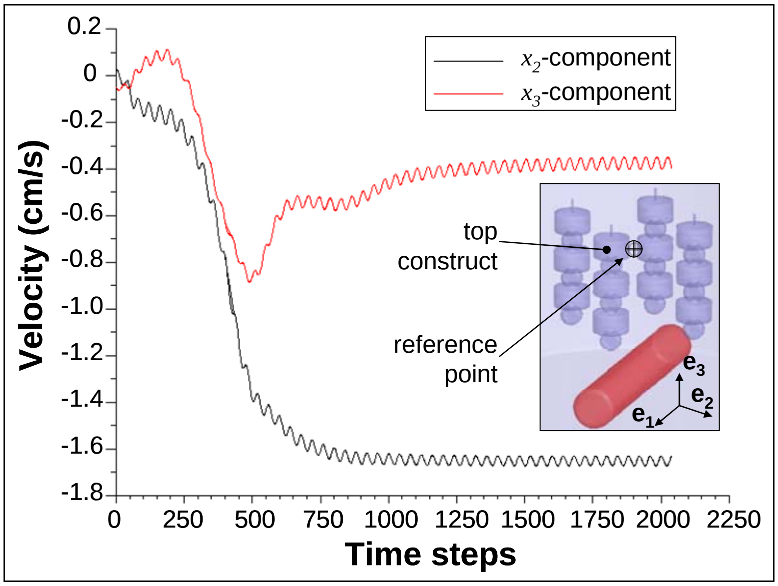

Figure 4.5: Time history of the x_2- and x_3-components of the mean velocity at a point on the upstream side of the top construct threaded on the front needle.

After the computation of the transient effects, the mesh was refined within a cylindrical region centered on the front array and with a diameter exceeding that of the construct by 1.6 cm (**Figure 4.6**). The final computational grid contained 703,706 cells, i.e., 36% more cells than in the coarse mesh. Then, computations were run for one period of the stir bar (i.e., 40 time steps). The case and data files defining the geometry as well as the fluid variables were stored at the end of each time step, occupying eventually 5.2 Gb of storage. The computation of the 40 time steps required 6 hours of processing time. In order to ensure that the flow solution computed by FLUENT was mesh-independent, the variations of the mean-velocity magnitude $\bar{U}(\mathbf{x},t)$ defined as

$$\bar{U}(\mathbf{x},t)=\left[\bar{U}_1^2(\mathbf{x},t)+\bar{U}_2^2(\mathbf{x},t)+\bar{U}_3^2(\mathbf{x},t)\right]^{\frac{1}{2}} \tag{4-14}$$

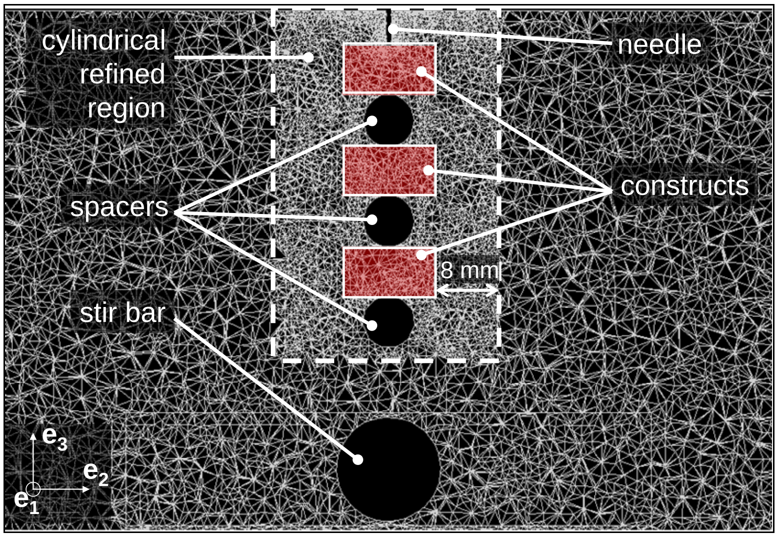

Figure 4.6: Cross-section of the final mesh obtained after refinement in a cylindrical region containing the front array.

and computed using the coarse and refined mesh were compared at three points located on the upstream side of the reference needle over one revolution of the stir bar (**Figure 4.7**). Although the variations of the mean-velocity magnitudes computed with the two meshes are very similar at point 1, point 2 and point 3, the root-mean square values calculated over one period of the stir bar still indicate a small dependence of the velocity on the mesh size. This observation is particularly true at point 1 and point 2 (i.e., near the stir bar) where the root-mean square values are almost one order of magnitude larger than at point 3. However, the refined mesh produced in the flask geometry was the finest possible that could be generated without leading to significant mesh errors or convergence issues.

Figure 4.8 shows a comparison of the mean-velocity vectors and magnitudes obtained by PIV and FLUENT in the vicinity of the bottom construct threaded on the front array as the stir bar is aligned along the $\mathbf{e}_1$-direction. Those results shown in the $\left(\mathbf{e}_2, \mathbf{e}_3\right)$-plane containing the diameter of the front construct array are based on the in-plane velocity defined as

$$\overline{\mathbf{U}}_{23}\left(\mathbf{x},t\right)=\overline{U}_2\left(\mathbf{x},t\right)\mathbf{e}_2+\overline{U}_3\left(\mathbf{x},t\right)\mathbf{e}_3, \tag{4-15}$$

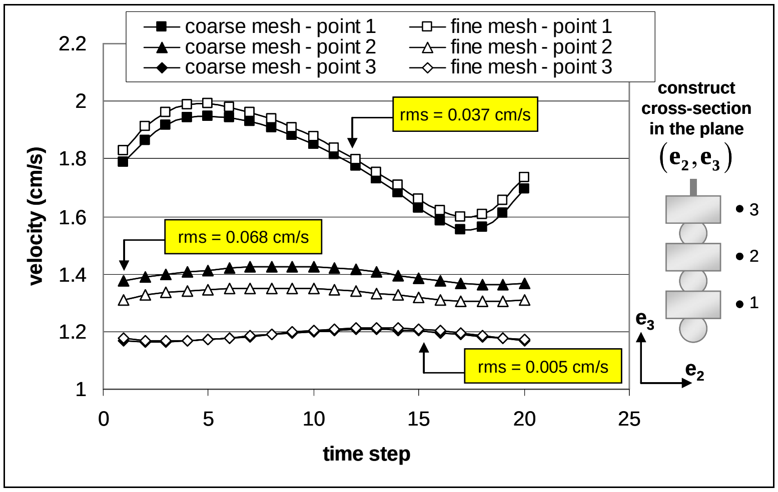

Figure 4.7: Variations of the mean-velocity magnitude computed in the coarse and refined mesh at three points located on the upstream side of the reference needle, over one period of the stir bar.

where $\bar{U}_2(\mathbf{x},t)$ and $\bar{U}_3(\mathbf{x},t)$ are the magnitudes of the velocity components in the $\mathbf{e}_2$ and $\mathbf{e}_3$ directions, respectively.

Locally, the vectors indicated in the velocity fields of **Figure 4.8a** and **Figure 4.8b** have similar orientations and directions. The stagnation point located on the upper surface, on the upstream side of the construct as demonstrated on the PIV results is well predicted by FLUENT. In addition, the measurements and the simulations show the existence of a recirculation region located in the upstream region, between the bottom spacer and the lower surface of the construct. The velocity contours shown in **Figure 4.8c** and **Figure 4.8d** have a similar appearance both near and far from the construct. Because the construct constitutes an obstacle for the flow, higher velocity magnitudes can be observed in the region far upstream of the construct than in the region far downstream. As expected, the maximum velocities are found close to the stir bar, on the upstream side of the construct.

A quantitative comparison of the velocities measured by PIV and predicted by FLUENT is shown in **Figure 4.9**. This graph shows the variations of the x_2- and x_3-components of the mean velocity obtained at a reference point located on the upstream side of the bottom construct

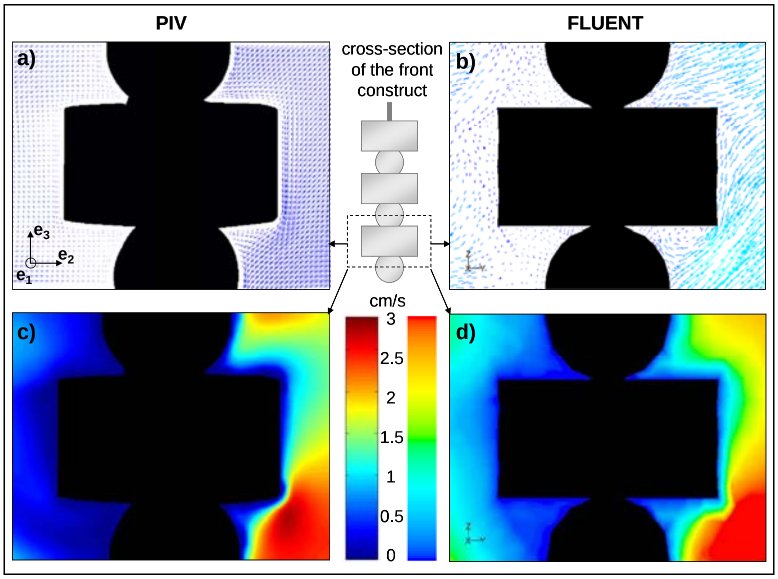

Figure 4.8: Comparison of the mean-velocity vectors and magnitudes obtained with PIV (a and c, respectively) and FLUENT (b and d, respectively) at an instant of time.

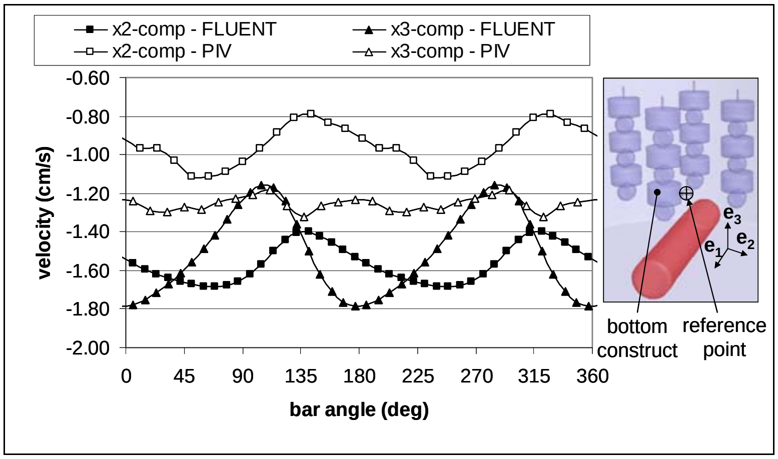

Figure 4.9: Comparison of the variations of the x_2- and x_3-components of the mean velocity obtained at a point on the upstream side of the bottom construct over one revolution of the stir bar.

over one revolution of the stir bar. Although the two techniques indicate the same flow periodicity, a systematic discrepancy can be observed between the prediction and the laboratory measurements. The same discrepancy can be observed between results obtained at other reference points located further from the stir bar. In those comparisons, the FLUENT model over- or under-predicts the PIV velocity measurements but the largest discrepancy obtained close to the impeller and shown in **Figure 4.9** is about 0.5 cm/s. This qualitative velocity difference whose magnitude is apparently dependent on the distance from the stir bar is believed to be related to the poor performance of the current turbulence models in the case of complex geometries such as the spinner flask. Although the accuracy of the CFD model could certainly be improved by optimizing the mesh, the model parameters and the order of accuracy at which the computations were conducted, the realizable $k-\varepsilon$ model showed its capability to fairly simulate the general flow configuration in the vicinity of the constructs at a reasonable computational cost, and is considered a more reliable tool than the standard $k-\varepsilon$ model for the design of the future tissue-growth model.

Porous construct computations

Permeability estimate

As addressed earlier, one of the difficulties associated with flow computations in a porous medium was the determination of the permeability given the dependence of this property on the pressure gradient imposed across the medium. The setup designed to quantify the permeability of a PGA construct allowed measurements relative to pressure gradients of the order of 10^5 N/m^3. In an effort to produce an estimate of permeability for the range of pressure gradients actually present across a construct in the model bioreactor, the pressure field computed by the validated flow model had to be examined on the surface of a scaffold threaded on the reference needle. A pressure map obtained at an instant of time is shown in **Figure 4.10**. For the bottom, middle or

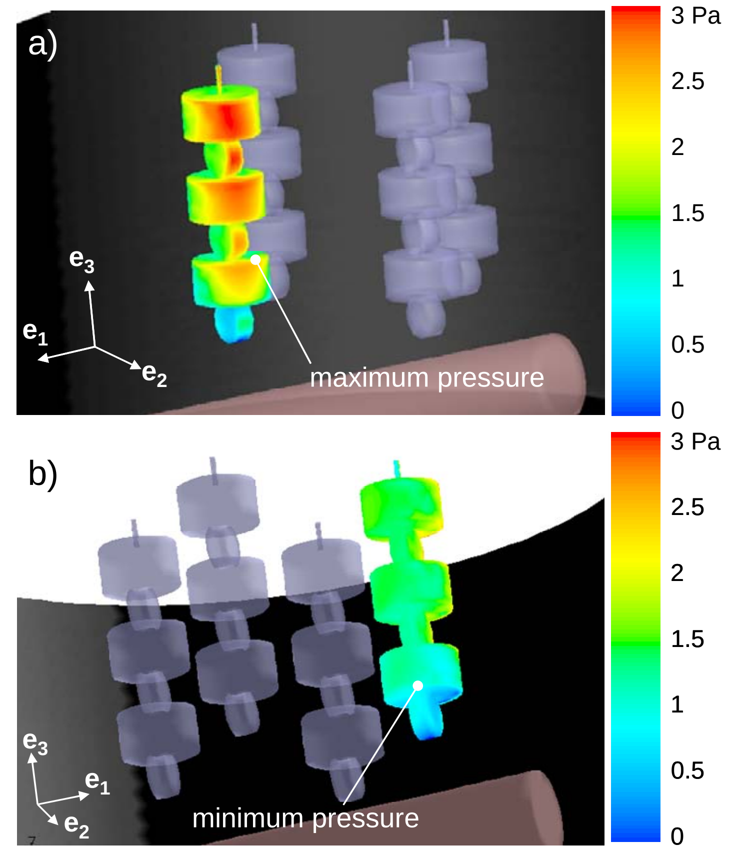

Figure 4.10: Pressure field obtained on the surface of solid constructs computed by the realizable $k-\varepsilon$ model. For all the constructs (i.e., bottom, middle, or top), the pressures observed on the top surface (a) were systematically larger than those on the bottom surface (b).

top construct, the maximum pressure was systematically obtained on the top surface, near the stagnation points observed experimentally (**Figure 4.10a**). For the three constructs, the pressures obtained on the lower surface were systematically smaller (**Figure 4.10b**). The maximum pressure drop obtained over one period of the stir bar, across the bottom construct and along the direction $\left(0,-1,-1\right)$ could be estimated as 3.1 N/m^2. The length of the porous scaffold along this direction (i.e., 1.27 cm) resulted in a pressure gradient $\nabla P = -244\ \text{N/m}^3$. This pressure gradient was assumed to be the maximum pressure gradient across any direction of any construct present in the model bioreactor. Although the power law described in **Equation (4-13)** was obtained by fitting permeability data relative to pressure gradients three orders of magnitude larger than that predicted across a construct, it was the only available tool to estimate the permeability of the constructs in the bioreactor. In fact, the implementation of a pressure gradient as low as -244 N/m^3 in the permeability-measuring apparatus would have required stacking four constructs to increase the height of the porous medium, removing the plastic pipe at the holder exit to set the pressure at the bottom of the construct as atmospheric, and continuously overflowing the construct holder with a height of 0.2 mm of water. The difficulty to satisfy such requirements left as a unique option to extrapolate the power law described in **Equation (4-13)** to a low pressure-gradient value. The permeability resulting from this analysis was $\alpha = 1.62 \times 10^{-8}$ m^2. This value whose validity cannot be ascertained was assumed to be an estimate of the initial scaffold permeability, prior to tissue growth.

Mean velocity

The validated model was used to predict the flow field in a geometry featuring porous constructs. The first computation was performed for PGA scaffolds with a porosity of 97% and a permeability of 10^{-8} m^2. Additional computations were performed for decreasing values of permeability (i.e., 10^{-10} m^2, 10^{-12} m^2 and 10^{-14} m^2) in order to simulate the physical effects of the tissue growth process during which cell progressively migrate and attach onto the constructs.

Figure 4.11 shows the mean-velocity fields obtained at an instant of time (stir bar aligned along the $\mathbf{e_1}-$direction) in the vicinity of the bottom construct, for permeabilities of 10^{-8} m^2 and 10^{-14} m^2. The velocity fields computed outside the constructs show similar trends. Consistent with the observations made previously on the PIV measurements performed in the same region (**Figure 4.8c**), the velocity magnitude is higher on the upstream than on the downstream side of the construct. Additionally, the velocities are affected by the distance from the stir bar. In fact, higher magnitudes are detected near the bottom of the field while lower velocities are observed near the top. Finally, The flow generated within the constructs medium is dependent on the

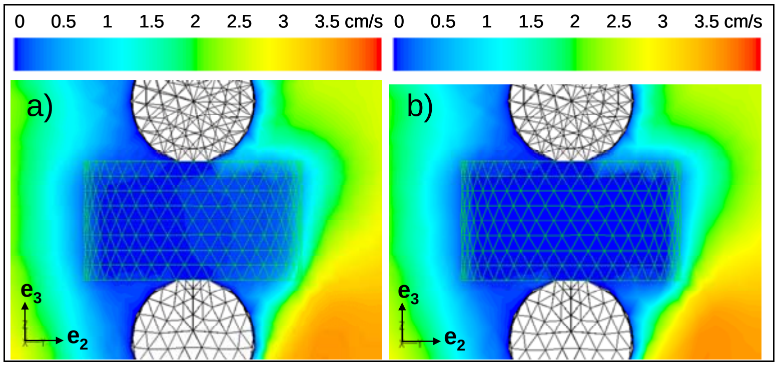

Figure 4.11: Contour of the mean-velocity magnitude obtained in the vicinity of the bottom construct for two different permeabilities: a) $\alpha = 10^{-8}$ m^2; and b) $\alpha = 10^{-14}$ m^2.

permeability. As expected, at high permeability, the fluid penetrates the construct over a large region, at least on the upstream side of the porous medium (**Figure 4.11a**). At low permeability, the porous medium offers more resistance to the flow, hence limiting the flux of fluid across the wall of the scaffold (**Figure 4.11b**).

Flow-rate analysis

In addition to the characterization of the flow field in the vicinity of the constructs, a flow rate analysis was performed on the surface of the bottom construct. The entire surface was discretized into four faces: the top surface, the bottom surface, the lateral right surface on the upstream side, and the lateral left surface on the downstream side. The variations of the flow rates through each surface are shown in **Figure 4.12** for permeabilities of 10^{-8} m^2 and 10^{-14} m^2. The results obtained for the two cases share some similarities. As expected, positive flow rates are obtained for the top and lateral right surfaces where the flow enters the construct (i.e., inflow surfaces) whereas the bottom and lateral left surfaces are characterized by negative flow rates (i.e., outflow surfaces). In addition, a symmetry can be observed between the flow rates through the top and lateral left surfaces, and between the bottom and lateral right surfaces. Quantitatively, most of the flow enters the construct through the upstream surface (i.e., lateral right surface) and

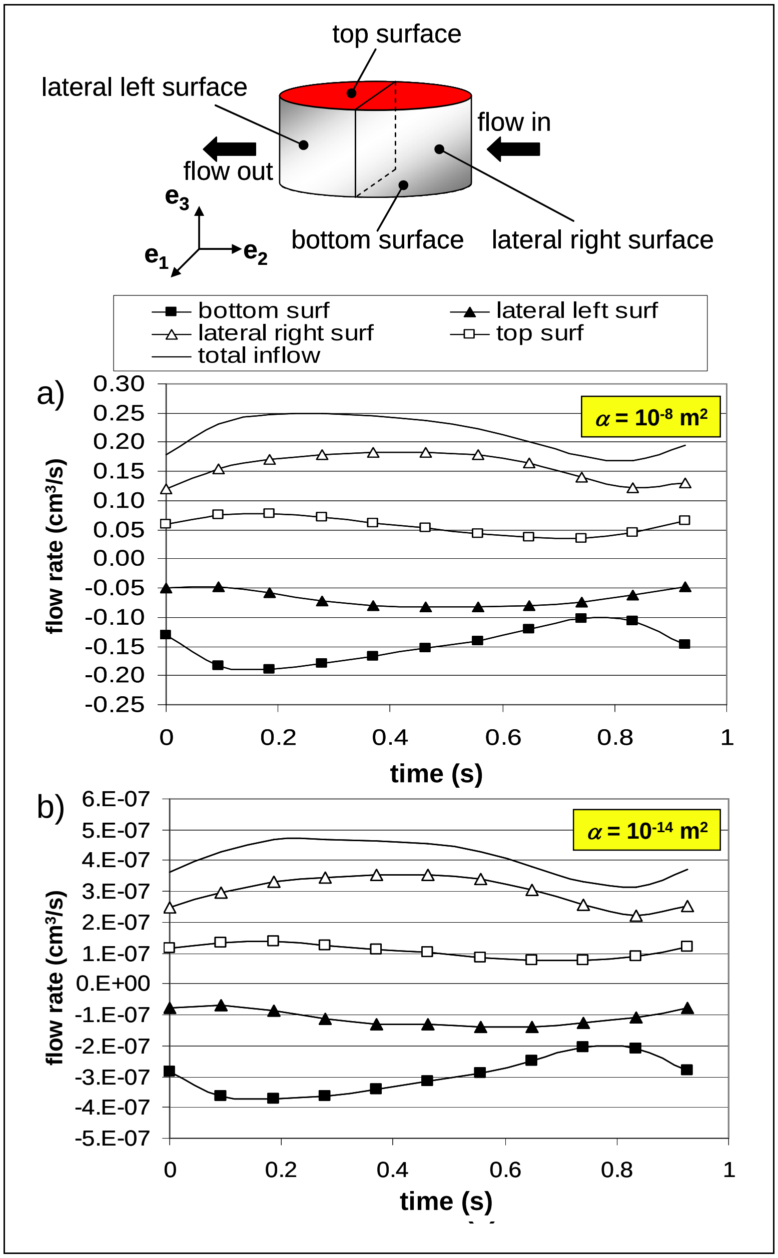

Figure 4.12: Variations of the flow rates across the top, lateral right, lateral left, and bottom surfaces of the bottom construct over one period of the stir bar, for two permeabilities: a) $\alpha = 10^{-8}$ m^2; and b) $\alpha = 10^{-14}$ m^2.

exits through the bottom surface, suggesting that the general flow orientation is aligned along the construct diagonal. The comparison of the flow rates obtained for the two permeabilities supports the observations made earlier on the respective velocity fields. The maximum flow rate of fluid penetrating the construct at a permeability of 10^{-8} m^2 is 0.25 cm^3/s whereas that computed for the construct at a permeability of 10^{-14} m^2 is only 0.5 mm^3/s, as shown in **Figure 4.12a** and **Figure 4.12b**, respectively. Normalizing those values by the maximum possible flow rate (i.e., the flow rate that would be obtained if the constructs were modeled with a permeability equal to 1 m^2) suggests that 6.8% of the maximum flow rate is obtained through the scaffold at a permeability of 10^{-8} m^2, and only 1.3×10^{-5} % at a permeability of 10^{-14} m^2.

Mean-shear stress

The mean-shear stress level on the surface of the constructs has been analyzed and quantified. This variable defined as a user-defined function in FLUENT includes the effects of the three mean-shear stress components, $\overline{\tau}_{12}$, $\overline{\tau}_{13}$ and $\overline{\tau}_{23}$, and can be written as

$$\overline{\tau}\left(\mathbf{x},t\right)=\left[\overline{\tau}_{12}^2\left(\mathbf{x},t\right)+\overline{\tau}_{13}^2\left(\mathbf{x},t\right)+\overline{\tau}_{23}^2\left(\mathbf{x},t\right)\right]^{\frac{1}{2}} \tag{4-16}$$

where $\overline{\tau}_{ij}\left(\mathbf{x},t\right)$ is the *ij*-component of the mean-shear stress tensor. **Figure 4.13** shows the instantaneous mean-shear stress obtained on the surface of the bottom (**Figure 4.13a**), middle (**Figure 4.13b**), and top (**Figure 4.13c**) constructs at an instant of time for a permeability of 10^{-10} m^2. The maximum wall shear stress obtained for this particular configuration is 0.06 N/m^2. The comparison of the three fields suggests the dependence of the mean-shear stress on the distance from the stirring bar. In fact, the shear stress on the surface of the bottom construct is higher and more homogeneously distributed than that on the surface of the top construct which is

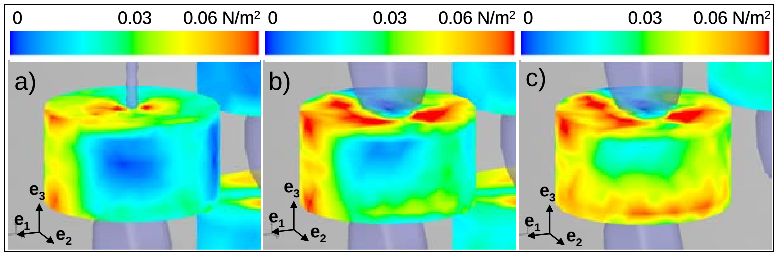

Figure 4.13: Comparison of the instantaneous wall-shear stress obtained on the surface of the a) top; b) middle; and c) bottom constructs, at a permeability of 10^{-10} m^2.

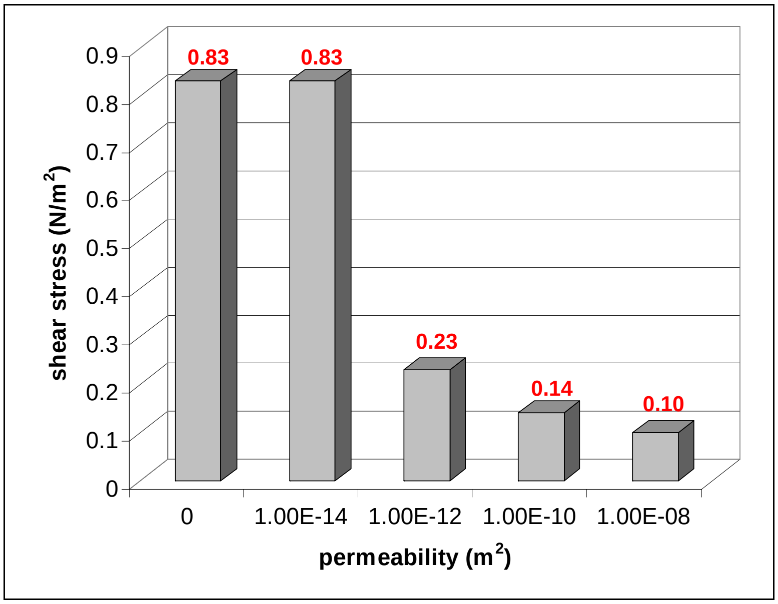

Figure 4.14: Variation of the maximum wall-shear stress detected on the surface of the constructs as a function of permeability.

concentrated near the needle. In addition, the maximum wall shear stress level obtained over one period of the stir bar on the surface of the constructs has been compared for permeabilities of 10^{-8} m^2, 10^{-10} m^2, 10^{-12} m^2, 10^{-14} m^2 and 0 m^2 (**Figure 4.14**). As expected, the maximum wall-shear stress increases with decreasing permeability. At a permeability of 10^{-8} m^2, the maximum stress level is one-eighth that predicted at a permeability of 10^{-14} m^2. Finally, the values of the maximum shear stress obtained at 10^{-14} m^2 and for a solid construct (i.e., theoretical permeability of 0 m^2) do not differ significantly.

Summary

In this section, a computational-fluid dynamic model was designed with FLUENT to predict the turbulent flow produced by the model spinner flask. The numerical results were compared to the laboratory measurements conducted previously in a similar bioreactor. Although a complete agreement between experimental and computational results could not be attained, the FLUENT model fairly predicted the flow features already observed with PIV. A laboratory setup was constructed in order to estimate the permeability of the PGA scaffolds used during tissue growth. The CFD model was then exploited to predict the flow field obtained within and outside porous constructs for decreasing permeability values. Finally, the maximum level of the wall-shear stresses computed on the surface of the constructs could be assessed.

CHAPTER 5

CARTILAGE-GROWTH MODEL

Tissue culture

In order to correlate the local flow predictions of the CFD model with the local growth of tissue on a scaffold, cartilage constructs had to be cultivated in the spinner-flask bioreactor described in Chapter 1. Our collaborators at MIT, Drs. Gordana Vunjak-Novakovic and Lisa Freed carried out the tissue-growth experiments in their lab. Cylindrical PGA scaffolds (diameter: 5 mm; thickness: 2 mm) with a porosity of 97% were used to provide the cells with a suitable attachment surface. Twelve scaffolds were threaded on the four equi-angularly spaced needles fixed in the cap of the flask at a distance of 1.24 cm from its center. The bioreactor was filled with 125.5 ml of culture medium (density: 1.03 g/cm^3; kinematic viscosity: 0.971 cSt – see Croughan et al., 1987). Three cylindrical spacers made of silicone tubing (diameter: 0.396 cm; thickness: 0.168 cm) were used on each needle to support the constructs (**Figure 5.1**). This configuration was expected to provide a better growth environment than that employed previously by preventing the top surface of each scaffold from contacting other solid. The top surface of the top, middle and bottom construct of each needle was located at 6 mm, 14 mm and 22 mm below the free surface, respectively, leaving a distance of about 7 mm between the bottom surface of the bottom construct and the upper part of the stir bar. The angular orientation of the three constructs threaded onto the reference needle was indexed by sewing a small piece of thread in the porous material at a location facing the center of the flask. The complete geometry of the flask can be appreciated in **Figure 5.2**.

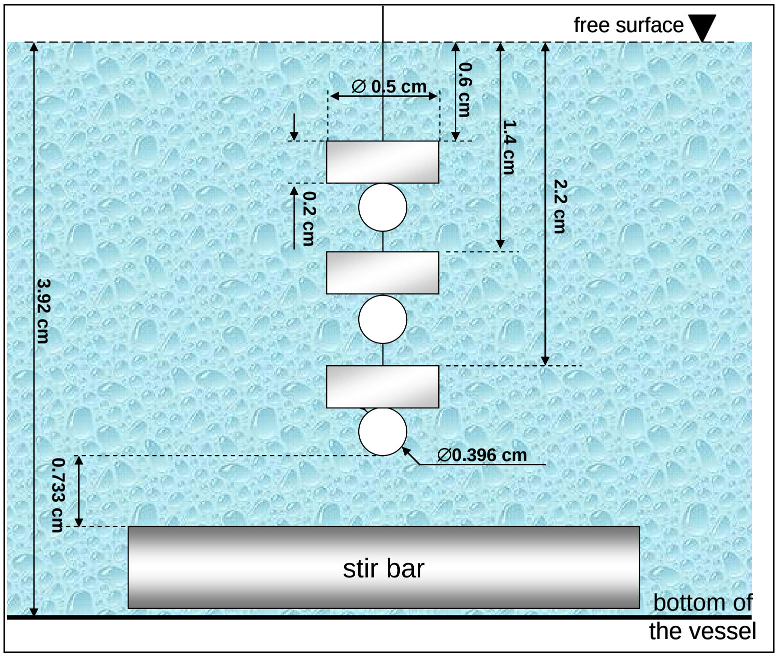

Figure 5.1: Layout of the reference needle used during tissue culture in the spinner flask.

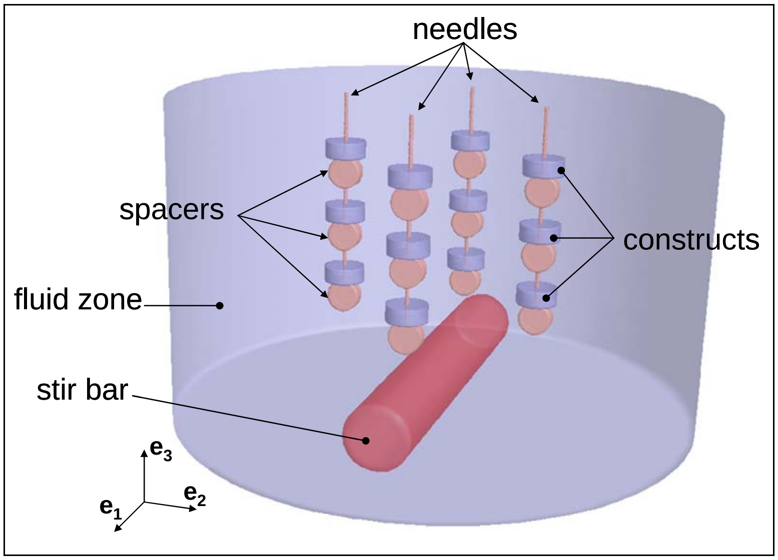

Figure 5.2: Three-dimensional geometry of the flask used during tissue culture. Initially, the stir bar is aligned along the $\mathbf{e}_1$ – direction.

Chondrocytes were dynamically seeded on 48 scaffolds. The resulting cell-polymer scaffolds were threaded onto 16 needles (each holding three scaffolds and three spacers). In order to account for the time dependence of tissue growth, the needles were separated into four groups and cultured for three days, ten days, four weeks and six weeks in four flasks (each containing four needles) operating under the same conditions. The magnetic impeller was rotated at an angular velocity of 50 rpm in the clockwise direction, when viewed from above.

Flow simulations

GAMBIT was used to create the three-dimensional geometry of the actual flask used for the tissue-growth experiments. As compared with the geometry described in Chapter 4, this new configuration featured a different construct size and a different needle configuration. In addition to the cues associated with the complex geometry of the spinner flask and already discussed in Chapter 4, an issue was raised by the presence of a small needle part intercalated between a construct and the spacer located directly above it. In fact, the presence of such a small element between two solids of larger size was expected to produce a discontinuity in the mesh. This problem was overcome by choosing different mesh sizes on the surface of needles, spacers and constructs, in the flask volume, and in the volumes occupied by the porous constructs. Surfaces were meshed using triangular elements of 0.4 mm whereas the constructs and flask volumes were filled with tetrahedral elements of 0.4 mm and 1.8 mm, respectively. The resulting mesh featured 1,152,485 elements, 2,435,363 faces and 225,732 nodes. The constructs were modeled as porous media with a porosity of 97% and a permeability of $\alpha = 1.62\times10^{-8}$ m^2, as determined experimentally (see Chapter 4). Initially, the stir bar was set parallel to the $\mathbf{e_1}-$direction.

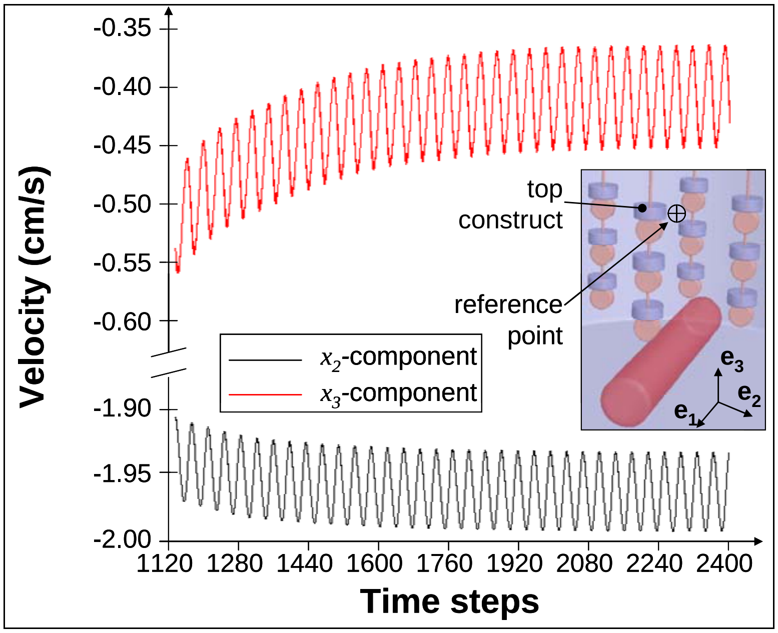

Figure 5.3: Time history of the x_2- and x_3-components of the mean-velocity at a point on the upstream side of the top construct threaded onto the reference needle (velocities are relative to the model bioreactor).

The fluid properties (i.e., dynamic viscosity and density), solver parameters, boundary conditions, and governing equations were set as those already defined in the preliminary model. The turbulent flow in the flask was solved using the realizable $k-\varepsilon$ model coupled with the enhanced wall treatment offered by FLUENT whereas the laminar flow in the porous scaffolds was computed using the standard Darcy law. The computation was launched using a time step of $\Delta t = 23.1$ ms. The time history of the x_2- and x_3-components of the mean-velocity at a point on the upstream side of the top construct threaded onto the reference needle (**Figure 5.3**) suggests that start-up effects could be neglected after 2400 times steps (i.e., 30 stir-bar revolutions). At that point, the mesh was refined within a cylindrical region of radius 1.2 cm, centered on the reference needle and extending from 8 mm below the bottom construct to 8 mm above the top construct (**Figure 5.4**). In that volume, 1,581,177 cells were marked for adaptation using the hanging-node technique in which an additional node was inserted between any two existing nodes in the mesh.

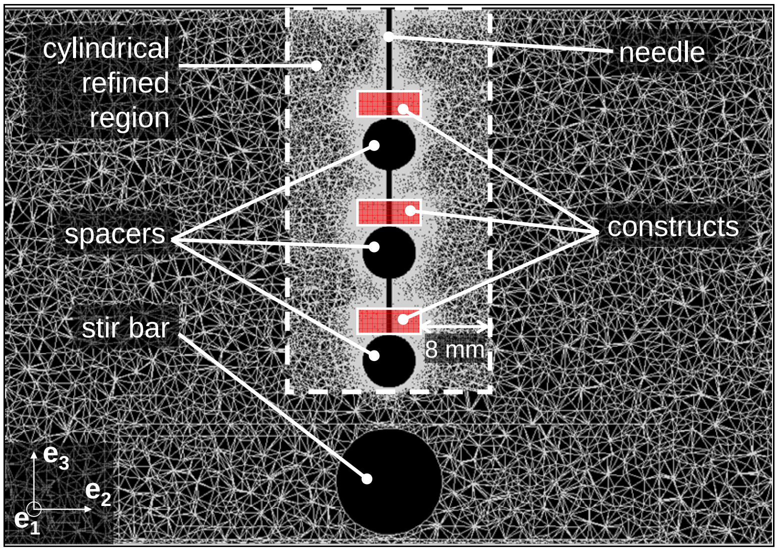

Figure 5.4: Cross-section of the final mesh obtained after refinement in a cylindrical region containing the front array.

This procedure generated a grid of 2,259,724 cells, representing an increase of 96% with respect to the number of cells contained in the coarse mesh. The mesh quality was inspected using the tools provided by the mesh-generator program. The maximum equiangle skew detected in the refined mesh was 0.93 with 79.74% of the cells presenting a skewness ranging from 0.2 to 0.5 (**Table 5-1**). The maximum cell volume calculated by GAMBIT was 3 mm^3. Finally, the aspect ratio of the mesh elements was found to be between 1 and 7. With such characteristics, the resulting mesh was expected to be suitable for the convergence of the flow solutions. The computation of the flow in its steady state was performed over one period of the stir bar (i.e., half a revolution), using the same time step as that implemented for the computation of the transient effects (i.e., $\Delta t = 23.1$ ms).

Mean velocity

Snapshots of the mean-velocity vector field $\overline{\mathbf{U}}_{23}(\mathbf{x},t)$ captured in the plane $(\mathbf{e}_2,\mathbf{e}_3)$ and obtained at an instant of time (with the stir bar aligned along the $\mathbf{e}_1 -$direction) in the vicinity of the top, middle and bottom constructs are shown in **Figure 5.5a**, **Figure 5.5b** and **Figure 5.5c**,

Table 5-1: Mesh-quality report produced by GAMBIT for equiangle skew.

From value	To value	Count in range	% of total count
0	0.1	40800	3.54
0.1	0.2	58314	5.06
0.2	0.3	202173	17.54
0.3	0.4	458731	39.80
0.4	0.5	258117	22.40
0.5	0.6	99424	8.63
0.6	0.7	28754	2.49
0.7	0.8	6120	0.53
0.8	0.9	50	0.01
0.9	1.0	2	0.00

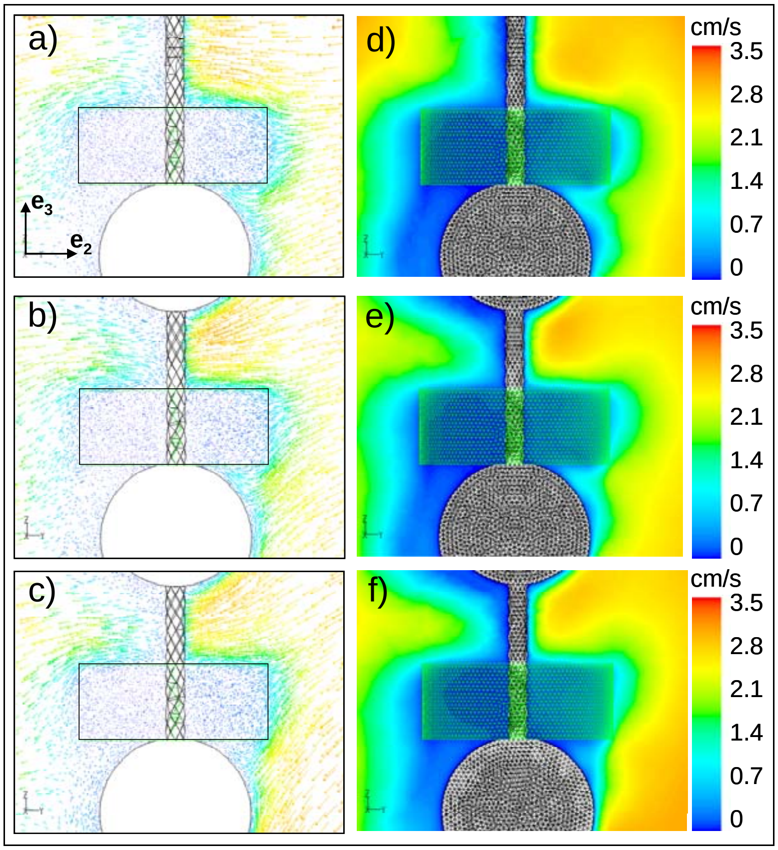

Figure 5.5: Mean-velocity vector and contour fields observed at time $t = 0$ in the vicinity of the top (a and d, respectively); middle (b and e, respectively); and top (c and f, respectively) constructs threaded onto the reference needle (velocities are relative to the model bioreactor).

respectively. The results suggest that the orientation of the flow is strongly dependent on the distance from the stir bar. In fact, the flow is oriented from top right to bottom left in the vicinity of the bottom construct whereas it is almost horizontal near the top construct. In addition, consistent with this observation, the location of the stagnation point is different for each construct. As the distance from the stir bar increases, the stagnation point moves from a location near the top to a location near the middle of the upstream edge of the construct. Finally, those differences in flow orientation affect the way the fluid flows around each construct. Two recirculation regions can be observed above the top surface and below the bottom surface on the upstream side of the top construct whereas there is only one below the bottom surface of the middle and bottom constructs.

The mean-velocity contour maps in the vicinity of the top, middle and bottom constructs are shown in **Figure 5.5d**, **Figure 5.5e** and **Figure 5.5f**, respectively. Not surprisingly, the velocity magnitude is higher upstream (i.e., on the right of the construct) than downstream. Similar to the flow orientation, the velocity is dependent on the distance from the stir bar and attains a maximum of 3.5 cm/s in the vicinity of the bottom construct. As already commented in the preliminary flow computations conducted in the previous chapter, the flow loses a lot of inertia as it approaches the surface of a construct and penetrates the construct volume only a short distance.

Mean-shear stress

The magnitude of the mean-shear stress was computed on the surface of the top, middle and bottom constructs according to **Equation (4-16)**. The results are presented in **Figure 5.6** where the top, middle and bottom constructs are shown on their downstream (**Figure 5.6a**, **Figure 5.6b** and **Figure 5.6c**, respectively) and upstream sides (**Figure 5.6d**, **Figure 5.6e** and **Figure 5.6f**, respectively). The direction of the flow with respect to the constructs is indicated as a black arrow and the shear-stress magnitudes are relative to the model bioreactor. On the

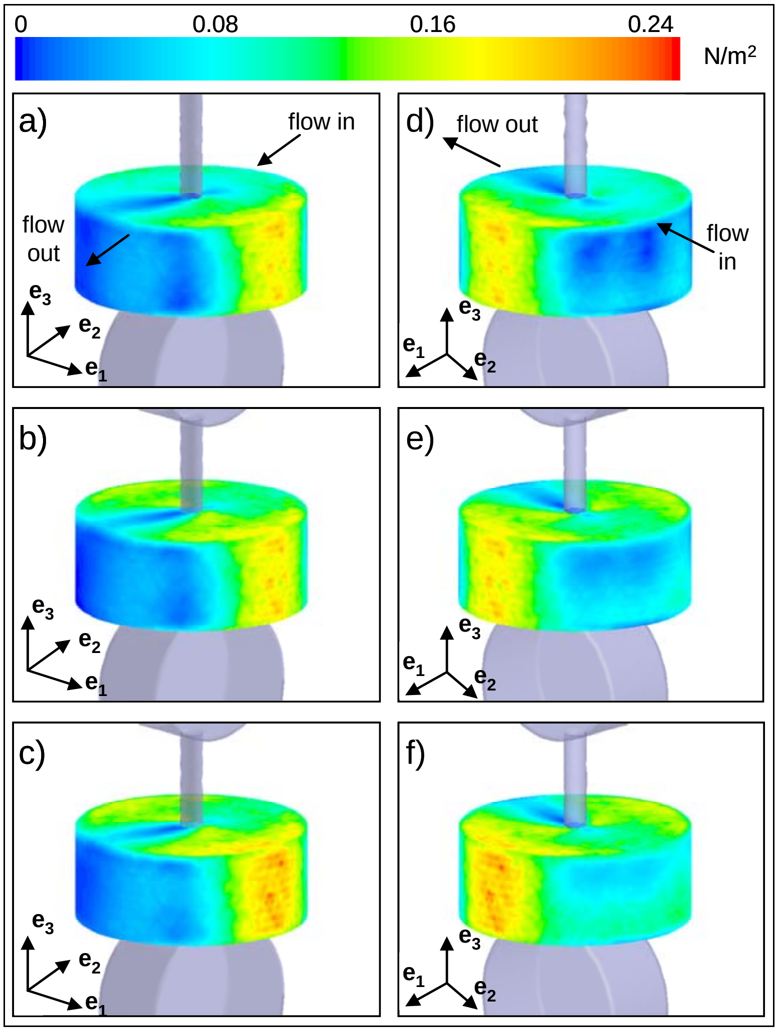

Figure 5.6: Mean-shear stress magnitudes obtained on two different views of the surface of the top (a and d, respectively), middle (b and e, respectively) and bottom (c and f, respectively) constructs threaded onto the reference needle. The black arrow indicates the flow direction. The magnitudes are relative to the model bioreactor.

upstream side of the construct surface, the wall-shear stress increases between the most upstream location (i.e., $x_2 = 0.4$ cm) and the mid-section (i.e., $x_2 = 0$ cm). In fact, the analysis of the velocity-vector field in the vicinity of the reference needle (see **Figure 5.5**) demonstrated a flow orientation essentially parallel to the $\mathbf{e}_2$ – direction, making $\bar{U}_2(\mathbf{x},t)$ the dominant velocity component of $\bar{\mathbf{U}}(\mathbf{x},t)$ in that region. As long as the incidence angle of the fluid particles hitting the construct surface remains close to 0° (i.e., flow direction parallel to the vector normal to the construct surface), the velocity gradients are dominated by the $\frac{\partial \bar{U}_2}{\partial x_2}$ – component that relates to a normal stress. In contrast, as the incidence angle becomes larger (i.e., flow direction perpendicular to the vector normal to the construct surface), the contribution of the normal component of the velocity gradients becomes milder and **Equation (4-16)** is dominated by the $\frac{\partial \bar{U}_2}{\partial x_1}$ – component. This justifies the presence of large wall-shear stress magnitudes (maximum value: $\bar{\tau}_m = 0.24$ N/m^2; $\bar{\tau}_p = 0.12$ N/m^2) in the vicinity of $x_2 = 0$ cm. In the downstream wall region comprised between $x_2 = 0$ cm and $x_2 = 0.4$ cm, the wall-shear stress decreases again due to the decreasing incidence angle and the lower velocity magnitudes present in the wake of the constructs.

Flow-rate analysis

The ability of the fluid to cross the surface of the constructs was investigated by analyzing the flow rates across their surfaces. The surface of each construct was divided into top, bottom, lateral-right (i.e., upstream) and lateral-left (i.e., downstream) surfaces. **Figure 5.7** shows the variations of the volumetric flow rate across each surface and total inflow entering each construct over half a stir-bar revolution. Although different trends can be drawn depending on the

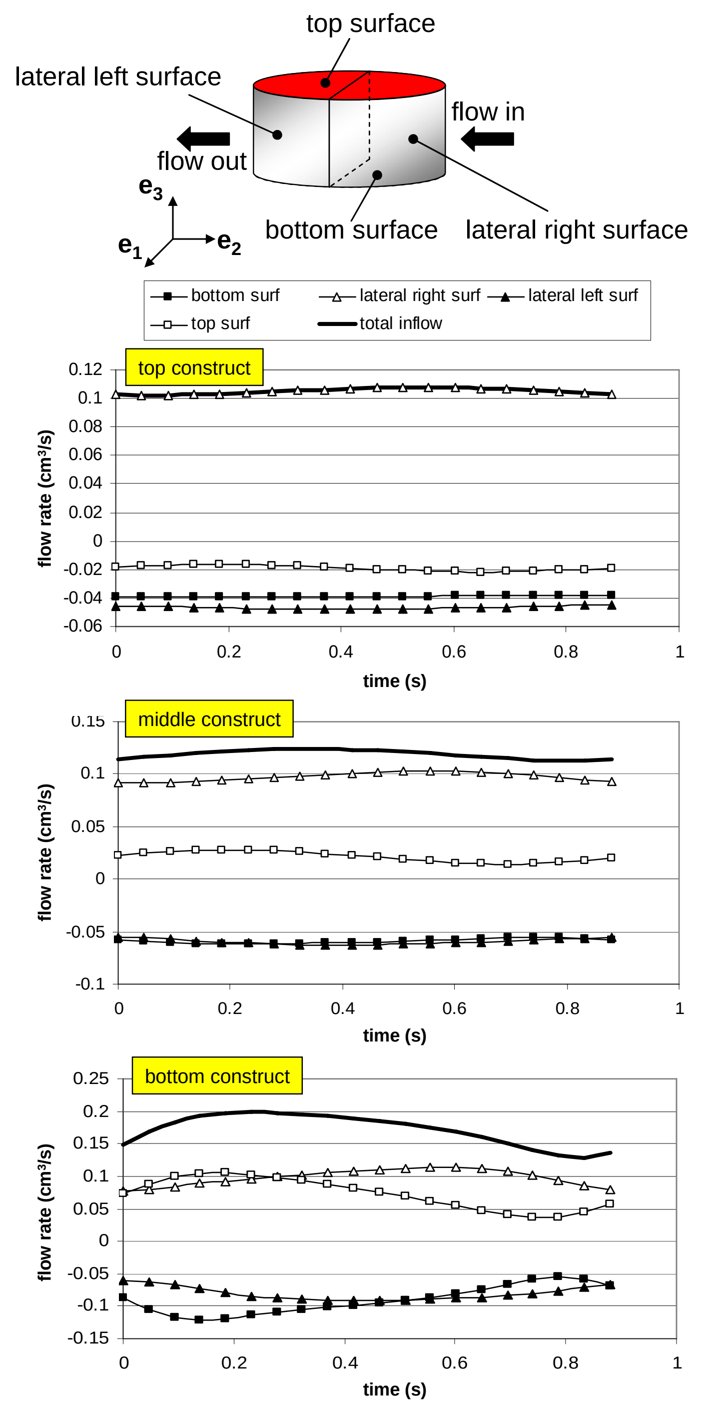

Figure 5.7: Variation of the flow rates across the top, lateral left, lateral right and bottom surfaces of the top, middle and bottom constructs over one period of the stir bar. Flow-rate values are relative to the model bioreactor.

observed construct, the rate at which fluid penetrates the construct decreases continuously as the distance from the stir bar increases.

The results relative to the bottom construct suggest that the fluid penetrates the porous material through the top and lateral-right surfaces for which the flow rates are constantly positive over a period, and exits through the bottom and lateral-left surfaces. This information is consistent with the general flow orientation described by the velocity-vector field in **Figure 5.5c**. Compared with the flow-rate analysis conducted in the preliminary computations on a construct of similar permeability and porosity (see **Figure 4.12a**), lower flow rates are obtained in the new bioreactor geometry. This is partly explained by the fact that, for the preliminary computations, the bottom construct was positioned closer to the stir bar and therefore positioned in a region of higher velocity magnitudes as compared with the present geometry. Quantitatively, the current computations demonstrate that the amount of fluid crossing the lateral-right (lateral-left) surface is not significantly different from that crossing the top (bottom) surface.

The flow-rate analysis performed on the middle construct shows some interesting differences. Most of the flow enters through the top surface although some fluid also penetrates via the lateral-right surface. This trend is supported by the earlier observations on the flow direction in the vicinity of this scaffold. Because the flow is more nearly tangential to the top surface, the flow rate across this surface becomes lower. Conversely, this change in flow orientation is accompanied by an increase in the flow rate across the lateral surface whose normal vector is more parallel to the flow direction. In addition, the flow rates computed across the bottom and lateral-left surfaces of the construct are very similar, suggesting that the fluid exits the construct with the same fluxes across those two surfaces.

Finally, the position of the top construct far from the agitation produced by the stir bar explains the low flow rates observed across its surfaces. The extremely low flow rates revealed by the computations across this construct raise important concerns regarding the delivery of nutrients and the removal of waste products via convective effects in that region of the bioreactor. In addition, consistent with the horizontal orientation of the flow observed in **Figure 5.5a**, the fluid penetrates the top construct only through the upstream portion of the lateral surface. After flowing inside the porous material, the fluid exits randomly through one the three other surfaces.

GAG-content analysis

The design of a model for the contribution of the convective effects to the growth of cartilage in the spinner-flask bioreactor requires the knowledge of a relation between the shear stresses on the surface of the constructs and an indicator characterizing the growth of tissue on each scaffold. GAG, the most negatively charged cartilage component, can be easily isolated. Due to its specific binding to polyanions, safranin-O is often used to stain histological sections and provide a qualitative measurement of the presence of GAG in the tissue. The ease of use of safranin-O and the availability of reliable experimental protocols to measure GAG content suggested the implementation of such methods to analyze the tissue constructs grown in the four spinner flasks.

Methods

The constructs threaded onto the reference needle were removed from each of the four flasks after three days, ten days, four weeks and six weeks, respectively, and were cross-sectioned for histological analysis. Slices were cut in the horizontal cross section passing through the center of each scaffold and were stained with safranin-O for GAG-content analysis (**Figure 5.8**). Martin et al. (1999) have shown that the local red intensity of the stain ($\bar{R}$) can be directly related to the local GAG fraction (P_G) expressed as a percentage of the wet weight of tissue as

$$P_G = 0.04078\bar{R}, \tag{5-1}$$

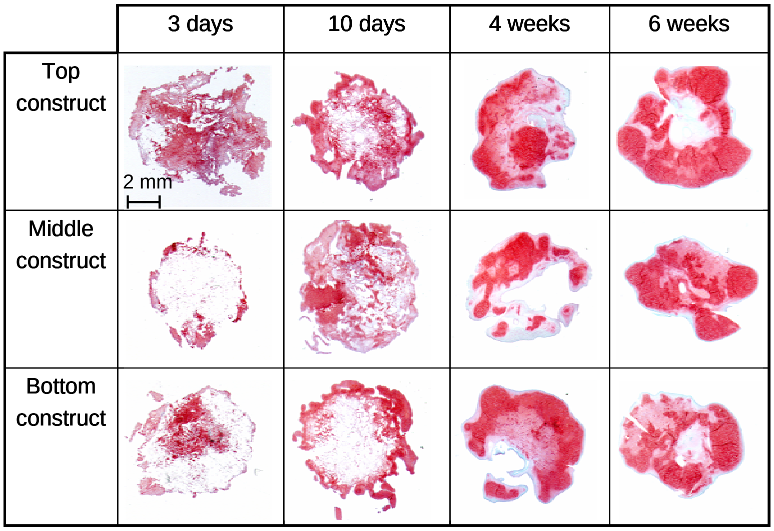

Figure 5.8: Horizontal histological slices cut in the middle cross-section of the top, middle and bottom constructs after three days, ten days, four weeks and six weeks in culture. The samples are stained for GAG with safranin-O.

with a correlation coefficient of 0.952.

Because of her experience with this technique, Dr. Bojana Obradovic (MIT) carried out the assessment of the spatial GAG-fraction distribution in each slice using the following procedure. The tissue slices were observed using a microscope and pictures were digitized in 8-bit image files of 640×480 pixels at a resolution of 47 pixels/cm. The presence of glare caused by the optical lens of the microscope was compensated for by subtracting a background image from each slice image. The resulting inverted normalized images consisted of white pixels corresponding to areas without GAG, and pixels ranging from light pink to dark red depending on the local GAG content.

The quantification of the GAG fraction in a slice was performed by a code running on the IPLab Spectrum platform according to the following procedure. A grid of 8500 square elements, each measuring 5×5 pixels (i.e., 0.106×0.106 mm), was first superimposed on the normalized image. The analysis of each square element consisted of the inspection of the number of colored pixels present in the element and the calculation of the average value of the red intensity detected on those pixels. **Equation (5-1)** was then used to deduce the average GAG fraction in each square, as a percentage of the wet weight of tissue contained in each square.

Results

Figure 5.9 shows the results of the GAG-content analysis performed on all available slices. Not surprisingly, the constructs grown for three days are relatively circular due to the initial shape of the cell-supporting scaffolds. On the middle construct, GAG is localized at the periphery of the scaffold. On the bottom construct, GAG is more concentrated inside the porous scaffold. The fact that the largest inflow was found across the surface of the bottom construct (see **Figure 5.7**) supports this observation. The presence of large GAG fractions in the bulk of the top construct is unexpected and might find an explanation in the uneven dynamic seeding of the chondrocytes on each construct prior to tissue culture. The second set of slices analyzed after ten days of growth reveal an increase in both GAG deposition/synthesis (i.e., related to the number of colored pixels) and GAG content (i.e., related to the brightness of the colored pixels) in the three scaffolds. In fact, the perimeters of the bottom and top constructs are thicker and more GAG seems to have migrated into the middle construct than observed with the three-day samples. The

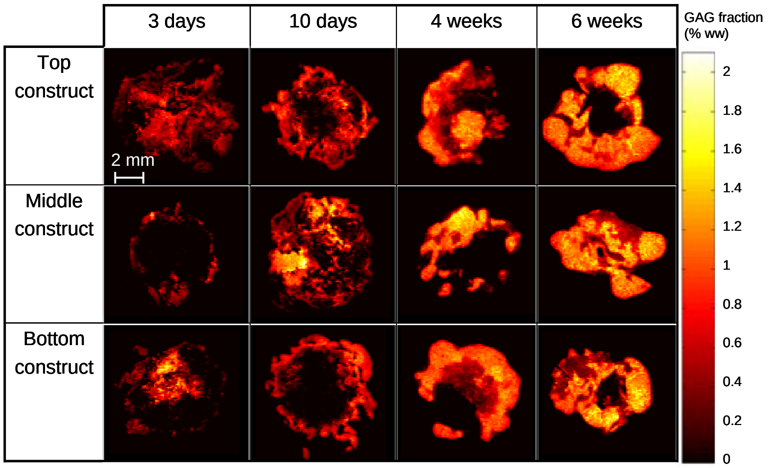

Figure 5.9: Distribution of the local GAG fraction (in % wet weight of tissue) measured in each sample.

shapes of the scaffolds are still fairly circular, suggesting that the degradation of the PGA material has not started yet. After four weeks of culture, the tissue constructs are less homogeneous in shape due to the resorption of the scaffolds and, hypothetically, the long-term effects of the periodic shear stresses on their surfaces. The increased content in GAG inside the constructs makes the localization of the initial construct position more challenging. Finally, the shapes of the scaffolds after six weeks of growth are significantly different from those observed after four weeks. The bottom and middle constructs look smaller whereas the top construct is larger. In contrast, the GAG fraction seems to increase significantly with respect to that observed on the bottom, middle and top slices after four weeks, suggesting the existence of mechanisms such as convective GAG deposition on the construct surfaces, GAG diffusion into the constructs or GAG synthesis by the chondrocytes.

Those observations motivated the investigation of the time variations of the total GAG content in each slice along the tissue-culture process. The total GAG content in a slice, P_{Gtot}, could be determined based on the local information stored for each square element as

$$P_{Gtot} = \frac{0.04078 \sum_{i=1}^{8500} \bar{R}_i px_i}{\sum_{i=1}^{8500} px_i}, \tag{5-2}$$

where $\bar{R}_i$ is the average red intensity and px_i is the number of colored pixels in the square element i. The results shown in **Figure 5.10** demonstrate that the GAG content of each construct continuously increases as a function of time and support the observations made earlier. Quantitatively, the GAG fractions measured at a given time during the culture are relatively similar in the three constructs. At the end of the culture process, the GAG content measured in the constructs ranges from 0.68 to 0.82% of the wet weight of the tissue. This value is significantly

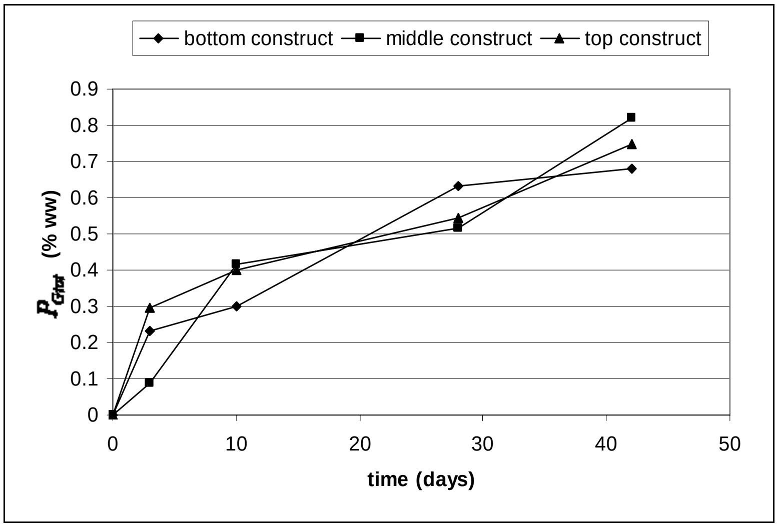

Figure 5.10: GAG content (in % wet weight of tissue) measured in the bottom, middle and top construct as a function of culture time.

inferior to the GAG fractions found by Martin et al. (1999) in constructs grown within a static spinner flask ($P_{Gtot} = 3.3$), a mixed spinner flask ($P_{Gtot} = 2.9$), and a rotating-wall bioreactor ($P_{Gtot} = 5.4$).

GAG -shear stress correlation

Global correlation

Two different methods were implemented in order to produce a correlation between GAG fraction and wall-shear stress. The first one consisted of inspecting the entire surface of each slice for GAG content and using the CFD model to retrieve the mean wall-shear stress obtained on the surface of the scaffold specific to that particular slice (i.e., bottom, middle or top construct). Because the GAG fraction was calculated with respect to the entire slice, this technique resulted in a global correlation between GAG content and wall-shear stress. Different options can be considered to calculate the average wall-shear stress on the surface of a construct. A first option consists of averaging the wall-shear stress values predicted by the CFD model

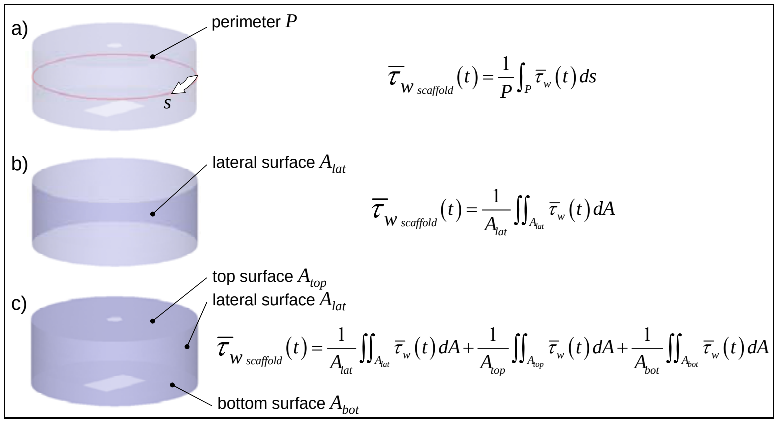

Figure 5.11: Description of the three averaging methods for the production of the wall-shear stress estimate: a) average over the perimeter of the scaffold located in the cross-section of the histological slice; b) average over the lateral surface of the scaffold; and c) average over the lateral, bottom and top surfaces of the scaffold.

along the perimeter of the cylindrical scaffold included in the plane from which the slice was cut (**Figure 5.11a**). A second option consists of averaging the wall-shear stress values obtained on the lateral surface of the scaffold (**Figure 5.11b**). Finally, a last option is to average the wall-shear stress over the entire surface of the cylindrical scaffold (i.e., top, bottom and lateral surfaces) as shown in **Figure 5.11c**. Because the turbulent flow encountered in the spinner flask is periodic, the time-dependent wall-shear stresses yielded by each method also had to be averaged over one revolution of the stir bar in order to produce one unique wall-shear stress estimate. The results of those calculations are shown in **Table 5-2**, where the shear stresses are relative to the prototype bioreactor used during the tissue-growth experiments. The wall-shear stress estimates found by averaging over the whole construct surface and over the lateral surface only do not display any significant difference. On the other hand, the values found by averaging over the perimeter of the construct contained in the section of the slice are systematically twice as large as those obtained using the two other averaging methods. The small number of vertices produced by the mesh along the perimeter could explain this difference and raises an issue on the relevance of this average shear-stress estimate. In addition, since the tissue slices do not carry any

Table 5-2: Wall-shear stress predicted by FLUENT on the bottom, middle and top constructs using three averaging methods (values are for the prototype bioreactor and units are N/m^2).

Averaging method	$\overline{\tau}_{w}$ bottom construct	$\overline{\tau}_{w}$ middle construct	$\overline{\tau}_{w}$ top construct
perimeter	0.08048	0.06003	0.04984
lateral surface	0.04094	0.03210	0.02693
whole surface	0.04085	0.03567	0.03098

information about the growth on the top and bottom surfaces of the constructs, averaging over the whole construct surface was discarded. For those reasons, averaging over the lateral scaffold surface was chosen as an appropriate method to produce a reliable wall-shear stress estimate.

Figure 5.12 shows the variations of GAG content as a function of average wall-shear stress at each culture time (i.e., three days, ten days, four weeks and six weeks). The average wall-shear stress calculated on the perfectly circular lateral surface (i.e., initial construct shape prior to tissue growth) of the bottom, middle and top constructs was assumed constant all along the culture despite the associated variations in construct shape. The dependence of the GAG content on the construct wall-shear stress is not obvious. Different trends can be observed at each culture time. The random character of this result invites some comments. One of the issues raised by this global analysis is the narrow range of shear stresses (i.e., from 0.269 to 0.409 dyn/cm^2) used to build the correlation. Since the global analysis relies on one wall-shear stress estimate per construct, only three data points (i.e., for the bottom, middle and top constructs) are available to produce a correlation at each culture time. New tissue-growth experiments using spinner flasks operating under similar dynamic conditions but with different construct vertical positions could provide additional GAG-content measurements and new wall-shear stress values. In addition, the assumption of constant wall-shear stress on a given construct all along the growth process might be simplistic, making the trends observed after long culture times (i.e., 10 six weeks, four weeks and, possibly, ten days) inaccurate. This issue could be overcome by modifying the three-dimensional geometry of the constructs in the CFD model at a given culture time. Finally, another

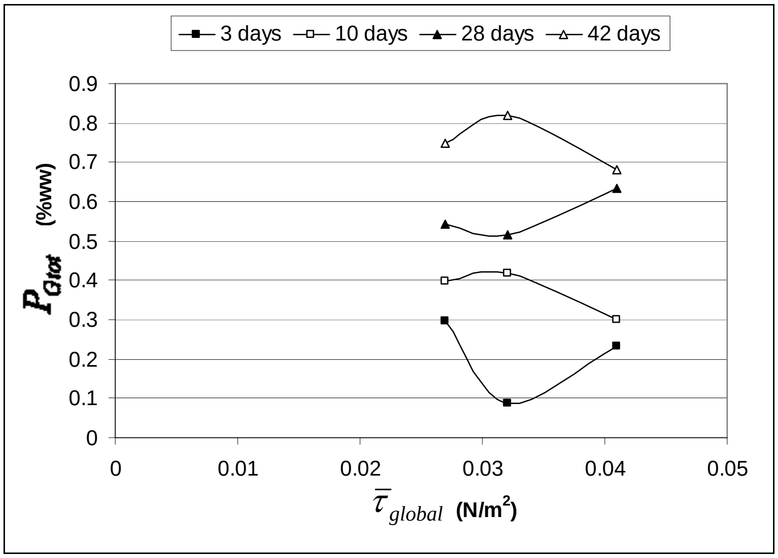

Figure 5.12: Global correlation between the average wall-shear stress computed over the lateral surface of each construct and the global GAG fraction measured in each slice at 3, 10, 28 and 42 days.

issue raised by analyzing the GAG content *globally* is the loss of information regarding the mechanism stimulating tissue growth. In fact, since it calculates the GAG fraction in the whole slice, the global analysis is not capable of dissociating the amount of GAG deposited via convection at the surface of the scaffold from that obtained via diffusion inside the porous material. Therefore, it might not be possible to isolate a correlation between global GAG content and wall-shear stress.

Local correlation

A different method was proposed to correlate *locally* GAG fraction and wall-shear stress. The description of this procedure is depicted in **Figure 5.13**. On each slice, the initial position of the scaffold was identified and a reference point was isolated to determine the angular orientation of the construct in the bioreactor. The location of this reference point was defined as the intersection between the initial scaffold perimeter and the V-shaped crack indicating the tissue part closest to the flask center (**Figure 5.13a**). The scaffold perimeter was then discretized into 20

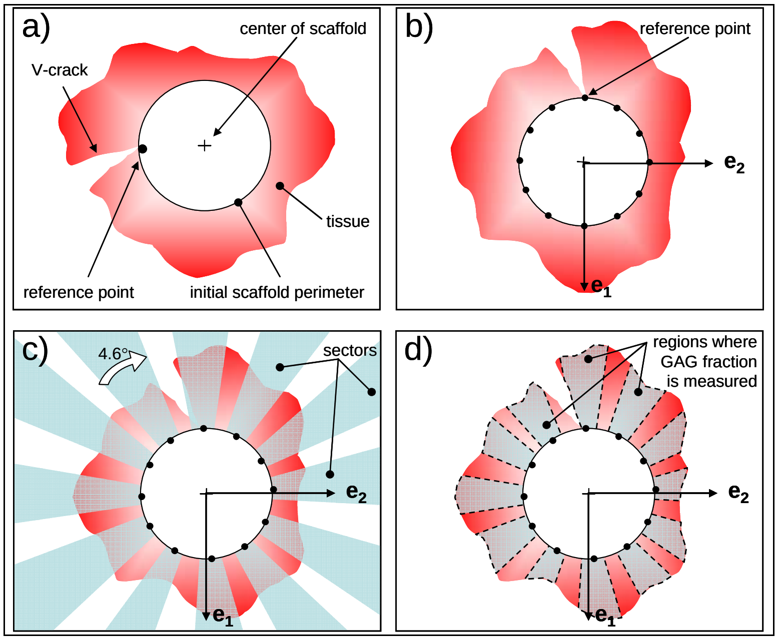

Figure 5.13: Implementation of the local correlation: a) the initial scaffold position and the reference point are identified; b) the scaffold perimeter is discretized into 20 points; c) angular sectors centered on the perimeter points are created; d) local GAG fraction is measured in the tissue region outside the scaffold and contained within a sector.

equi-angularly spaced points separated by an angle $\theta = 18°$ (**Figure 5.13b**). For each perimeter point, an angular sector whose origin is the center of the initial scaffold position and bisector passes through the perimeter point was created (**Figure 5.13c**). The angle of the sector (i.e., 4.6°) was chosen such that the size of the perimeter part contained within a sector was similar to that of a mesh element on the construct surface in the CFD model (i.e., 0.2 mm). This detail was motivated by the effort to compare shear-stress data and GAG-content information over regions sharing similar scales. Finally, at each point created on the construct perimeter, the wall-shear stress predictions were obtained from the CFD model at each time step and were averaged over one period to produce a unique wall-shear stress estimate at that point. The GAG fraction relative to the same point was calculated in the part of the tissue falling in the associated sector and located outside the region initially occupied by the scaffold (**Figure 5.13d**).

Compared with the global analysis described earlier, the local procedure presents some advantages. Because it is based on the measurement of the GAG fraction outside the porous material, this method permits the direct assessment of tissue growth via convective effects. Diffusion that occurs inside the scaffold is not considered. In addition, since the choice of the discretization angle on the scaffold perimeter (i.e., $\theta = 18°$ in the present analysis) is arbitrary, the number of available points to achieve the correlation is not limited. Although 20 points on the construct perimeter were found to be a good compromise between sample size, shear-stress range and computation time, more points could be possibly used.

On the other hand, the implementation of this new analysis raises additional issues. Because of the difficulty to report the changes undergone by the scaffold shape during growth in the CFD geometry, the local analysis is also based on the assumption that the time-averaged shear stress predicted at a perimeter point on the perfectly cylindrical construct shape does not depend on the culture time, i.e., that the changing shape of the construct does not significantly impact the flow. Lappa (2003) proposed an organic tissue-growth volume-of-fraction method in order to predict the change of shape of a single cartilage construct exposed to a laminar flow within a rotating-wall vessel. Although this method successfully predicted the shape of a six-week construct, its implementation in the spinner-flask environment would be difficult. In fact, because each construct affects the entire flow field in the spinner flask, a processor-consuming model updating the shape of each construct at each time step would have to be used. In addition, the predictive growth model has not been proved to be reliable in a turbulent-flow environment.

More importantly, the necessity to find the initial construct position and the location of the reference point indicating the orientation of the construct in the flow was an important concern. As shown in **Figure 5.8**, if the features of the initial porous scaffold can be observed in the center of the slices obtained after three days and ten days, they are much less obvious and even undetectable in slices obtained at a later time. Conversely, if the V-shaped crack and, therefore, the reference point, can be fairly identified on slices observed late in the growth, they cannot be isolated without uncertainty in slices grown at an earlier stage because of the discontinuity or limited presence of tissue on the construct perimeter.

This issue restricted the implementation of the local analysis on the slice obtained in the cross section of the bottom construct after ten days of culture, i.e., the only slice providing enough information for the localization of the initial scaffold position and the reference point (**Figure 5.14**). Although this limitation limited the number of available data point to achieve the correlation, it relaxed the issue raised by the dependence of the shear-stress environment on the construct shape since the data were all collected at the same instant of time (i.e., ten days).

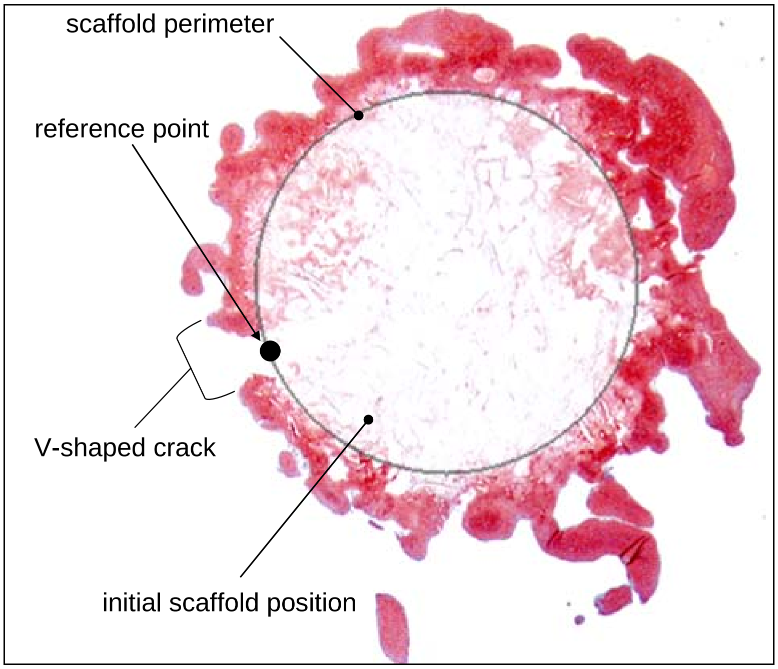

Figure 5.14: Tissue slice extracted from the middle cross-section of the bottom construct after ten days of culture and used for the production of the local correlation. The initial scaffold position and the reference point are indicated.

The GAG content measured on the periphery of the construct was correlated to the shear-stress predictions provided by the CFD model following the procedure described earlier and the results are plotted in **Figure 5.15**. The data obtained at the reference point were not considered because of the presence in its vicinity of the V-shaped crack preventing a reliable measurement of the GAG content in the associated sector. The GAG fractions measured in the sectors were found to be between 0 and 0.8% of the tissue wet weight found within the same sectors while the time-averaged wall-shear stress values computed at the 20 perimeter points ranged from 0.082 to 1.1 dyn/cm^2 (prototype values). The general trend of the graph suggests a GAG fraction increasing with wall-shear stress over this specific range. Shown as a solid line in **Figure 5.15** is the power-law data fit

$$P_{Gloc} = 1.3636 \times \overline{\tau}_{local}{}^{0.3324}, \qquad (5\text{-}3)$$

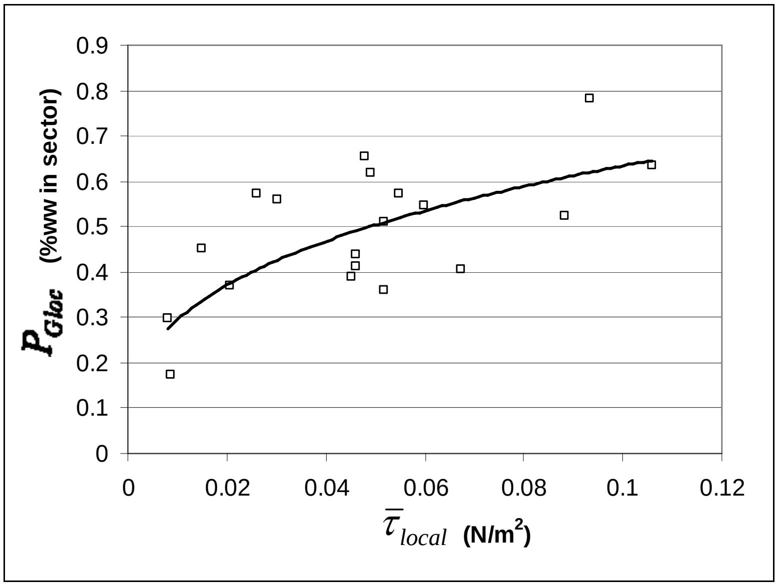

Figure 5.15: Variations of the local GAG fraction measured in a sector as a function of the wall-shear stress predicted at a scaffold perimeter point. A power law (indicated by a solid line) was found to be the best fit to the data.

which provided the data with the best possible fit. However, due to the low value of the correlation coefficient ($R^2 = 0.5053$), this relation could not be exploited with confidence for the prediction of GAG fractions, especially for shear stress values falling outside the interval considered in this study. Nevertheless, the trend observed on this correlation attempt is supported by the results obtained by Saini and Wick (2003) already commented in Chapter 1. In fact, although they were grown in a different type of device, the constructs grown in the concentric-cylinder bioreactor after 12 days in culture exhibited increasing GAG contents with increasing angular velocities (and, therefore, shear stresses) (see **Figure 1.9c**).

Different hypotheses can be developed to explain the lack of correlation between the shear-stress and GAG data. Although the range of shear-stress magnitudes on which the local correlation was based (i.e., 0.082 to 1.1 dyn/cm^2) is broader than that used to describe the variations of the global GAG content (i.e., 0.269 to 0.409 dyn/cm^2), it is still too narrow to permit the generalization of the trend observed on the graph of **Figure 5.15**. In fact, this range only corresponds to one particular shear-stress environment present in the vicinity of the bottom construct at a specific time (ten days in the present correlation). Although more data could be obtained by discretizing the construct perimeter into more points, it would be preferable and more statistically significant to use data collected from different constructs (i.e., top and middle constructs grown in the same bioreactor, or bottom construct grown in a different bioreactor operating under the same conditions). In addition, more data could have been analyzed if the difficulties raised by the precise localization of the scaffold perimeter and the reference point could have been lifted. One strategy to solve this issue would consist of using a different construct architecture allowing for the non-arbitrary determination of the initial scaffold position. The composite construct shown in **Figure 5.16** is made of a cylindrical solid core (e.g., polymer) with a diameter of about 3 mm partially cut on one side in the direction of its height and covered by a thin (i.e., 1-mm thick) layer of porous biodegradable material such as PGA. This particular

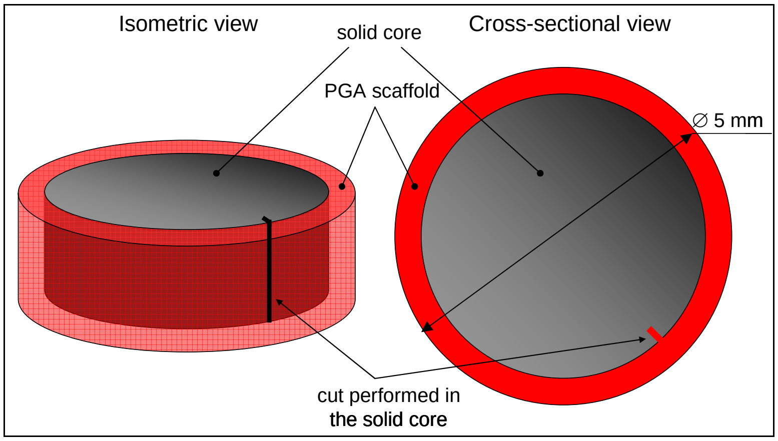

Figure 5.16: Description of the new scaffold architecture envisioned for the successful implementation of the local correlation. The scaffold made of a solid core is covered by a thin layer of biodegradable porous material.

architecture would be more appropriate than the common PGA scaffolds to study the effects of convective mechanisms on tissue growth and to provide an estimate of the initial time rate of change of local GAG content on the construct perimeter. Since the solid core does not degrade over time, it would be intact and clearly visible in histological tissue cross-sections. The location of the cut would provide information about the orientation of the construct within the bioreactor. In addition, the PGA layer would allow for the seeding of chondrocytes, and the synthesis and deposition of GAG, at least for a short culture time (dependent on the thickness of the porous layer).

Finally, another reason that prevented the production of a reliable correlation is the quality of the tissue constructs obtained during the culture. As mentioned earlier, the global GAG fraction measured on each slice revealed a very low GAG content, more than 20 times lower than the content usually observed in mixed cultures (e.g., spinner flasks and rotating-wall vessels) operating under mixing of similar intensity, and more than 40 times lower than that measured in native cartilage.

Discussion

The final step of this research consisted of the implementation of tissue-growth experiments in the prototype spinner-flask bioreactor described in Chapter 1 and the prediction of the shear-stress environment in a dynamically-similar three-dimensional CFD model. Four bioreactors operating under similar conditions were used to provide four sets of constructs (each consisting of the bottom, middle and top constructs threaded onto the reference needle) grown for periods of three days, ten days, four weeks and six weeks, respectively. Histological construct cross-sections were stained with safranin-O and inspected for GAG content using an image-processing technique. The GAG content in each construct (i.e., bottom, middle and top) was shown to increase continuously as a function of culture time. The relation between GAG content and wall-shear stress that this study aimed at producing was investigated in two different ways. First, a global correlation was attempted between the global GAG content in each construct and the average value of the shear stress predicted on the surface of each construct over one period. Then, a local correlation was sought between the local wall-shear stress computed at a point on the construct perimeter and the GAG content measured in the tissue part falling in a sector outside the scaffold and extending from the perimeter point toward the flow. The global analysis did not provide any relevant information due to the small number of data points (one construct generated one shear stress magnitude and only three constructs were threaded on the reference needle). The local correlation revealed increasing GAG contents with increasing wall-shear stresses. However, the large number of tissue slices that had to be discarded (i.e., 11 out of 12) for the reliable implementation of this correlation prevented the production of statistically significant results and of a numerical relation between local GAG content and local wall-shear stress. Finally, a new construct architecture was proposed in order to lift those difficulties.

CHAPTER 6

DISCUSSION AND CONCLUSIONS

Summary

This thesis focused on the development of a tissue-growth model for cartilage in a spinner-flask bioreactor. This model based on a relation derived from the correlation between local GAG-fraction measurements and local shear-stress estimates on construct surfaces required the development of experimental and computational tools aiming at the characterization and prediction of the flow in the spinner flask. An experimental two-dimensional particle-image velocimetry (PIV) setup was built for the study of turbulent periodic flows of the type produced in the spinner flask. Flexible and user-friendly PIV software was designed to achieve the cross-correlation and to produce the turbulent-flow characteristics (i.e., mean velocity, mean-shear stress, Reynolds stress and turbulent kinetic energy). The resulting setup was exploited to inspect the complex flow in a model spinner flask operating under dynamic conditions suitable for tissue growth. Finally, the PIV setup was validated in terms of its ability to produce data satisfying continuity (i.e., mass conservation).

The availability of flow measurements permitted the design of a computational-fluid-dynamics model using FLUENT. The three-dimensional geometry of the model bioreactor inspected experimentally was successfully generated using advanced features such as the sliding mesh option necessary to simulate the rotation of the stirring element in the flask. The resulting model based on the realizable $k-\varepsilon$ model was implemented in the model bioreactor geometry. The computational results were compared with the PIV measurements and the fair agreement between those resulted in the validation of the CFD model. In an effort to collect information more relevant for tissue growth, the model was exercised in a similar flask geometry containing porous instead of solid scaffolds. The features of the flow present in the porous material were predicted using the Darcy law but were not validated due to the absence of similar measurements.

Tissue-growth experiments were carried out by our collaborators at MIT, Drs. Gordana Vunjak-Novakovic, Lisa Freed and Bojana Obradovic. An experimental protocol was proposed to allow for the production of cartilage constructs whose geometry, position and orientation in the flow were perfectly determined so that flow features could be readily obtained via the use of the CFD model. The culture was started in a flask similar to the prototype in which flow predictions were performed. Histological tissue cross sections were harvested after three days, ten days, four weeks and six weeks and analyzed for GAG content using an image-processing code. The local GAG data provided by our collaborators were used to attempt to determine a relation between local GAG content and local shear-stress magnitude. Global and local correlations based on global and local GAG measurements and shear-stress predictions were proposed but processing difficulties due to the loss of information on construct position and orientation prevented the production of a reliable CFD-based tissue-growth model.

Benefits

Although the present thesis did not attain all its intended goals, it provided a variety of tools and methods from which future studies would benefit. First, a set of routines has been developed to permit the processing of single-exposure double frame digital PIV images captured in a turbulent periodic flow. The integration of those MATLAB programs in a graphic-user interface makes “DoctorPIV plus” a powerful instrument for the analysis of PIV data captured in a wide range of flows. The special wall-treatment that limits uncertainty in velocity measurements near solid boundaries is an additional improvement with respect to commercially available codes. This feature could be exploited in applications focusing on the estimation of velocity gradients (and, therefore, shear stresses) near solid edges. The realizable $k-\varepsilon$ model whose specific strength is in the modeling of swirling flows was shown to be well adapted for the prediction of the flow produced in the spinner-flask bioreactor. The advanced moving-mesh feature offered by FLUENT along with the tools provided by GAMBIT led to the successful design of a three-dimensional geometry mimicking the architecture and operating mode of a spinner flask configured for tissue culture. This thesis provided tools that could be used in the future for the experimental investigation and computational modeling of the flow produced in more complex tissue-growth environments (e.g., wavy-walled bioreactor; Barabino et al., 1993).

In addition, this thesis constitutes a first attempt to assess the convective effects of the flow environment on the growth of tissue constructs reflected by a correlation between local shear stress predictions and local GAG measurements. An experimental tissue-growth protocol was successfully designed and implemented to provide time-dependent GAG measurements in constructs cultivated in four flasks. GAG content was assessed through the implementation of the image-processing technique whose reliability had been demonstrated by Martin et al. (1999). The failure to obtain a correlation between GAG and wall-shear stress is not believed to be caused by the inaccuracy of the hypothesis formed at the beginning of this study, i.e., “the production of a functional tissue with the desired properties requires the detailed knowledge of the relationship between the production of critical cartilage structural components (mainly, GAG and type-II collagen) and shear stress”. Instead, the inability to produce cartilage constructs with GAG contents similar to those usually observed *in vitro* and the failure to effectively mark the position and orientation of standard PGA scaffolds during the culture are issues that should be corrected to produce the intended correlation.

Improvements and future work

The work presented in this thesis could benefit from a number of improvements. First, the accuracy and reliability of the PIV setup could be addressed. The optical lenses used in the current setup are capable of producing a 1-mm thick laser sheet. Since the measurement of the velocity and, more specifically, of the velocity gradients in the vicinity of the constructs is of interest in this research, it is critical to eliminate cross-correlation noise produced by the displacement of tracer particles located at different depths in the laser sheet. This noise could be attenuated by producing a thinner laser sheet, permitting a better alignment of the observed particles with the flow field of interest. However, because the use of a thinner laser sheet would result in an increased number of particles leaving the sheet between the two images captured at each double-pulse of the laser, a trade-off would have to be made and the resulting error on the cross-correlation would have to be quantified.

The reasons for the observed discrepancy between the mean velocity magnitudes measured experimentally and predicted by the CFD model should be investigated further. The realizable $k-\varepsilon$ model was implemented in the spinner-flask geometry using the standard constants described by Shih et al. (1995). The role and influence of each model parameter on the prediction of the flow field could be addressed in order to produce a better agreement with the laboratory measurements.

As suggested earlier, the correlation between the local wall-shear stress and local GAG content could be improved significantly by using the new construct design described in the previous section. Although this composite scaffold would permit the localization of the construct in the bioreactor, the presence of a solid core and thus wall effects could impact adversely the prediction of tissue growth due to convective effects in the porous medium. In addition, the local correlation could be performed on a construct placed in a simple, well-characterized flow (e.g., plane Poiseuille flow) permitting better control of the shear-stress environment.

Finally, as intended originally, the convective tissue-growth model could be coupled with the diffusive model designed by Obradovic (2000). The resulting predictive tool would permit the investigation of new operating conditions, bioreactor geometries and scaffold architectures aimed at improving the growth of tissue *in vitro*.

APPENDIX A

UNCERTAINTY IN REYNOLDS NUMBER CALCULATION

In the spinner flask, the Reynolds number was calculated as

$$\mathrm{Re} = \frac{L^2 \omega}{\nu}, \tag{A-1}$$

where L is the length of the stir bar, ω is the angular velocity of the stir bar, and ν is the kinematic viscosity of the working fluid. The rotation speed of the impeller was measured by a MONARCH tachometer (model ACT-1) mounted on the base of the bioreactor. This device displayed the angular velocity in revolutions per minute with an uncertainty w_ω of ± 0.5 rpm. The kinematic viscosity was measured by a viscometer (COLE-PARMER, size 50) as

$$\nu = \alpha \Delta t, \tag{A-2}$$

where Δt is the time required by the fluid to flow through the viscometer, and α is a temperature-dependent factor. Δt was measured by a timer with an uncertainty $w_{\Delta t}$ of ± 0.5 s. Substituting (A-2) into (A-1) yields

$$\mathrm{Re} = \frac{L^2 \omega}{\alpha \Delta t}. \tag{A-3}$$

Kline and McClintock (1953) showed that the uncertainty of the resulting Reynolds number could be calculated as

$$w_{\mathrm{Re}} = \left[\left(\frac{\partial \mathrm{Re}}{\partial \Delta t} w_{\Delta t} \right)^2 + \left(\frac{\partial \mathrm{Re}}{\partial \omega} w_{\omega} \right)^2 \right]^{\frac{1}{2}} . \tag{A-4}$$

Substituting the partial derivatives of Re with respect to the two dependent variables Δt and ω yield

$$w_{\mathrm{Re}} = \left[\left(\frac{-L^2 \omega}{\alpha \Delta t^2} w_{\Delta t} \right)^2 + \left(\frac{L^2}{\alpha \Delta t} w_{\omega} \right)^2 \right]^{\frac{1}{2}} . \tag{A-5}$$

Averaging the measurements over five realizations resulted in $\alpha = 3.813 \times 10^{-3}$ mm^2/s^2 and $\Delta t = 422$ s. Given a stir-bar length of 7.24 cm and an angular velocity of 32.38 rpm, the uncertainty in the calculation of the Reynolds number could be calculated as $w_{\mathrm{Re}} = \pm 27$.

APPENDIX B

PARTICLE SEDIMENTATION VELOCITY

The sedimentation velocity of the tracer particles used in the PIV measurements could be calculated with the Stokes' law as

$$U_{St} = \frac{2{a_p}^2\left(\rho_p - \rho_f\right)}{9\mu} g_r, \tag{B-1}$$

where a_p is the radius of the spherical particle, ρ_p is the mass density of a particle, ρ_f is the mass density of the fluid, μ is the dynamic viscosity of the fluid, and g_r is the acceleration of gravity. The particles used in the experiments had a diameter of 11 μm and a density of 2.54 g/cm^3. The density of the working fluid was 1901.5 kg/m^3 and its viscosity was 3.06×10^{-3} kg.m^{-1}.s^{-1}. Given a gravity constant of 9.81 m/s^2, the sedimentation velocity of the particles was found to be 13.8 μm/s.

APPENDIX C

UNCERTAINTY IN PERMEABILITY MEASUREMENT

The Darcy law written in **Equation (4-11)** can be written as a function of Q, the flow rate of fluid passing through the porous medium:

$$\alpha = \frac{\mu Q}{A \nabla P}, \tag{C-1}$$

where A is the area of the porous medium cross-section whose normal is parallel to the principal flow direction. Therefore, the uncertainty in the measurement of the permeability is related to both, uncertainties in the measurement of the flow rate and uncertainties in the estimation of the pressure gradient across the porous medium. The relation allowing the estimation of this value can be expressed as

$$w_{\alpha} = \left[\left(\left(\frac{\partial \alpha}{\partial Q} \right) w_{Q} \right)^{2} + \left(\left(\frac{\partial \alpha}{\partial \nabla P} \right) w_{\nabla P} \right)^{2} \right]^{\frac{1}{2}}, \tag{C-2}$$

where w_{α}, w_{Q} and $w_{\nabla P}$ are uncertainties relative to the estimation of the permeability, flow rate and pressure gradient, respectively. Since the uncertainty in permeability measurement is a function of the flow rate and the pressure gradient, the following calculation was made for one set of those parameters.

The flow rate was calculated as the time Δt for a certain volume V of fluid to flow through the construct:

$$Q = \frac{V}{\Delta t}. \tag{C-3}$$

The uncertainty in the measurement of Q is correlated to the uncertainty for measuring the time Δt as

$$w_Q = \left[\left(\left(\frac{\partial Q}{\partial \Delta t} \right) w_{\Delta t} \right)^2 \right]^{\frac{1}{2}}, \tag{C-4}$$

where w_Q and $w_{\Delta t}$ are the uncertainties relative to the estimation of the flow rate and time, respectively. The time was measured by a timer with an uncertainty $w_{\Delta t}$ of ± 0.5 s. Given a volume of liquid $V = 20$ ml and a time $\Delta t = 7.9$ s, the uncertainty in flow rate estimation was calculated as $w_Q = 1.6 \times 10^{-7}$ m^3/s.

The pressure gradient was calculated based on the successive application of the Bernoulli equation between different points in the permeability device. Its expression was given in **Equation 4-12**. The uncertainty in the estimation of this quantity depends on the measurement of the flow rate as

$$w_{\nabla P} = \left[\left(\left(\frac{\partial \nabla P}{\partial Q} \right) w_Q \right)^2 \right]^{\frac{1}{2}}, \tag{C-5}$$

where $w_{\nabla P}$ and w_Q are the uncertainties relative to the estimation of the pressure gradient and flow rate, respectively. Given a flow rate $Q = 2.53 \times 10^{-6}$ m^3/s, the uncertainty in pressure gradient was evaluated as $w_{\nabla P} = 20395$ N/m^3.

Substituting (C-4) and (C-5) into (C-2) and expanding the partial derivatives yields:

$$w_\alpha = \left[\left(\frac{\mu}{A \nabla P} w_Q \right)^2 + \left(\frac{\mu Q}{A (\nabla P)^2} w_{\nabla P} \right)^2 \right]^{\frac{1}{2}}. \tag{C-6}$$

Therefore, given a construct cross-sectional area $A = 0.79$ cm^2, the permeability measurement relative to the case $Q = 2.53 \times 10^{-6}$ m^3/s and $\nabla P = -4.16 \times 10^5$ N/m^3 could be estimated as $\alpha = 6.98 \times 10^{-11} \pm 5.59 \times 10^{-12}$ m^2.

REFERENCES

Adrian RJ. 1991. Particle-imaging techniques for experimental fluid mechanics. Annual Review of Fluid Mechanics 23:261-304.

Agrawal CM, McKinney JS, Lanctot D, Athanasiou KA. 2000. Effects of fluid flow on the in vitro degradation kinetics of biodegradable scaffolds for tissue engineering. Biomaterials 21:2443-2452.

Agrawal CM, Ray RB. 2001. Biodegradable polymeric scaffolds for musculoskeletal tissue engineering. Journal of Biomedical Materials Research 55(2):141-150.

Aigner T, McKenna L. 2002. Molecular pathology and pathobiology of osteoarthritic cartilage. Cellular and molecular life sciences 59:5-18.

Barabino GA, Metghalchi M, Zhang B. Mammalian Cell Culture in a Novel Bioreactor; 1993. ASME-BED The Bioengineering Division. p 1-4.

Begley CM, Kleis SJ. 2000. The fluid dynamic and shear environment in the NASA/JSC rotating-wall perfused-vessel bioreactor. Biotechnology and Bioengineering 70:32-40.

Bernal L. 1996. MATLAB programs for particle-image velocimetry. University of Michigan.

Bradshaw P. 1971. An introduction to turbulence and its measurement. Pergamon Press. p 9.

Brown JB. 1998. An experimental facility for the investigation of the flow in a circular-Couette flow bioreactor [MS]. Atlanta, GA: Georgia Institute of Technology.

Cherry RS, Papoutsakis ET. 1988. Physical mechanisms of cell damage in microcarrier cell bioreactors. Biotechnology and Bioengineering 32:1001-1014.

Croughan MS, Hamel JF, Wang DIC. 1987. Hydrodynamic effects on animal cells grown in microcarrier cultures. Biotechnology and Bioengineering 29:130-141.

Cuckler JM. 1997. Surgical treatment of knee arthritis. In: Koopman WJ, editor. Arthritis and allied conditions. Philadelphia: Lippincott Williams and Wilkins. p 949-958.

Feder J, Tolbert WR. 1983. The large-scale cultivation of mammalian cells. Scientific American 248:34-43.

Freed LE, Langer R, Martin I, Pellis NR, Vunjak-Novakovic G. 1997. Tissue engineering of cartilage in space. Proceedings of the National Academy of Sciences 94:13885-13890.

Freed LE, Vunjak-Novakovic G. 1995. Cultivation of cell-polymer tissue constructs in simulated microgravity. Biotechnology and Bioengineering 46:306.

Gooch KJ, Kwon JH, Blunk T, Langer R, Freed LE, Vunjak-Novakovic G. 2001. Effects of mixing intensity on tissue-engineered cartilage. Biotechnology and Bioengineering 72:402-407.

Grande DA, Halberstadt C, Naughton G, Schwartz R, Manji R. 1997. Evaluation of matrix scaffolds for tissue engineering of articular cartilage grafts. Journal of Biomedical Materials Research 34:211-220.

Hauselmann HJ, Flura T, Marti C, Hauser N, Hedbom E. 1998. From chondrocyte culture to joint cartilage replacement. Development of de novo cartilage in vitro. Schweizerische Medizinische Wochenschrift 128:824-832.

Hendricks R, Aviram A. 1982. Use of zinc iodide solutions in flow research. Review of Scientific Instruments 53:75-78.

Jackson DW, Scheer MJ, Simon TM. 2001. Cartilage substitutes: overview of basic science and treatment options. Journal of American Academy of Orthopaedic Surgeons 9:37-52.

Keane RD, Adrian RJ. 1992. Theory of cross-correlation analysis of PIV images. Journal of Applied Scientific Research 49:191-215.

Kline J, McClintock FA. 1953. Describing uncertainties in single-sample experiments. Mechanical Engineering 75:3-8.

Langer R, Vacanti JP. 1993. Tissue engineering. Science 260(May 14):920-926.

Lappa M. 2003. Organic tissues in rotating bioreactors: fluid-mechanical aspects, dynamic growth model, and morphological evolution. Biotechnology and Bioengineering 84(5):518-532.

Launder BE, Spalding DB. 1972. Lectures in mathematical models of turbulence. London: Academic Press.

Lawrence RC, Helmick CG, Arnett FC. 1998. Estimates of the prevalence of arthritis and selected musculoskeletal disorders in the United States. Arthritis and Rheumatism 43:778-799.

Maroudas A. 1976. Balance between swelling pressure and collagen tension in normal and degenerate cartilage. Nature 260:808-809.

Maroudas A, Venn M. 1977. Chemical composition and swelling of normal and osteoarthritic femoral head cartilage. Annals or Rheumatic Diseases 36:399-406.

Martin I, Obradovic B, Freed LE, Vunjak-Novakovic G. 1999. Method for quantitative analysis of glycosaminoglycan distribution in cultured natural and engineered cartilage. Annals of Biomedical Engineering 27:656-662.

Mow VC, Ratcliffe A, Rosnwasser MP, Buckwalter JA. 1991. Experimental studies on repair of large osteochondral defects at a high weight bearing area of the knee joint: a tissue engineering study. Journal of Biomechanical Engineering - Transactions of ASME 113:198-207.

Muir H. 1995. The chondrocytes, architect of cartilage. BioEssays 17:1039-1048.

Muir H, Bullough P, Maroudas A. 1970. The distribution of collagen in human articular cartilage with some of its physiological implications. Journal of Bone Joint Surgery 52:554-563.

Nagata S. 1975. Mixing - Principles and applications. Mixing - Principles and applications. New-York: John Wiley and Sons. p 10, 124-138, 446.

Neitzel GP, Nerem RM, Sambanis A, Smith MK, Wick TM, Brown JB, Hunter C, Jovanovic I, Malaviya P, Saini S and others. 1998. Cell function and tissue growth in bioreactors: fluid-mechanical and chemical environments. Journal of the Japanese Society of Microgravity Applications 15:602.

Nerem RM, Sambanis A. 1995. Tissue engineering: from biology to biological substitutes. Tissue Engineering 1: 3–13.

Obradovic B, Meldon JH, Freed LE, Vunjak-Novakovic G. 2000. Glycosaminoglycan deposition in engineered cartilage: experiments and mathematical model. AIChE Journal 46:1860-1871.

Ogston AG. 1970. The biological functions of glycosaminoglycans. In: Andre AB, editor. Chemistry and molecular biology of the intracellular matrix. London: Academic Press. p 1231-1240.

Osorio DF. 2001. Numerical simulation of the fluid mechanics of a spinner-flask bioreactor [MS]. Atlanta, GA: Georgia Institute of Technology. 122 p.

Pope SB. 2000. Turbulent viscosity models. Turbulent flows: Cambridge University Press. p 358-386.

Praemer A, Furner S, Rice DP. 1999. Musculoskeletal conditions in the United States: Amer Academy of Orthopaedic. 182 p.

Risbud MV, Sittinger M. 2002. Tissue engineering: advances in in vitro cartilage generation. Trends in Biotechnology 20(8):351-356.

Saini S, Wick TM. 2003. Concentric cylinder bioreactor for production of tissue engineered cartilage: effect of seeding density and hydrodynamic loading on construct development. Biotechnology Progress 19:510-521.

Shih TH, Liou WW, Shabbir A, Zhu J. 1995. A new k-ε eddy-viscosity model for high Reynolds number turbulent flows - Model development and validation. Computers and Fluids 24(3):227-238.

Tennekes H, Lumley JL. 1972. A first course in turbulence. Cambridge, MA: MIT Press. 300 p.

Unger DR, Muzzio FJ, Aunins JG, Singhvi R. 2000. Computational and experimental investigation of flow and fluid mixing in the roller bottle bioreactor. Biotechnology and Bioengineering 70(2):117-130.

Venkat RV, Stock RL, Chalmers JJ. 1996. Study of hydrodynamics in microcarrier culture spinner vessels - a particle tracking velocimetry approach. Biotechnology and Bioengineering 49:456-466.

Vunjak-Novakovic G, Freed LE, Biron RJ, Langer R. 1996. Effects of mixing on the composition and morphology of tissue engineered cartilage. American Institute of Chemical Engineering Journal 42:850-860.

Westerweel J. 1997. Fundamentals of digital particle image velocimetry. Measurement Science and Technology 8:1379-1392.

Willert CE, Gharib M. 1991. Digital particle image velocimetry. Experiments in Fluids 10:181–193.

Wolfstein M. 1969. The velocity and temperature distribution of one-dimensional flow with turbulence augmentation and pressure gradient. International Journal of Heat and Mass Transfer 12:301-318.

VITA

Philippe Sucosky was born in Nice, France, in 1976. He completed his high-school education in France, earning the Baccalauréat in Science in 1994. From 1994 to 1996, he completed two years of preparatory classes with a major in mathematics, physics, design and manufacturing at the Lycée des Eucalyptus, Nice, France.

After passing the national exam in 1996, he started his undergraduate program at the Ecole Nationale Supérieure des Arts et Métiers (ENSAM), Aix-en-Provence, Metz and Paris, France, a leading French National School of Engineering and Manufacturing. During his senior year in 1998, he specialized in thermal and fluid sciences and conducted a research project in collaboration with the Centre National de Recherche Scientifique (CNRS), the French National Center of Scientific Research.

In July 1998, he enrolled as a Masters student at the George W. Woodruff School of Mechanical Engineering at the Georgia Institute of Technology, Atlanta, GA, USA. Between July and December 1998, he started his Masters program at Georgia Tech Lorraine, Metz, France, the European campus of the Georgia Institute of Technology, while completing his undergraduate curriculum at ENSAM.

In 1999, he conducted his final ENSAM research project on the design and optimization of an abrasive waterjet cutting system. He earned his Engineering diploma with the Silver Medal distinction in July 1999.

He started his Masters Thesis on the prediction of the kerf width produced by a waterjet cutting head on silicon wafers on the main Georgia Tech campus, Atlanta, GA in August 1999 and graduated in May 2000 with a major in fluid mechanics and tribology.

From May 2000 to May 2005, he completed his Ph.D. in Mechanical Engineering with a major in fluid mechanics and thermodynamics and a minor in biomechanics. His research interests focused on the fluid mechanics of bioreactors and the modeling of the effects of shear stresses on cartilage growth in spinner-flask bioreactors.